Multi-scale Sintering Model of Visco-Elastic Powders

JUAN E. ALVAREZ

MULTI-SCALE SINTERING MODEL OF VISCO-ELASTIC POWDERS

Juan Esteban Alvarez Naranjo

MULTI-SCALE SINTERING MODEL OF VISCO-ELASTIC POWDERS

DISSERTATION

to obtain
the degree of doctor at the University of Twente,
on the authority of the rector magnificus,
Prof.dr. ir. A. Veldkamp,
on account of the decision of the graduation committee,
to be publicly defended
on Friday 27 October 2023 at 16:45 hours

by

Juan Esteban Alvarez Naranjo
born on the 8th Nov 1991 in Zarzal - Valle del Cauca,
Colombia.

This dissertation has been approved by:

Promotor:
Prof.dr.rer.-nat. S. Luding

Co-promotor:
Dr. T. Weinhart

To my grandfather Bernabe

"If have seen further, it is by standing on the shoulders of giants."
- Isaac Newton

SUMMARY

This thesis aims to investigate the sintering process of visco-elastic particles through a multi-scale framework and multi-physics approach. The research examines the sintering process at various scales, ranging from particle-particle interactions at the microscopic scale to continuum deformations at the macroscopic scale. By combining computer simulations and laboratory tests, the investigations gain valuable insights into the micro-macro responses of the sintering process.

The thesis is organized into four distinct yet interconnected chapters that span the entire spectrum of the sintering process. These chapters focus on the following aspects:

- In Chapter 2, we characterise contact rheology. The focus is on understanding the mechanical interactions between particles during the sintering process.

- In Chapter 3, we explore the multi-physics of sintering. It delves into the physical phenomena that occur during sintering considering heat transfer and material flow.

- In Chapter 4, we analyse the influence of material and process parameters on sintering. The study investigates how different material properties and process conditions affect the overall sintering process and its outcomes.

- In Chapter 5, we couple the discrete model to the continuum model for a multi-scale framework. It bridges the gap between the micro- and macro-scales by developing a comprehensive multi-scale model that incorporates both particle-level interactions and macroscopic deformations.

The findings of this research offer an understanding of the sintering process in Additive Manufacturing by integrating microscopic and macroscopic perspectives. Furthermore, this study highlights the potential to continue developing and optimizing the sintering processes using advanced multi-scale modelling techniques via virtual prototyping.

SAMENVATTING

Deze dissertatie heeft tot doel het sinterproces van visco-elastische deeltjes te onderzoeken via een multi-fysische benadering op meerdere schaalniveaus. Het onderzoek analyseert het sinterproces op verschillende schaalniveaus, variërend van deeltjes-deeltjesinteracties op de microscopische schaal tot continuüm vervormingen op macroscopische schaal. Door computersimulaties en laboratoriumtests te combineren, levert het onderzoek waardevolle inzichten op in de micro-macro reacties van het sinterproces.

Deze dissertatie is onderverdeeld in vier afzonderlijke, maar onderling verbonden hoofdstukken die het gehele spectrum van het sinterproces bevatten. In deze hoofdstukken staan de volgende aspecten centraal:

- In Hoofdstuk 2 karakteriseren we contactreologie. De focus ligt op het begrijpen van de mechanische interacties tussen deeltjes tijdens het sinterproces.

- In hoofdstuk 3 onderzoeken we de multifysica van het sinterproces. Hierbij gaan we dieper in op de fysische verschijnselen die optreden tijdens het sinteren, waarbij rekening wordt gehouden met warmteoverdracht en materiaalstroming.

- In Hoofdstuk 4 analyseren we de invloed van materiaal- en procesparameters tijdens het sinteren. De studie onderzoekt en discussieerd hoe verschillende materiaaleigenschappen en procesomstandigheden het algehele sinterproces beïnvloeden.

- In hoofdstuk 5 koppelen we het discrete model aan het continuüm model voor een raamwerk op meerdere schaalniveaus. Het overbrugt de kloof tussen de micro- en macro schaal door een alomvattend multi-schaalmodel te ontwikkelen dat zowel interacties op deeltjesniveau als macroscopische vervormingen omvat.

De bevindingen van dit onderzoek bieden inzicht in het sinterproces in additieve productie door microscopische en macroscopische perspectieven te integreren. Bovendien benadrukt deze studie het potentieel om sinterprocessen verder te ontwikkelen en te optimaliseren met behulp van geavanceerde multi-schaal modelleringstechnieken via virtuele prototypen.

CONTENTS

1

INTRODUCTION

1.1. ENGINEERING AND THE MULTI-SCALE ANALYSIS

Throughout the history of engineering, humans have been captivated by the interplay between the mesmerizing intricacies of microscopic phenomena and the fascinating emergent effects they have on macroscopic objects. By studying and predicting the behaviour of matter at multiple scales, engineers strive to unlock the secrets of the physical world. As a mechanical engineer, I am particularly fascinated by the laws that govern the behaviour of granular materials, which can be represented as granulates (discrete objects) at the micro-scale and as a continuum at the macro-scale, as discussed throughout this document. By comprehending the behaviour of materials at both the micro and macro levels, engineers can develop new manufacturing processes and optimize the performance of existing materials and structures. It is therefore crucial to advancing the field of engineering and finding solutions to complex challenges.

To comprehend the microscopic and macroscopic behaviour of matter, granulates and continuum, we rely on the laws of physics. On the micro-scale, the movement of each granulate can be governed by Newtonian classical theory [1]. On the macro-scale, the continuum laws enable us to predict the movements of matter that satisfy the conservation of mass, momentum and energy. The accuracy of these laws is remarkable for predicting the behaviour of various materials such as metal, ceramics and polymers, even when simplifying assumptions are made to analyse mechanical problems. For instance, sand behaves like a fluid, solid, and liquid simultaneously, posing a multi-physics problem (see Fig. 1.1, left). Still, the movement of the particles can be predicted using a simple physical balance of total external force and linear momentum in the local form (Newton's second law) [2]. In other cases, like the sintering of synthetic particles using a laser source, depicted in Fig. 1.1, right, two physical balances come into play, accounting for both the equilibrium of momentum and the balance of thermal energy [3].

1

However, the accurate prediction of granular material behaviour under various conditions requires the inclusion of specific rheology and contact laws in the models. Rheology, which explores how materials flow, deform, and react to applied forces or stresses, plays a critical role in understanding their mechanical properties. Meanwhile, the contact law governs the interactions between material surfaces when they come into contact. Researchers can enhance the accuracy of predictions by customizing these laws to suit the material being analysed, referred to as contact rheology within this document, thereby gaining deeper insights into its response to external factors. This tailored approach allows for a more comprehensive understanding of granular materials and opens up possibilities for improved modelling and analysis techniques.

As an application example of granular behaviour and my passion within the field, this thesis focuses on the application in the field of 3D printing, specifically, **the sintering of visco-elastic particles**. This intricate process involves the interplay of multiple physical phenomena, including heat transfer and mechanics. There are two main methods to study this process:

First, the selective **laser sintering** (SLS). It starts by preparing a layer of particulate material on a platform. Then, a laser is used to heat and fuse specific areas, layer by layer. The platform moves down, and more particles are added for each new layer. This continues until the entire object is formed. SLS is known for its precision and adaptability.

Second, the **homogeneous sintering**. It begins with the pellet preparation. The particles are compacted into a solid shape and heated in a controlled environment. During heating, the particles in the compact merge together and remove any gaps, resulting in a denser structure. After heating, the pellet cools and solidifies, and an additional axial pressure can assist the process.

To tackle the complexity of this process, and study the sintering process, this thesis integrates micro-scale and macro-scale models with contact rheology models. This synergistic approach enables the analysis of multi-physics and **multi-scale** problems, paving the way for advancements in additive manufacturing as a cutting-edge technology.
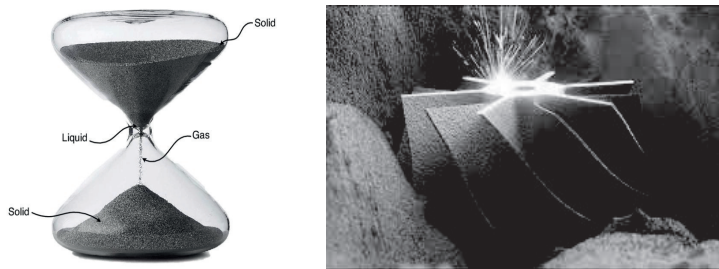
Figure 1.1: Left: an hourglass contains sand that exhibits characteristics of both solid, liquid, and gas as it moves through the orifice (Copyright [4]). Right: sintering of synthetic particles using a laser source to create a 3D object (Copyright [5]).

1.2. CONTACT RHEOLOGY OF VISCO-ELASTIC MATERIALS

Rheology is a multidisciplinary scientific field that studies the flow and deformation of materials when exposed to external stresses or strains. The field encompasses a diverse range of materials, including those that exhibit elastic, plastic, or visco-elastoplastic behaviour under dissipative effects [6, 7]. Studies that investigate the thermo-visco-elastoplastic properties of materials seek to explore how their rheological behaviour changes as a function of temperature and other variables.

At the microscopic and particle scale, materials are influenced by various factors, such as particle size, shape, packing density, and inter-particle forces, and can exhibit a diverse range of rheological behaviours. For instance, particulate materials or powders can behave as solids, retaining their shape and resisting deformation, or as liquids, flowing and spreading like fluids [8, 9]. Most granular materials display complex phenomena, such as jamming or intermittent flow phenomena, where the material can suddenly become rigid or fluid-like based on changes in stress or other factors [10, 11]. Understanding these rheological contact properties is crucial for practical applications, such as the sintering process, where visco-elastoplastic particles are bonded by applying temperature to their surfaces [12, 13]. The behaviour of powders during sintering is determined by properties, such as their viscosity and contact stiffness, which can influence their densification and final mechanical properties.

At the macroscopic and continuum level, the rheology of a material can be described by constitutive equations such as Hooke's law [14]. Note that Hooke's law is a linear relation and rheology can be more complex. These equations establish a linear relationship between stress and strain and enable scientists and engineers to calculate the mechanical properties of both isotropic and anisotropic visco-elastoplastic materials, such as their stiffness, elasticity, and strength. In addition to mechanical properties, these constitutive equations can be modified to incorporate thermal effects, enabling scientists to predict how a material will deform and respond to changes in temperature, external fields and boundary conditions.

Therefore, understanding the rheological contact properties and modelling the behaviour of visco-elastic materials through different scales may help to optimize their design and usability.

1.3. MODELLING MATERIAL BEHAVIOUR

Modelling the behaviour of materials at both micro- and macro-scales requires the use of computational models that describe the mechanical interaction by using constitutive rheological relationships and ensuring physical balance. At the micro-scale, the interaction of particles or discrete elements can be computed using the discrete element method (DEM) through contact laws [15]. On the other hand, at the macro-scale, the behaviour of materials is modelled using a discretization process such as the finite element method (FEM) to determine a material's mechanical properties, such as strength and elasticity of a material [16]. These computational models provide insights into the complex rheological properties of materials and can be used to

1

develop new materials with specific properties for various applications. Furthermore, to couple the two scales, a volume coupling approach can be developed, which provides a comprehensive understanding of the material behaviour at both micro- and macro-scales.

1.3.1. DEM TO MODEL THE MICRO-SCALE

By modelling each particle and simulating their interactions, DEM can provide insights into the behaviour of granular materials at a microscopic level. This method allows for the constitutive relation of deformation to be introduced at the contact level, where the behaviour of particles in contact can be characterized by visco-elastic or plastic models [17, 18]. One widely used software for particle contact interaction is MercuryDPM [19], an open-source package that has been extensively utilized in the field of granular materials research and used in the present investigation. The package allows for the simulation of complex scenarios, such as particle-particle interactions with multiple contact points and particle-wall interactions with frictional or adhesive properties.

1.3.2. FEM TO MODEL THE MACRO-SCALE

FEM is a widely used computational technique for modelling the behaviour of complex systems. It involves dividing a continuous system into smaller finite elements and solving for the behaviour of each element individually. The process involves discretizing a continuum model represented by partial differential equations (PDEs). These individual solutions are then combined to create a solution for the entire system. This approach can be used to study a variety of phenomena, including fluid dynamics, heat transfer, and structural mechanics [20, 21]. oomph-lib is an open-source software package that is widely used for implementing finite element models [22]. The present investigation also utilizes oomph-lib to model and simulate the behaviour of materials at the macroscopic level.

1.3.3. MULTI-SCALE COUPLING

Volume coupling techniques are essential in multi-scale modelling as they enable the application of micro- and macro-models in the same simulation, in different regions. These methods introduce a coupling region where information between both scales is exchanged. The size and shape of the coupling region are determined based on the length scale at which the micro and macro scales interact. These methods have been developed to effectively ensure the conservation of momentum and energy in the coupling region [23, 24]. The method is also preferred over other coupling methods such as surface coupling in simulations of laser sintering because it captures the internal interactions and complex physical phenomena that characterize the sintering process. For example. laser sintering primarily affects a material's interior, involving heat transfer, mass transport, phase changes, and mechanical deformation throughout the entire volume. Therefore, volume coupling methods enable a more precise representation of these interactions, including the gradual filling of pores, conserving mass, and simulating thermal and mechanical behaviour within the material. In this

investigation, a volume coupling approach is applied to a thermo-mechanical system, which allows for the simulation of larger length and time scales while retaining the essential features of the micro-scale behaviour.

1.3.4. MACHINE LEARNING FOR CALIBRATION

To ensure that simulations accurately reflect the physical behaviour of matter, they must be validated against experimental data. However, the quantification of material properties, especially at the micro-scale, is extremely challenging to evaluate, and therefore, parameters are calibrated according to the time evolution and best confidence. In the present investigation, we treat the quantification of parameters as an inverse problem, that is to infer particle-scale parameters from experimental observations. To this end, the iterative Bayesian filtering framework proposed by Cheng *et al.* [25], an open and machine learning-based package, is coupled with MercuryDPM to define the best probabilistic set-up for the models. It uses the recursive Bayes' rule to quantify the evolution of the probability distribution of parameters over iterations, which are guided to be asymptotically close to optima.

To achieve a comprehensive investigation of the sintering process, this study focuses on the following research questions:

- How can we model the vico-elastic material deformation at the particle-particle interactions using the discrete element method (DEM)?

- What is the impact of process and material parameters on the sintering process?

- How can the finite element method (FEM) be employed to bridge the sintering process's response to a macroscopic scale?

- In what ways can virtual prototyping be facilitated through the integration of DEM and FEM?

1.4. THESIS OUTLINE

The primary goal of this thesis is to provide an investigation of the sintering process of particles using a multi-scale framework and multi-physics approach. This framework allows for a detailed characterization of the contact rheology of visco-elastic materials and the evaluation of the impact of process and material parameters. To achieve this goal, we use a combination of computer simulations and laboratory tests as tools to gain insights into the micro-macro responses of the system. The thesis comprises four distinct yet interrelated chapters that cover the entire spectrum of the sintering process, from the particle-particle interaction at the micro-scale to the continuum deformations at the macro-scale. Fig. 1.2 shows the designed framework to understand the multi-physics and multi-scale of the sintering process.

In Chapter 2, we present a DEM model for predicting the sintering kinetics of visco-elastic particles based on a sintering regime map that accounts for the material contact rheology during particle-particle interpenetration. The model incorporates three different sintering mechanisms, each describing a distinct driving force that

1
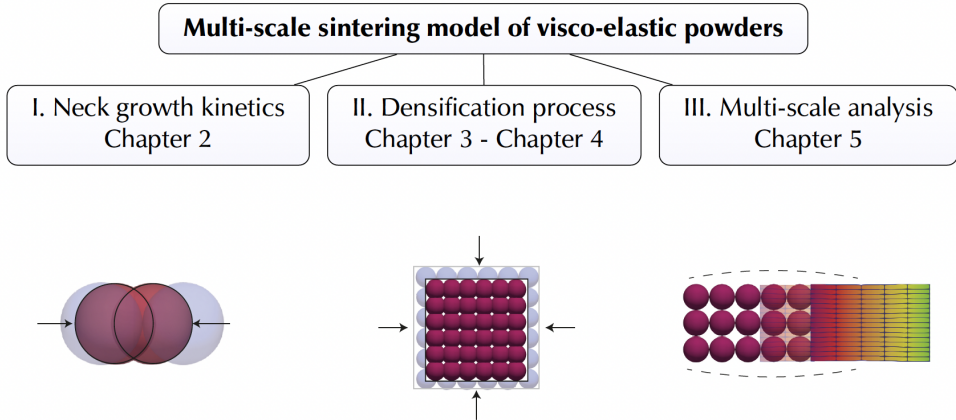
Figure 1.2: A diagram of the multi-scale investigation of the sintering process of visco-elastic powders, covering four distinct investigations. Investigation I: Characterizing the rheology of visco-elastic particles during sintering. Investigation II: Implementing energy absorption and multiphysics modelling to describe laser sintering. Analyzing the effect of pressure and temperature to characterize bulk measurements of powder systems. Investigation III: Developing the coupling between the discrete and continuum media.

allows for a precise description of the kinetics and therefore the sintering rate. The simulations are calibrated using Bayesian inference, and we analyse the sintering behaviour of Polyamide 12 in both virgin and aged states, polystyrene (PS), and polyetheretherketone (PEEK). The simulations show good agreement with experimental data and accurately describe the neck-growth kinetics, indicating that sintering takes two to three times longer for aged polymers.

Chapter 3 builds upon Chapter 2 by incorporating the thermal balance into the model to better describe the multi-physics of sintering, including the interaction between the laser and the visco-elastic particles. The sintering regime map is further refined by taking into account the temperature dependence of the DEM model. Additionally, a new ray tracing model approach is implemented to accurately evaluate energy absorption during laser-particle interaction. The calibration procedure is performed using Bayesian interference with experimental data on PA12 and PS, ensuring accuracy and reliability. Using the calibrated model, a case study of polymer thin-layer sintering is analysed, demonstrating that doubling the energy intensity results in an irradiated zone that shrinks by up to 2%. These findings highlight the importance of carefully optimizing energy parameters to achieve the desired sintering results.

Chapter 4 focuses on understanding the influence of material parameters on the sintering process by exploring the densification process. The DEM model, which is now temperature and pressure dependent, is utilized to conduct simulations of both free and pressure-assisted sintering. Experimental dilatometric data of PA12 is used to validate the model's ability to predict the effects of temperature, holding time, process time, and pressure on viscoelastic pellets. The findings of the study demonstrate that the application of pressure during sintering is particularly beneficial when the

temperature is close to the material's melting point. This insight emphasizes the importance of considering the material properties and process parameters to achieve optimal sintering outcomes.

In Chapter 5, we present a continuum model to describe the thermo-mechanical behaviour of granular materials on the macroscopic scale and introduce a volume-coupled multi-scale model of the sintering process. Firstly, the thermo-mechanical continuum analysis is validated using the strength of materials and mechanical vibration tests. Thereafter, the coupling to the granular scale is performed, which is ensured to be highly accurate using coarse-graining techniques. A multi-scale simulation of the sintering process, calibrated from the particle interaction and contact rheology, is then performed to demonstrate the advantages and usability of the coupled research. This approach provides a more comprehensive understanding of the sintering process by integrating the microscopic and macroscopic perspectives. The results of this study highlight the potential for continued development and optimization of sintering processes using multi-scale modelling techniques.

Finally, we give our conclusions and an outlook in Chapter 6.

REFERENCES

[1] R. C. Dolcetta, *Classical Newtonian gravity*, (2019), https://doi.org/10.1007/978-3-030-25846-7.

[2] E. Manger, T. Solberg, B. H. Hjertager, and D. Vareide, *Numerical simulation of the ticking hourglass*, International journal of multiphase flow **21**, 561 (1995).

[3] Y. Yang, O. Ragnvaldsen, Y. Bai, M. Yi, and B.-X. Xu, *3D non-isothermal phase-field simulation of microstructure evolution during selective laser sintering*, npj Computational Materials **5**, 81 (2019).

[4] *https://www.stickpng.com/img/objects/hourglasses/hourglass-grey-sand*, (2023).

[5] *https://www.3dnatives.com/en/direct-metal-laser-sintering100420174-2*, (2023).

[6] N. Chand and M. Fahim, *Tribology of natural fiber polymer composites* (Woodhead publishing, 2020).

[7] S. Luding, *Cohesive, frictional powders: Contact models for tension*, Granular Matter **10**, 235 (2008).

[8] P. Snabre and P. Mills, *Rheology of concentrated suspensions of viscoelastic particles*, Colloids and Surfaces A: Physicochemical and Engineering Aspects **152**, 79 (1999).

[9] A. Zubov, J. F. Wilson, M. Kroupa, M. Soos, and J. Kosek, *Numerical modeling of viscoelasticity in particle suspensions using the discrete element method*, Langmuir **35**, 12754 (2019).

[10] S. Luding, Y. Jiang, and M. Liu, *Un-jamming due to energetic instability: statics to dynamics*, Granular matter **23**, 1 (2021).

[11] W. Nan, M. Pasha, T. Bonakdar, A. Lopez, U. Zafar, S. Nadimi, and M. Ghadiri, *Jamming during particle spreading in additive manufacturing,* Powder Technology **338**, 253 (2018).

[12] P. Hejmady, L. C. Van Breemen, P. D. Anderson, and R. Cardinaels, *Laser sintering of polymer particle pairs studied by in situ visualization,* Soft Matter **15**, 1373 (2019).

[13] P. Hejmady, L. C. van Breemen, D. Hermida-Merino, P. D. Anderson, and R. Cardinaels, *Laser sintering of PA12 particles studied by in-situ optical, thermal and X-ray characterization,* Additive Manufacturing **52**, 102624 (2022).

[14] G. Arfken, *International edition university physics* (Elsevier, 2012).

[15] P. Cundall and O. Strack, *Discussion: a discrete numerical model for granular assemblies,* Géotechnique **30**, 331 (1980).

[16] J. N. Reddy, *Introduction to the finite element method* (McGraw-Hill Education, 2019).

[17] S. Luding, *Introduction to discrete element methods: basic of contact force models and how to perform the micro-macro transition to continuum theory,* European journal of environmental and civil engineering **12**, 785 (2008).

[18] Z. Peng, E. Doroodchi, and B. Moghtaderi, *Heat transfer modelling in discrete element method (DEM)-based simulations of thermal processes: Theory and model development,* Progress in Energy and Combustion Science **79**, 100847 (2020).

[19] T. Weinhart, L. Orefice, M. Post, M. P. van Schrojenstein Lantman, I. F. Denissen, D. R. Tunuguntla, J. M. Tsang, H. Cheng, M. Y. Shaheen, H. Shi, P. Rapino, E. Grannonio, N. Losacco, J. Barbosa, L. Jing, J. E. Alvarez Naranjo, S. Roy, W. K. den Otter, and A. R. Thornton, *Fast, flexible particle simulations — An introduction to MercuryDPM,* Computer Physics Communications **249**, 107129 (2020).

[20] H. Zhou and W. Peukert, *Modeling adhesion forces between deformable bodies by FEM and Hamaker summation.* Langmuir : the ACS journal of surfaces and colloids **24**, 1459 (2008).

[21] P. Wriggers, *Finite element algorithms for contact problems,* Archives of Computational Methods in Engineering **2**, 1 (1995).

[22] M. Heil and A. L. Hazel, *oomph-lib- An object-oriented multi-physics finite-element library,* in *Fluid-structure interaction: Modelling, simulation, optimisation* (Springer, 2006) pp. 19–49.

[23] H. Cheng, S. Luding, and T. Weinhart, *CG-enriched concurrent multi-scale modeling of dynamic surface interactions between discrete particles and solid continua,* Acta Mechanica Sinica **39**, 1 (2023).

[24] J. Xiao, L. Xue, D. Zhang, S. Sun, Y. Bai, and J. Shi, *Coupled DEM-FEM methods for analyzing contact stress between railway ballast and subgrade considering real particle shape characteristic,* Computers and Geotechnics **155**, 105192 (2023).

1

[25] H. Cheng, T. Shuku, K. Thoeni, P. Tempone, S. Luding, and V. Magnanimo, *An iterative Bayesian filtering framework for fast and automated calibration of DEM models,* Computer Methods in Applied Mechanics and Engineering **350**, 268 (2019).

2

VISCO-ELASTIC SINTERING KINETICS IN VIRGIN AND AGED POLYMER POWDERS

This work provides a novel discrete element method (DEM) framework for modelling the visco-elastic sintering kinetics in virgin and aged polymer powders. The coalescence of particle pairs, over long times, is described by a combined three-stage model of the sintering process, where each stage is dominated by a different driving force: adhesive contact force, adhesive inter-surface force and surface tension. The proposed framework is implemented in MercuryDPM, an open-source package for discrete particle simulations. To quantitatively calibrate the particle-scale parameters, Bayesian filtering is used. Experimental data on Polystyrene (PS), Polyamide 12 (PA12), and PEEK powders, both virgin and aged, are analysed and confirm over a wide range of times the existence of the three distinct sintering mechanisms. In good agreement with the experimental observations, the estimation of sintering time is achieved with a significant accuracy compared to Frenkel's model. This study provides an efficient and reliable approach for future studies of strength evolution in powder-bed fusion processes.

2.1. INTRODUCTION

Selective laser sintering is a modern technique to build 3D objects from visco-elastic powders. In the process, a laser beam heats selected particles resulting in solid sinter-necks at the contact points. It leads to a solidified surface layer, which is augmented with new powder deposition and their respective sintering. If the cohesion between particles is weak, texture defects arise on the sintered object such as delamination, distortion and dimensional inaccuracies [2, 3]. Furthermore, external effects from powder spattering and laser socking may induce additional forces along the cohesion. Therefore, an appropriate sintering time needs to be set to ensure sufficient cohesion among the particles. This sintering time depends on the powder properties and the specifications of the laser beam.

To predict sintering, Frenkel's model is commonly employed [4]. This model describes the rate of sintering between adjacent particles by equating the rate of work done by surface tension to the rate of energy dissipation due to viscous flow. It results in a power law, which reproduces the neck-growth kinetics at constant time. However, predictions based on Frenkel's model disagree with experimental observations in the early stage of visco-elastic sintering [5–8]. The reason is that a single power law does not account for the non-linear behaviour in visco-elastic powders. To overcome this fact, Lin *et al.* [9] introduced a time-dependent neck growth model that depends on three sintering mechanisms. First, the neck radius is determined using a global energy balance, equating the work of adhesion to the change of potential energy [10]. Second, the neck growth is driven by adhesive inter-surface forces, accommodated by visco-elastic deformations. Third, the sintering mechanism proposed by Frenkel drives the sintering forward.

Different approaches to predict contact interaction are found in the literature, either using Frenkel's model or visco-elastic adhesive contact models [11–17]. Nonetheless, the micro-mechanical calibration remains a tremendous challenge [15, 18], mainly due to the diversity of particle surfaces, shapes, disorder and anisotropy. Furthermore, rheological flow properties are difficult to obtain when visco-elastic powders are recycled from a previous sintering process, for instance.

This work introduces a novel time-dependent sintering DEM approach to estimate the visco-elastic coalescence of polymer particles at short and long times. The approach relies on the three-stage sintering scheme proposed by Lin *et al.* [9]. First, the sintering model is integrated into the visco-elastoplastic and dissipative contact model proposed by Luding [19], using the rate of plastic overlap. Then, particle pair interactions are computed utilizing MercuryDPM [20]. The calibration of the micro-mechanical parameters is performed by the Bayesian calibration tool developed by Cheng *et al.* [21]. The current approach uses experimental data from PA12 in both virgin and aged states, PS as studied by Hejmady *et al.* [22], and PEEK as presented by Beretta *et al.* [7].

2.2. SINTERING MODEL FOR POLYMER POWDERS

When a thermal field is defined on two contacting visco-elastic particles, adhesive and surface-tension forces act to sinter the two into a single particle. According to Lin *et al.* [9], the visco-elastic kinetics during the sintering process may be described within three different stages, each dominated by a different sintering mechanism: contacts formation due to elastic and adhesive forces; contact growth driven by adhesive inter-surface forces, accommodated by visco-elastic deformation; and contact growth driven by surface tension, accommodated by viscous flow. These three mechanisms are bound by the interplay between time and length scales set by intrinsic polymer properties, including compliance properties and visco-elastic interactions during the growth phase. A regime map for the three different stages is illustrated in Fig. 2.1, similar to that developed by Lin *et al.* [9].
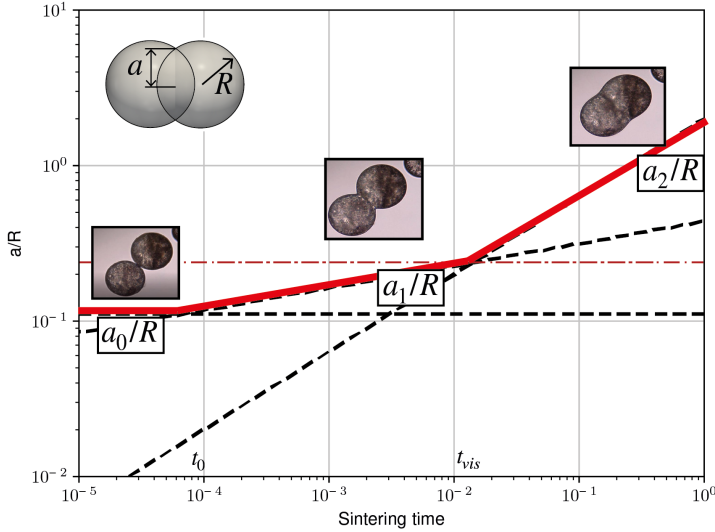
Figure 2.1: Log-log plot of the three-stage model for the growth of the dimensionless contact radius a/R with time. If $t < t_0$, a_0/R is a constant derived from JKR theory. For intermediate times $t_0 < t < t_{vis}$, a power-law behaviour emerges, $a_1/R \sim t^{1/7}$, exhibiting only weakly time-dependent growth. For $t > t_{vis}$, $a_2/R \sim t^{1/2}$, indicative of viscous sintering, which results in faster growth.

In the first stage, the sintering kinetics is described by balancing the work exerted by adhesive forces within the contact area between the particles and the work of the visco-elastic deformation. Johnson, Kendall, and Roberts (JKR [10]) expressed that under zero applied load, the contact between two particles exhibits an initial flattened contact radius a_0. Thereby, with zero applied load, the two contacting particles approach an equilibrium state in which the elastic repulsion is balanced by the adhesive attraction of the particles. JKR analysis assumes that the particles are linearly elastic, and the strain theory is used since the contact area is smaller than the radius of the particles. The schematic illustration of this first stage is presented in Fig. 2.2.
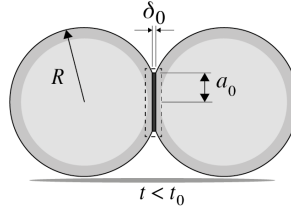
Figure 2.2: Schematic of contact area following the JKR model. An instantaneous flattened contact of radius a_0, corresponding to sphere-interpenetration δ_0, is formed to ensure an equilibrium state of two contacting particles without external forces.

The non-dimensional neck radius a_0/R was derived by JKR at very short times ($t \ll t_0$) for the equilibrium deformation of two elastic bodies under the influence of surface tension. Thus, the elastic repulsion using the Hertz equation is balanced by the adhesive traction of the particles, giving

$$\frac{a_0}{R} = \left(\frac{9\pi(1-\nu^2)\gamma}{ER} \right)^{1/3},$$ (2.1)

where γ is the surface tension ($[\text{Nm}^{-1}]$), ν is Poisson's ratio, E is Young's modulus ([Pa]). Within this adhesive stage, the contact radius is not time-dependent due to the time-invariant modulus, which is that of a glassy solid, and a very rapid swing-in period, which is neglected.

After the initial contact ($t > t_0$, see Fig. 2.1), the second stage of neck growth is due to visco-elastic deformation of the particles balanced by inter-surface adhesive forces acting in the region around the contact area, as illustrated in Fig. 2.3.

In this stage, polymers can exhibit all intermediate-range of properties between an elastic solid and a viscous liquid. For this, two main phenomena required being involved while the visco-elastic particles are bonding: creep compliance and stress relaxation. First, creep $C(t)$ ($[\text{Pa}^{-1}]$) quantifies the capacity of a material to flow in response to a sudden applied stress. Second, stress relaxation indicates the moment at which a visco-elastic material relieves stress under strain. Therefore, the strain rate is a function of time under instantaneous application of constant stress σ, expressed in a non-Hookean fashion as

$$\epsilon(t) = C(t)\sigma.$$ (2.2)

2
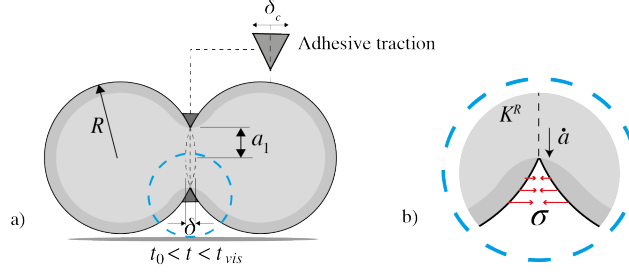
Figure 2.3: a) Schematic of visco-elastic contact growth for $t_0 < t < t_{visc}$ driven by adhesive traction. Forces act normal to the contact plane. b) Inner problem of local adhesive bonding.

The contact creep compliance is a useful metric that quantifies a unique mechanical response, defined by

$$C(t) = C_0 + C_1 t^m, \qquad (2.3)$$

where $C_0 = (1 - v^2)/E$ represents the instantaneous compliance ($[\text{Pa}^{-1}]$), C_1 ($[\text{Pa}^{-1}\text{s}^{-1}]$) is a material property, called "fluidity" in our work, and $0 < m < 1$. To treat the problem of sintering due to adhesive forces, the region around the contact area is modelled as a crack, computing the adhesive traction between the two-particle surfaces using a cohesive traction theory. Theoretically, virtual elements are attached to the particle surfaces in order to mimic the adhesive traction. These elements describe inter-surface adhesive forces in the regime of visco-elastic deformation. By assuming that the virtual element is smaller than the contact radius a, the visco-elastic contact problem can be decomposed into an outer problem of contact mechanics, and an inner problem of local adhesive bonding [9]. The contact radius a approaches to the radius R by the reference contact stress field $\sigma(r, t) \approx \frac{K^R}{\sqrt{2\pi(a-r)}}$, which indicates a singularity at the contact edge. The strength of the singularity K^R is related to the contact radius and the external loading history, which depends on the rate at which strain increases for constant applied stress (creep compliance). The Dugdale-Barenblatt cohesive zone model is used to represent the intersurface adhesive forces, assuming that adhesive force σ is constant inside the cohesive zone as long as the separation distance is less than the critical separation distance δ_c ([m]). The separation distance is specified to ensure the work of adhesion, defined as the range of the adhesive force. Then, the work of adhesion is computed as $W = \sigma\delta_c$. The prediction of the rate of bonding $\dot{a}$ is coupled with the strength of the singularity at the tip by Lin *et al.* [9], which results

$$\dot{a} = \frac{\pi\gamma}{2c_m^2 C_0 \sigma^2} \left(\frac{C_1 \gamma_m}{C_0 c_m} \right), \qquad (2.4)$$

where $c_m = (2m + 1)/(m + 1)$, and $\gamma_m = (4/\pi)^{1/2}\Gamma(m + 1)\Gamma(m + 1.5)$, with Γ as the gamma function of adhesion. By solving the evolution of the contact radius in Eq. (2.4), the estimation of a is obtained as function of the creep response of the material

$$a = a_0^{\frac{3(m+1)}{4m+3}} \left(\frac{4m+3}{m} \frac{\pi\gamma}{2c_m^2 C_0 \sigma^2} \left(\frac{C_1\gamma_m}{C_0 c_m} \right) \right)^{\frac{m}{4m+3}} t^{\frac{m}{4m+3}}, \tag{2.5}$$

where the term $a_0^{\frac{3(m+1)}{4m+3}}$ of the Eq. (2.5) indicates the formation of an initial elastic JKR contact (Eq.(2.1)), and a visco-elastic transition followed by creeping contact growth for times $t \gg (C_0/C_m)^{1/m}$. It leads to the exact long time solution for visco-elastic contact growth driven by adhesive traction with a power-law of $t^{m/(4m+3)}$, derived by Hui *et al.* [9]. Thus, the growth of the contact radius can be computed by

$$\frac{a}{R} = \left(\frac{9\pi}{2} \right)^{\frac{m+1}{4m+3}} \left[\frac{4m+3}{m} \frac{\pi}{4c_m^2} \left(\frac{\delta_c}{R} \right)^2 \right]^{\frac{m}{4m+3}} \left(\frac{\gamma_m}{c_m} \frac{2C_1\gamma}{R} \right)^{\frac{1}{4m+3}} t^{\frac{m}{4m+3}}. \tag{2.6}$$

For intermediate times in the interval $t_0 < t < t_{vis}$, the growth of contact radius a_1 is predicted to be $t^{1/7}$ for a Maxwell material, where $m = 1$. This results in

$$\frac{a_1}{R} = \left(\frac{63\pi^3}{16} \right)^{1/7} \left(\frac{\delta_c}{R} \right)^{2/7} \left(\frac{2C_1\gamma t}{R} \right)^{1/7}. \tag{2.7}$$

Subsequently, the sintering problem is treated in the third stage for long times ($t \gg t_0$). It assumes that the visco-elastic particles achieve stress relaxation due to molecular rearrangement, and the extent of recovery is directly proportional to the formerly applied stress. The neck growth kinetics is related to the action of surface tension in the viscous flow regime (see Fig. 2.1). The schematic representation is shown in Fig. 2.4.
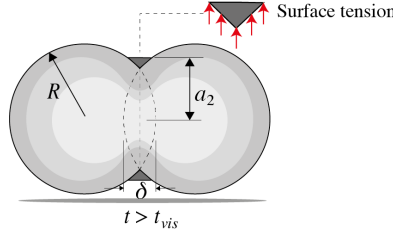
Figure 2.4: Schematic of contact growth driven by surface tension and accommodated by viscous flow. Forces act perpendicular to the contact plane.

The growth of the contact radius a_2 was initially derived by Frenkel [4], showing that for a Newtonian fluid, the evolution of a_2 may fulfil a scaling law, which is expected to be well-approximated by the last part of Eq. (2.5), where is equated the rate of surface tension work to the viscous flow energy dissipation rate, giving

$$\frac{a_2}{R} = \left(\frac{8C_1\gamma t}{R} \right)^{1/2}. \tag{2.8}$$

By defining a as the maximum of the three different models, $a = \max(a_0, a_1, a_2)$, it is possible to include each stage of the sintering process into a DEM approach. In the following chapter, we discuss how to incorporate the neck growth models (Eq. (2.1), Eq. (2.7), Eq. (2.8)) into the visco-elastoplastic contact model proposed by Luding [19].

2.3. DEM FOR VISCO-ELASTIC SINTERING

To describe the sintering of discrete particles, DEM is highly suitable. A brief description of the method is included in Appendix 2.8.1. Particles are assumed to be rigid and interact via contact forces. The computation of the forces, acting between particle pairs, are determined using contact models. In this work, we apply the visco-elastoplastic and dissipative model proposed by Luding [19], using MercuryDPM [20] to compute particle pair interactions. Fig. 2.5 illustrates the contact model.
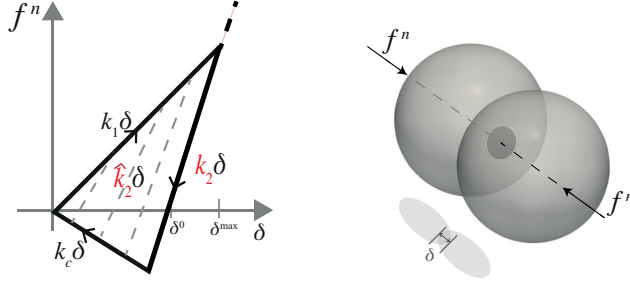
Figure 2.5: (Left) Visco-elastoplastic contact law. The contact displacement is related to δ (overlap) and the normal contact force f^n. Right/left-pointing arrows are used to distinguish the forces obtained during the loading and unloading stages, respectively. (Right) Two particle contact with overlap δ.

The elastoplastic and dissipative model computes the repulsive elastoplastic forces during compression (loading) between the particles using a loading stiffness k_1. The unloading process follows the slope of $\hat{k}_2$, which varies between k_1 and k_2, depending on the plastic deformation at zero force δ_{ij}^0. To track the plastic deformation, the maximum plastic overlap $\delta_{ij}^{\max}$ is stored, and used to compute the zero-force overlap as

$$\delta_{ij}^0 = \frac{\hat{k}_2 - k_1}{\hat{k}_2} \delta_{ij}^{\max}.$$
(2.9)

The minimum force overlap $\delta_{ij}^{\min}$ is computed as

$$\delta_{ij}^{\min} = \frac{\hat{k}_2}{\hat{k}_2 + k_c} \delta_{ij}^0.$$
(2.10)

Thereby, the overlap δ_{ij} defines the deformation measurement as

$$\delta_{ij} = (R_i + R_j) - (\mathbf{r}_i - \mathbf{r}_j) \cdot \mathbf{n},$$
(2.11)

where $\mathbf{r}_i$ and $\mathbf{r}_j$ are the particle positions with unit vector $\mathbf{n} = (\mathbf{r}_i - \mathbf{r}_j)/|\mathbf{r}_i - \mathbf{r}_j|$, and R_i and R_j are the particle radii. If the unloading stiffness $\hat{k}_2$ becomes equal to k_2, the force remains on the corresponding limit elastoplastic branch with the same slope[1]. For

---

[1]It avoids unrealistic large overlaps, also approximating the melt incompressibility with rather low stiffness, in order to have the computation time-step not too small.

overlaps smaller than $\delta_{ij}^{\max}$, the unloading stiffness is interpolated linearly between k_2 and k_1 as

$$\hat{k}_2 = \left\{ \begin{array}{ll} k_1 + (k_2 - k_1) \dfrac{\delta_{ij}^{\max}}{\phi_f R_{ij}} & \text{if } \delta_{ij} < \delta_{ij}^{\max} \\ k_2 & \text{if } \delta_{ij} \geq \delta_{ij}^{\max} \end{array} \right\}, \tag{2.12}$$

where ϕ_f is the dimensionless plasticity depth, set such that fully merged particles have a contact radius $a/R = \sqrt[3]{2}$. R represents the harmonic mean of the particle radii, $R = 2R_1 R_2/(R_1 + R_2)$. After the contact force becomes negative, for $\delta_{ij} < \delta_{ij}^0$, the model introduces cohesive forces using the cohesion stiffness k_c. Thus, the normal force f_{ij}^n between two particles in contact ($\delta_{ij} > 0$) describes the interaction as

$$f_{ij}^n = -f_{ij}^a + \left\{ \begin{array}{ll} k_1 \delta_{ij} & \text{if } \delta_{ij} > \delta_{ij}^{\max} \\ \hat{k}_2 (\delta_{ij} - \delta_{ij}^0) & \text{if } \delta_{ij}^{\min} < \delta_{ij} \leq \delta_{ij}^{\max} \\ -k_c \delta_{ij} & \text{if } 0 < \delta_{ij} \leq \delta_{ij}^{min} \end{array} \right\} - \gamma^n v_{ij}^n. \tag{2.13}$$

The adhesive force $f_{ij}^a = k_1 \delta_a$ is assumed constant, large enough to reach the equilibrium of the first sintering mechanism, see Eq. (2.1). For small displacements around some equilibrium state, this hysteretic elastoplastic model does not contain strong dissipation. Therefore, to allow for stronger dissipation and thus faster relaxation, a viscous dissipative force is included in the normal direction. The viscous dissipation coefficient is set to $\gamma^n = \sqrt{2mk_1}/(\sqrt{\pi} + \sqrt{\log e}) \log e$, such that we obtain a constant restitution coefficient e. Note, this assumes that e is measured in the elastic regime, i.e. $\delta_{ij} \ll R$. After the model parameters k_2 and γ are specified, the time-step of the simulation t_{DEM} has to be chosen such that

$$t_{\text{DEM}} \approx t_c/50, \tag{2.14}$$

where t_c represents the collision time on the contact level. For a detailed analytical model treatment, see [19].

2.3.1. RATE OF PLASTIC OVERLAP

To include the sintering behaviour proposed by Lin *et al.* [9] in the contact description (Eq. (2.13)), we compute the rate of the plastic overlap $\dot{\delta}_{ij}^0$ using a novel approach. Knowing that the overlap between the particles nearly equals the plastic overlap, $\delta_{ij} \approx \delta_{ij}^0$ for stiff particles ($k_1 \gg (f_{ij}^n + f_{ij}^a)/R$), the contact radius may be approximated as $a/R \approx \sqrt{\delta_{ij}/R}$ (small overlaps $\delta_{ij}^0 \ll R$). It can be controlled by setting the growth rate $\dot{\delta}_{ij}^0$ according to Eq. (2.1), Eq. (2.7), Eq. (2.8). First, δ_{ij}^0 is derived below the JKR equilibrium a_0/R, by satisfying $f_{ij}^n = f_{ij}^a$. Second, the computation of $\dot{\delta}_{ij}^0$ is derived within the visco-elastic deformation regime a_1/R, until the neck growth reaches the intersection point at a_{vis}/R,

$$\dot{\delta}_{ij}^0 = \frac{9}{2} \frac{\pi^3 \delta_c^2 R^{1/2} C_1 \gamma}{2^{5/7} \delta_{ij}^{7/2}} \frac{f_{ij}^n}{f_{ij}^a}, \tag{2.15}$$

where δ_c is the cohesive separation distance, and C_1 is the material fluidity. The calculation of a_{vis}/R is based on the contribution of both JKR and visco-elastic contact during $t_0 < t < t_{vis}$. The explicit expressions for t_0 and t_{vis} can be obtained by plotting Eq. (2.1), Eq. (2.7), Eq. (2.8) and finding the intersection of the curves, see Fig. 2.1, then

$$t_{vis} = \frac{1}{16}\left(\frac{63\pi^3}{2}\right)^{2/5}\frac{R}{C_1 W}\left(\frac{\delta_c}{R}\right)^{4/5}. \tag{2.16}$$

Substituting Eq. (2.16) into the expression of the second neck growth (Eq. (2.7)), gives

$$a_{vis}/R = (63\pi^3)^{1/5}\left(\frac{\delta_c}{8R}\right)^{2/5}. \tag{2.17}$$

Finally, $\dot{\delta}_{ij}^0$ is derived from Eq. (2.8) to define sintering at long times, modelled as

$$\dot{\delta}_{ij}^0 = C_1\gamma\frac{f_{ij}^n}{f_{ij}^a}. \tag{2.18}$$

All parameters of the contact model might vary with temperature, but this is neglected for simplicity assuming constant values. The only adjustable parameters in the simulations are δ_c and C_1. These parameters are calibrated using experimental data as discussed in section 2.4. Since friction forces act in the tangential direction, they do not affect the normal forces calculated via this approach, and therefore they are not discussed in this paper. For a detailed explanation, see [23].

2.4. METHODOLOGY

In Sect. 2.4.1, the sintering experiments of PA12 powder is described. Then in Sect. 2.4.2, we present the coupled implementation MercuryDPM and `GrainLearning` to calibrate the contact model based on the experimental data.

2.4.1. SINTERING EXPERIMENTS ON PA12 POWDER

Sintering experiments on PA12 were conducted with PA2200 performance powder for laser sintering supplied by EOS E-Manufacturing solutions. This powder material is a semi-crystalline thermoplastic with a melting point of about 180°C. The sintering measurements were recorded by a Keyence VHX 5000 digital microscope equipped with a Linkam THMS600 heating stage. It included a glass plate located on the top of the stage with a diameter of 22 mm and thickness of 1.7 mm.

Before starting the experiment, a fine silicon oil was placed on the plate and heated at a temperature of 300°C to distribute homogeneously. The oil reduces the adhesion between the particles and the glass plate. Then, the heating stage was cooled to room temperature, and a sample of individual virgin particles was selected manually and deposited onto the oil. Subsequently, the stage is re-heated to 195°C at a rate of 150°C/min. The coalescence of the particles was recorded using a digital microscope, using 20 frames per second and magnification between 200 and 500 times. A lower magnification was used to capture multiple particle pairs in one frame. After the

complete merging of the particles, the stage was cooled back down to room temperature. The procedure was repeated twice to reproduce deteriorated states under the same conditions of sintering using virgin particles. The microscopy images of the sintering process in virgin and two-recycled states are depicted in Fig. 2.6.
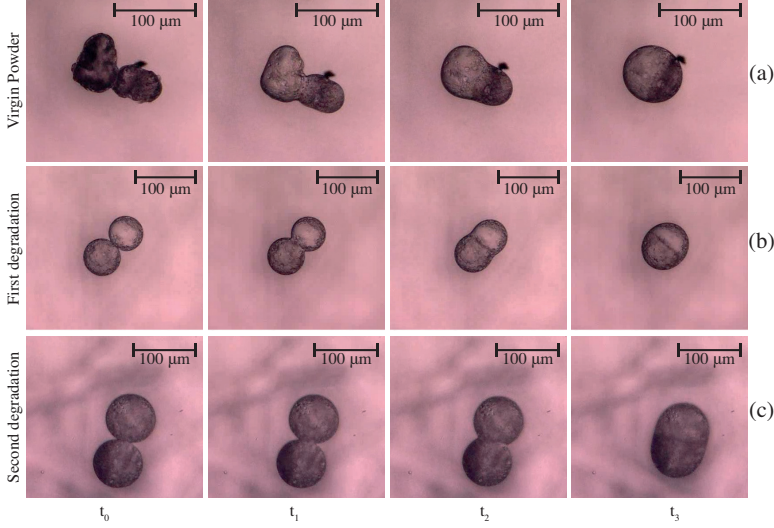
Figure 2.6: a) Sintering of virgin particles at $t_0 = 0.0\,\mathrm{s}$, $t_1 = 2.0\,\mathrm{s}$, $t_2 = 3.5\,\mathrm{s}$, $t_3 = 8.5\,\mathrm{s}$. b) Sintering of particles in a first heating at $t_0 = 0.0\,\mathrm{s}$, $t_1 = 2.0\,\mathrm{s}$, $t_2 = 6.0\,\mathrm{s}$, $t_3 = 14.0\,\mathrm{s}$. c) Sintering of particles in a second heating at $t_0 = 0.0\,\mathrm{s}$, $t_1 = 2.0\,\mathrm{s}$, $t_2 = 6.0\,\mathrm{s}$, $t_3 = 18.0\,\mathrm{s}$.

The average particle radius is determined by fitting a circle adjacent to the contact point to the measured pixel area constituting each particle and measuring its radius at beginning time t_0. Virgin particles are not always spherical, so the measured radius is only approximated, whereas particles of first or second ageing cycles are resintered and thus nearly spherical. The software ImageJ, an open-source image processing program [24], was utilized to measure the pixel length. Furthermore, the software gives information about particle area, aspect ratio, circularity, Feret diameter, perimeter and roundness. It enables the approximation of the particle radius to be set into DEM simulations.

2.4.2. DEM CALIBRATION USING GrainLearning

Microscopic material parameters relevant to sintering are extremely challenging to evaluate experimentally. Therefore, we treat the quantification of separation distance δ_c and fluidity C_1 as an inverse problem, that is to infer particle-scale parameters from experimental observations of the sintering kinetics. To this end, the iterative Bayesian filtering framework proposed by Cheng *et al.* [21] is coupled with MercuryDPM to calibrate the required sintering parameters. Fig. 2.7 presents the flowchart of this coupled implementation.

GrainLearning is a machine learning-based Bayesian calibration tool for estimating

2
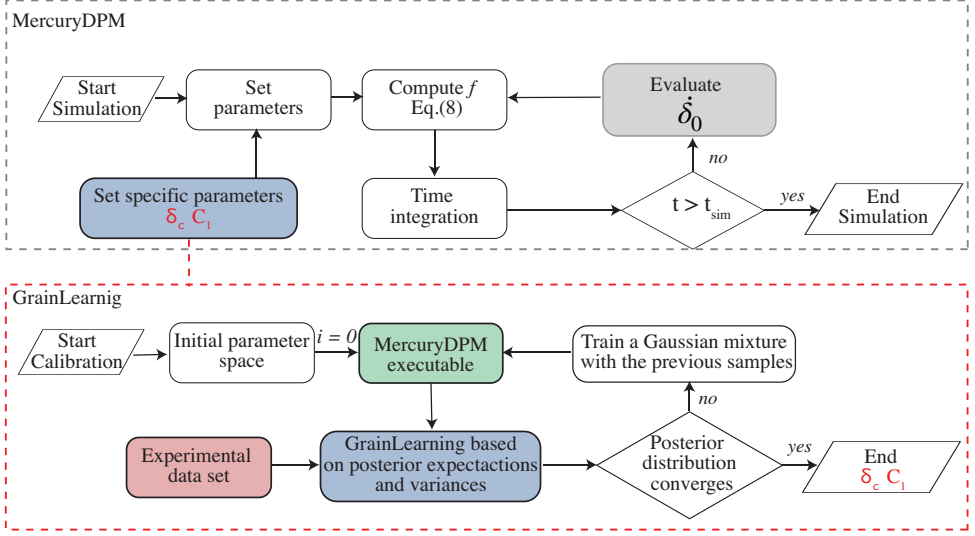
Figure 2.7: Flowchart of the coupled implementation to find the parameters: δ_c, C_1, using MercuryDPM and `GrainLearning`. A MercuryDPM executable is called by `GrainLearning` at each iteration where the probabilities over δ_c and C_1 are updated with the neck growth data. The calibration is finished if the statistics converge in three consecutive iterations.

parameter uncertainties in discrete particle simulations. It uses the recursive Bayes' rule to quantify the evolution of the probability distribution of parameters over iterations. Samples are drawn either uniformly, assuming no prior knowledge, developing an improving proposal distribution that is learned over several iterations. After having enough statistics per iteration (effective sample size), we train and utilize nonparametric Gaussian mixture models as proposal distributions to resample the parameter space. The mixture model trained at the end of each iteration guides the resampling to be asymptotically close to optima, and thus greatly reduces the computational cost compared with conventional approaches.

For Bayesian calibration, the probability distribution of model states and parameters, conditioned on given reference data (termed "posterior distribution") can be approximated by sequential Monte Carlo methods. To efficiently sample parameter space, a multi-level (re)sampling algorithm is utilized. For the first iteration of Bayesian filtering, the parameter values are uniformly sampled from quasi-random numbers, which leads to conventional sequential quasi-Monte Carlo filtering. For the subsequent iterations, new parameter values are drawn from the posterior distribution from the previous iteration. Iterative Bayesian filtering allows us to sample near potential posterior modes in parameter space, with an increasing sample density over the iterations, until the ensemble predictions (e.g., expectations) of the model parameters converge.

2.5. RESULTS AND DISCUSSION

In the following section, the proposed approach is applied to analyse the visco-elastic sintering kinetics of polymer powders. Thus, the results using virgin and aged particles are described and compared to experimental data. Finally, the influence of particle shape and sintering stress during the neck growth are discussed.

2.5.1. EFFECT OF VISCOELASTICITY ON POLYMER SINTERING

To simulate the visco-elastic sintering kinetics of polymer powders, a pair of 3D spheres of equal diameter is placed next to each other with negligible non-zero overlap between them. The particles are set just in contact at time t_0; the gravitational force is neglected. Fig. 2.8 illustrates the interpenetration between the two particles at four different time steps.
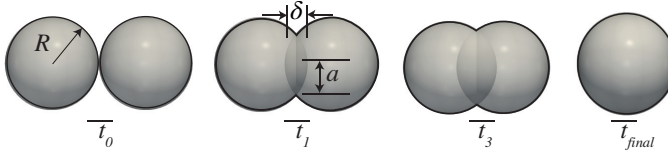
Figure 2.8: Simulation of two spherical particles using MercuryDPM. The snapshots are taken from four different time steps where $a/R = 0.0$, $a/R = 0.2$, $a/R = 0.5$, $a/R = \sqrt[3]{2}$.

A small adhesive force $f^a = k_1 \delta_a$ is applied to the particles to start the motion, where $\delta_a = 1.0 \times 10^{-3}$ m. Thereafter, the computation of the normal interaction updates the overlap δ. The geometrical relationship $a/R \approx \sqrt{\delta/R}$ can be obtained from the interaction, tracked at every time step in order to distinguish the sintering regime. All simulations use the material parameters listed in Table 2.1.

Table 2.1: System properties

ρ [kg/m^3]	k_1 [N/m]	k_2 [N/m]	k_c [N/m]	e	ϕ
1000	βER	$2.0\,k_1$	$1.0\,k_1$	0.1	$\sqrt[3]{4}$

The magnitude of stiffness k_1 cannot be compared directly with the Young's modulus E of a material, since it is a contact property. However, an approximation micro to macro parameter exist to relate $k_1 \sim \beta ER$ [25], where $\beta = 1.0$ is chosen in our work. It leads to a contact duration (half-period) $t_c \sim 2.9 \times 10^{-7}\ \mu s$, which is much smaller than the sintering time scale. Thus, the parameters in Table 2.1 only have a negligible effect on the sintering behaviour, which is determined by the evolution of δ_{ij}^0; they only affect how quickly oscillations due to the particle's inertia are damped. Young's modulus E, surface tension γ, Poisson's ratio η, and instantaneous compliance C_0 are set according to the type of materials analyzed in the present work. The magnitudes are listed in Table 2.2.

Two parameters remain to be calibrated in the contact model: δ_c and C_1. The parameters are calibrated via `GrainLearning` according to the sort of polymer and aged state. For this, the posterior probability distribution is estimated for all samples and materials with

Table 2.2: Material properties

Material	E [Pa]	γ [N/m]	η	C_0 [Pa^{-1}]
PA12	1.94×10^9	40.0×10^{-3}	0.35	2.58×10^{-10}
PS	1.23×10^9	35.6×10^{-3}	0.34	4.08×10^{-10}
PEEK 450PF	3.60×10^9	35.0×10^{-3}	0.40	1.39×10^{-10}

2

50 model evaluations per iteration. The normalized covariance parameter at the first iteration is set to 0.7, resulting in an effective sample size larger than 20%. The goal is to have a sufficient number of effective statistical samples for estimating the proposal distribution to continue the iterations. Table 2.3 lists the upper and lower limits of δ_c and C_1, for which a Halton sequence is generated.

Table 2.3: Upper and lower limits of the parameters to generate homogeneous quasi-random numbers for the first iteration.

Property	δ_c [μm]	C_1 [Pa^{-1} s^{-1}]
Θ_{min}	0.01	1.0×10^{-3}
Θ_{max}	9.0	1.0×10^1

The agreement of the posterior expectations before and after one iteration of Bayesian filtering is adopted as the convergence criterion. The posterior expectation of each micro-parameter converges after the third iteration. The illustration of the re-sampling process is presented in Fig. 2.9, which depicts the posterior modes localized progressively after each iteration for PA12, as an example. Note that if the initial guess for the model parameters is not able to capture at least one posterior distribution, the re-sampling scheme could explore outside the parameter ranges specified in Table 2.3, at the cost of more iterations and model evaluations.

VIRGIN POWDER

The first analysis corresponds to the sintering of polymers in a virgin state. The calibration of δ_c and C_1 is performed by `GrainLearning` using experimental data on PA12, PS [22], and PEEK [7]. Table 2.4 lists the results of the Bayesian calibration.

Table 2.4: Calibrated micro-mechanical properties (virgin particles)

Material	R [μm]	δ_c [μm]	C_1 [Pa^{-1} s^{-1}]
PA12	32.1	$0.28 \pm 3.0\%$	$2.42 \pm 1.0\%$
PS	30.0	$0.15 \pm 1.0\%$	$65.20 \pm 1.0\%$
PS	60.0	$0.41 \pm 1.0\%$	$27.20 \pm 1.0\%$
PEEK 450PF	25.0	$0.45 \pm 2.0\%$	$0.30 \pm 1.0\%$
PEK HP3	25.0	$0.31 \pm 2.0\%$	$0.35 \pm 1.0\%$

High precision is obtained, with only 1.0 ~ 3.0% range of error. Furthermore, the correlation of $\delta_c(R)$ is obtained as $\delta_c/R \sim 0.01$, as suggested by Lin *et al.* [9]. The visco-elastic sintering kinetic of PA12 particles is presented in Fig. 2.10.
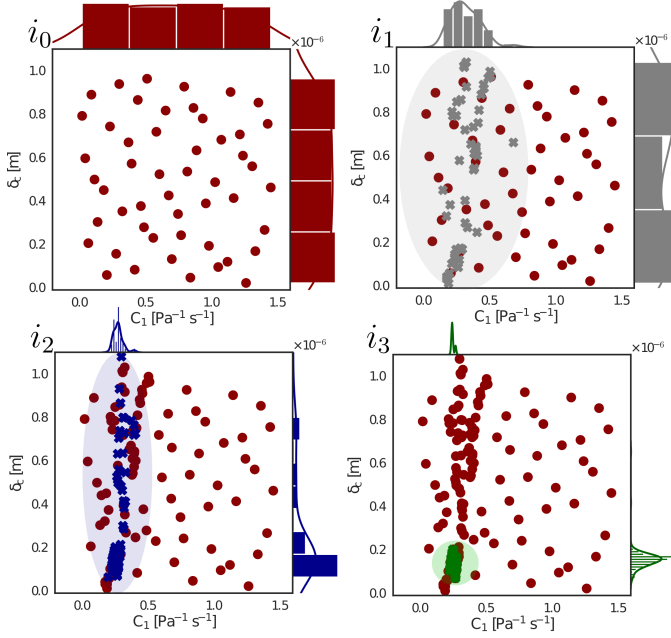
Figure 2.9: Calibration of δ_c and C_1 for sintering simulations of PA12 with $R = 33.63\ \mu$m. Bars denote the sampling distribution of the current iteration (which is based on the posterior distribution of the previous iteration, except for the first iteration). Coloured dots indicate the distributions, that are progressively placed near the posterior modes over the iterations as the localized bars show.

The experimental results show the non-linear sintering path first, corresponding to the visco-elastic behaviour of the material. The transition between the second and third sintering mechanisms is at $t_{vis} = 0.5$ s, when $a/R \sim 0.22$. The maximum overlap ($a/R = 1.0$) is crossed at $t = 3.7$ s. This overlap means that particles have still a distinctive radius. After this point, particles merge to complete the sintering at $a/R = \sqrt[3]{2}$. It is reached at $t_{final} = 5.6$ s. To compare the precision of the simulation result, the original and modified Frenkel models are calibrated using the best approximation at the maximum overlap, using $\eta = 3355.0$ Pa s. However, Frenkel models anticipate neck growth during the early stage of the process. It leads to the over-prediction of the sintering time for short sintering since the driving force for coalescence is equivalent during the process.

The neck-growth estimation for PS is plotted in comparison with the experimental data in Fig. 2.11.

An important consequence in the sintering of polymer powders is that the process is faster for materials with low molecular weight [12]. This is the case for PS, in which the stress relaxation occurs within $t_{vis} = 0.01$ s. Thereafter, the visco-elastic mechanism dominates the process to complete the full consolidation at $t_{final} = 0.11$ s for $R = 30.0\ \mu$m and $t_{final} = 0.27$ s for $R = 60.0\ \mu$m. Thereby, the influence of particle radius is highly relevant in the process, as evidenced by the retardation for sintering. The

2
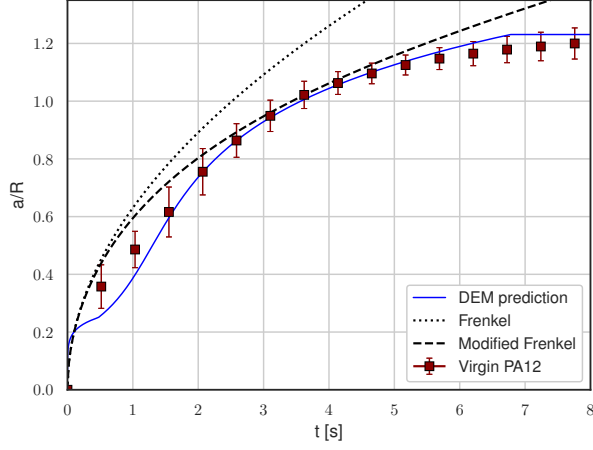
Figure 2.10: Neck growth kinetics of virgin PA12. The solid line represents the calibrated DEM simulation with $R = 32.1\,\mu$m. The dotted and dashed lines are obtained by fitting the original and modified Frenkel's models [26] to the experimental data with $\eta = 3355.0\,$Pa s, respectively. Experimental observations are represented by the error bars.
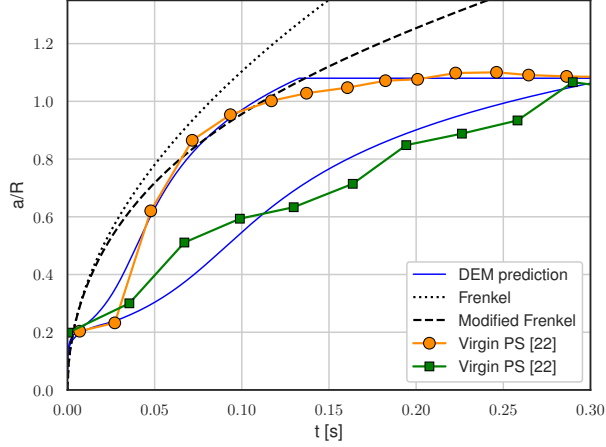
Figure 2.11: Neck growth kinetics of virgin PS. The solid line represents the calibrated DEM simulation. The dotted and dashed lines are obtained by fitting the original and modified Frenkel's models [26] to the experimental data with $\eta = 93.0\,$Pa s, respectively. Experimental observations are represented by dots for $R = 30.0\,\mu$m, and squares for $R = 60.0\,\mu$m, from [22].

maximum penetration depth was set to match the experimental merging radius at $a/R = 1.1$. This limitation was due to particles were not able to fully relax as spherical droplets experimentally [22]. It is demonstrated that PS powder can be well-described

by the proposed three-stage sintering model. Furthermore, Frenkel's equations are calibrated based on the best approximation at the merged particle radius, using $\eta = 93.0\,\text{Pa}\,\text{s}$. As the viscosity is increased, Frenkel's model may decrease the neck growth rate. However, this would retard the coalescence by leading to an inaccurate approximation.

The third analysis is conducted on PEEK 450PF and PEEK HP3, as reported by Berretta *et al.* [7]. Fig. 2.12 depicts the results.
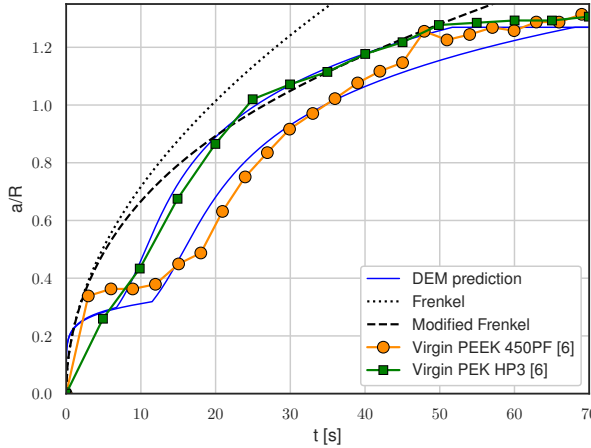
Figure 2.12: Neck growth kinetics of virgin PEEK 450PF and PEK HP3. The solid line represents the calibrated DEM simulation with $R = 25.0\,\mu\text{m}$. The dotted and dashed lines are obtained by fitting the original and modified Frenkel's models [26] to the experimental data with $\eta = 23000.0\,\text{Pa}\,\text{s}$. Experimental observations are represented by dots for PEEK 450PF and squares for PEK HP3, from [7].

The sintering of PEEK 450PF and PEK HP3 illustrates the implication of polymers with high viscosity. The relaxation for flowability is reached at $t_{vis} = 12.0\,\text{s}$, at about 36% of the interpenetration on PEEK 450PF, and $t_{vis} = 9.0\,\text{s}$, at about 34% of the interpenetration on PEK HP3. The highest slope was achieved by PEK HP3, followed by PEEK 450PF over the same time interval. It indicates that the second polymer is higher in molecular weight leading to less shrinkage. From the experimental results, it is observed the non-linear and visco-elastic kinetics of the material. This is remarkably predicted using the proposed contact model through the action of forces that involve two principal rheological characteristics, namely fluidity and elastic behaviours. These attributes determine the transport mechanism under the action of diffusive forces and stress, imposed either by thermal conditions or by mechanical action or by the combination of the two. It is relevant to mention that the particle radius used for the computations was set as the one measured at the beginning of the experiments, as reported by Berretta *et al* [7]. It may influence the prediction in the initial stage since the particles were in amorphous shapes. Frenkel's equations are calibrated based on the best approximation at the merged particle radius, using $\eta = 23000.0\,\text{Pa}\,\text{s}$. It also

indicates that the flowability is not good at high temperatures for this type of polymers.

Aged powder

To characterize polymer sintering under different aged conditions, we performed experiments based on a recycled scheme. The experimental data were collected in two different scenarios. First, the sintering process is repeated twice immediately after forming the consolidation from the virgin state; it was directly developed at the hot stage as presented in Fig. 2.6. Second, virgin PA12 powder was annealed inside an oven for 7 and 14 hours at a temperature of 160°C (below the melting point of 180°C). Then, the hot stage microscopy technique was employed to measure neck growth. Subsequently, `GrainLearning` is utilized to estimate δ_c and C_1 based on the observations. Table 2.5 lists the calibrated parameters to set within the contact model.

Table 2.5: Calibrated micro-mechanical properties

Material	δ_c [μ m]	C_1 [Pa^{-1}s^{-1}]
Virgin PA12	$0.28 \pm 3.0\%$	$2.42 \pm 1.0\%$
1st Aged PA12	$0.29 \pm 2.0\%$	$1.01 \pm 0.1\%$
2nd Aged PA12	$0.31 \pm 2.0\%$	$0.49 \pm 0.1\%$

After every usage (sintering), a trend of around 50% reduction in C_1 is observed relative to the previous situation. This is reasonable since viscosity increases in aged states, which means a lower fluidity. Conversely, the separation distance δ_c remains roughly steady, increasing by 1%. Fig. 2.13 displays the results of the sintering process for the first aged state.

In aged states, polymer sintering is slower as evidenced in Fig. 2.13. The 100% of neck growth is achieved at $t = 7.7$ s. This is twice the time required using virgin powder (see Fig. 2.10). The transition time, at which the second and third sintering mechanisms change, is at $t_{vis} = 1.1$ s; δ_c/R continues roughly steady. The two procedures to recycle PA12 led to similar experimental results. It suggests that particle properties are in a similar deteriorated state if they suffer heating conditions or if they are reused immediately after the first sintering process. Fig. 2.14 presents the neck-growth kinetics of the second aged state.

After sintering virgin powder twice, the maximum overlap $a/R = 100\%$ is obtained at about $t = 13$ s, which takes almost three times longer than the time required using virgin powder. Frenkel's models start to agree well with the experimental data at longer times due to the increased viscosity of the material in this state. The transition time between the second and third sintering mechanisms is at $t_{vis} = 1.9$ s, which is almost three times longer than the relaxation time sintering virgin particles.

Finally, Fig. 2.15 presents the three case studies for visco-elastic sintering using PA12. The degradation level has a great influence on the growth rate as evidenced in Fig. 2.15. This suggests that a lack of the supplied energy while sintering recycled powder can lead to slower neck formation, and therefore, poor cohesion. The DEM prediction indicates that the balance between the relaxation time and the material compliance has a significant contribution to the sintering of visco-elastic polymers. In fact, compliance
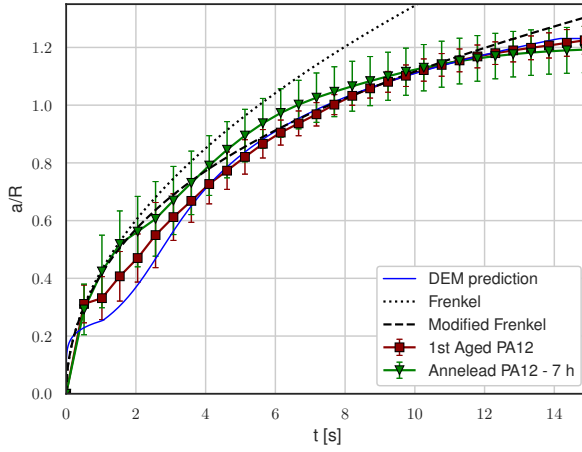
Figure 2.13: Neck growth kinetics of aged PA12 with $R = 33.7\,\mu\text{m}$. Squares represent the observations immediately after the first sintering. Triangles correspond to PA12 particles annealed inside an oven for 7 hours. The dotted and dashed lines are obtained by fitting original and modified Frenkel's models [26] to the experimental data with $\eta = 7550.0\,\text{Pa s}$.
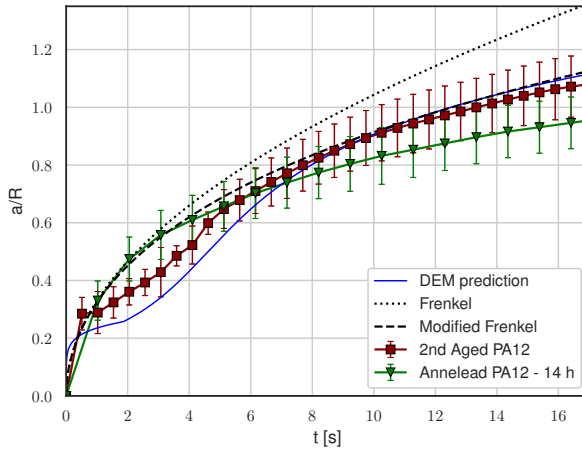
Figure 2.14: Neck growth kinetics of second aged PA12 with $R = 33.63\,\mu\text{m}$. Squares represent the observations immediately after the previous sintering. Triangles correspond to PA12 particles annealed in an oven for 14 hours. The dotted and dashed lines are obtained by fitting original and modified Frenkel's models [26] to the experimental data, with $\eta = 12500.0\,\text{Pa s}$.

is well known to be a sensitive function of molecular weight, and the visco-elastic kinetics must be analysed when modelling the sintering of polymers [12].
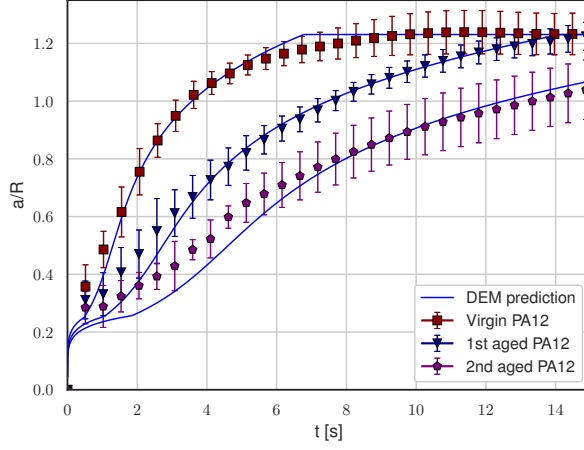
Figure 2.15: Neck growth kinetics of PA12 in virgin and aged states. Experimental observations are represented by squares, triangles and pentagons for virgin, first aged and second aged, respectively. Solid lines describe the DEM prediction.

2.5.2. INFLUENCE OF PARTICLE SHAPE DURING SINTERING

Particles are modelled as perfect spheres in the sintering simulations. It leads to a homogeneous interaction at the particle-particle contact. However, polymers are not always available as spheres in a virgin state, see Fig. 2.6. To overcome this fact, the Feret diameter was measured on the experimental data, which is an option available in ImageJ software. This diameter was set to perform the simulations in MercuryDPM. The results showed good agreement independent of the low circularity at short times, which increases when polymer particles were subjected to temperatures close to the melting point. Furthermore, particles characteristics such as morphology, surface texture and porosity are not as significant for the sintering rate at long times, and the shape evolution of the particle radius is independent of the flow history as suggested by Benedetii *et al* [11].

2.5.3. SINTERING STRESS

When particles are sintering, outward-directed traction arises at the neck tip as a result of the balance of the compressive force acting on the contact (Fig. 2.16). The traction can be expressed by

$$\sigma_t = k_s \gamma, \tag{2.19}$$

where γ is surface tension, $k_s = 2R/a^2$ represents the relationship between curvature at the neck tip and contact radius a [27].

As the particles approach the common radius during sintering, the curvature at the neck increases significantly, which becomes very large just before reaching the merging
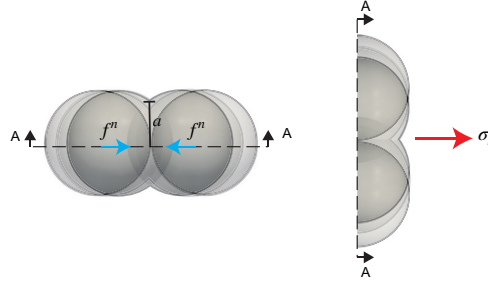
Figure 2.16: Evolution of the contact radius a during the sintering process. f^n represents the normal force and σ_t the tangential sintering stress.

radius. During this period, a debonding process may occur by external forces, leading to the formation of defects. To analyse the stress evolution during the growth of the contact radius, the tangential response during sintering of virgin and aged PA12 particles is plotted in Fig. 2.17.
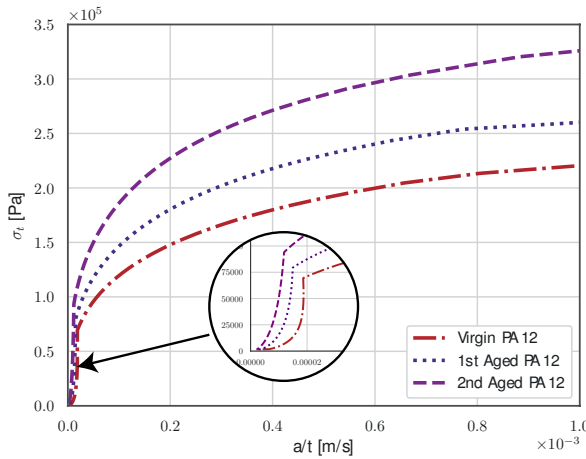
Figure 2.17: Stress evolution at the neck tip vs. the rate of contact radius for PA12 in virgin and aged states.

The sintering stress increases with time in the evolution of the contact radius. In the initial stage, a sharp peak is evidenced as the result of stress relaxation. Thereafter, this point marks the transition to mass transport due to surface tension. The contact radius grows continuously until the maximum radius, which implies the maximum stress during the process. As far as the virgin particles are aged as the higher stress reached during the consolidation. It means more energy is required to consolidate aged particles as evidenced in the neck growth kinetics (Fig. 2.15). The evolution of the tangential stress during the sintering process may be influenced by temperature gradients. As a consequence, local stresses may appear. Nonetheless, our experiments

and simulations were conducted under a controlled temperature regime, which allowed us to predict the sintering rate for all experiments.

2.6. Conclusions and outlook

Our main result is that the sintering of visco-elastic powders is accurately and quantitatively predictable, at both short and long time scales. This is successfully achieved in our DEM framework by modelling the non-linear behaviour and including three different sintering mechanisms. The presented model requires only two sintering parameters to be calibrated in the simulations. This calibration was performed using `GrainLearning` package, where the probabilistic distributions of the parameters and their correlations were inferred precisely. Even though the model does not account for the anisotropy of visco-elastic materials, it allows analysing cases where particles are recycled in two scenarios: reused powder from a previous sintering process and powder annealed inside an oven for several hours. All predictions show a remarkable agreement with the experimental observations on PA12, PS, and PEEK particles. It demonstrates the impact of this approach on the prediction of sintering times.

The proposed approach will be utilized in future DEM studies to analyse the strength evolution by particle cohesion, including different powder usage histories and temperature gradients. Thus, a better understanding of the grade of virgin and re-used particles can be assessed to avoid surface defects from the poor cohesion of sintered layers. In general, re-used powder requires a slower processing speed.

The present calculations refer to mono-disperse particles with spherical shapes. Future calculations will consider other possible particle distributions, and a multi-particle scheme to describe amorphous conditions. Furthermore, future studies on the sintering of aggregates will include the time-dependence of the radius based on the conservation of mass.

2.7. Acknowledgments

2.8. Appendices

2.8.1. Appendix: The Dicrete Element Method

The discrete element method (DEM) is a computational technique to describe the motion of particles, and for which MercuryDPM [20] is utilized. It assumes:

- Particles are unbreakable.

- Particle are undeformable, such that the particle masses m_i and inertia $\mathbf{I}_i$ are constant in the body-based frame.

- All interactions between the particles are binary, i.e. all internal forces/torques are due to particle pair interactions.

- Each particle pair i, j has at most a single contact point $\mathbf{c}_{ij}$ at which the interaction forces $\mathbf{f}_{ij}$ and torques τ_{ij} act.

- All external forces/torques acting on a particle i are either body forces $\mathbf{f}_i^b$ or interaction forces $\mathbf{f}_{ij}^w$ with a wall k. The same is true for torques.

The force and torque acting on each particle i can then be computed as

$$\mathbf{f}_i \sum_{j=1}^{N} \mathbf{f}_{ij} + \sum_{k=1}^{N_w} \mathbf{f}_{ik}^w + \mathbf{f}_i^b, \tag{2.20}$$

$$\tau_i \sum_{j=1}^{N} \mathbf{r}_{ij} \times \mathbf{f}_{ij} + \tau_{ij} + \sum_{k=1}^{N_w} \mathbf{r}_{ik} \times \mathbf{f}_{ik}^w + \tau_{ik}^w + \tau_i^b, \tag{2.21}$$

with the branch vector $\mathbf{r}_{ij} = \mathbf{c}_{ij} - \mathbf{r}_i$ connecting the particle position $\mathbf{r}_i$ with the contact point $\mathbf{c}_{ij}$. For given initial conditions, Newton's second law can then be used to evolve the particle's velocities $\mathbf{v}_i$, positions $\mathbf{r}_i$, angular velocities ω_i and orientations $\mathbf{q}_i$:

$$\frac{d\mathbf{v}_i}{dt} = \frac{1}{m_i}\mathbf{f}_i, \tag{2.22}$$

$$\frac{d\mathbf{r}_i}{dt} = \mathbf{v}_i, \tag{2.23}$$

$$\frac{d\omega_i}{dt} = \mathbf{I}_i^{-1}\tau_i, \tag{2.24}$$

$$\frac{d\mathbf{q}_i}{dt} = \mathbf{C}(\mathbf{q}_i)\omega_i, \tag{2.25}$$

For computational stability, the orientation is stored as a quaternion $\mathbf{q}_i \in \mathbb{R}$, which requires the use of a transformation matrix $\mathbf{C}(\mathbf{q}_i)$; see [20] for details.

Contact models are use to determine the forces acting between particle pairs, which can roughly be classified into three categories: elastic, plastic, and dissipative forces f_{ij}^n that act in the normal direction to the contact area, $\mathbf{n}_{ij}$; tangential forces $\mathbf{f}_{ij}^t$ and torques τ_{ij} due to sliding, rolling and torsion friction; and adhesive normal forces f_{ij}^a that may act between nearby particles even if they are not in contact. Which contact model best describes the real contact behaviour depends on the material type and particle size, and on ambient effects such as temperature and moisture. In most cases, a combination of these forces needs to be taken into account, i.e. the toral contact force is given as

$$\mathbf{f}_{ij} = (f_{ij}^n + f_{ij}^a)\mathbf{n}_{ij} + \mathbf{f}_{ij}^t. \tag{2.26}$$

REFERENCES

[1] J. Alvarez, H. Snijder, T. Vaneker, H. Cheng, A. Thornton, S. Luding, and T. Weinhart, *Visco-elastic sintering kinetics in virgin and aged polymer powders,* Powder technology **397**, 117000 (2022).

[2] G. Guan, M. Hirsch, Z. H. Lu, D. T. Childs, S. J. Matcher, R. Goodridge, K. M. Groom, and A. T. Clare, *Evaluation of selective laser sintering processes by optical coherence tomography,* Materials and Design **88**, 837 (2015).

[3] M. Markl and C. Körner, *Powder layer deposition algorithm for additive manufacturing simulations,* Powder Technology **330**, 125 (2018).

[4] J. Frenkel, *Viscous flow of crystalline bodies under the action of surface tension,* Journal of Phyiscs **9**, 385 (1945).

[5] S. Haeri, L. Benedetti, and O. Ghita, *Effects of particle elongation on the binary coalescence dynamics of powder grains for laser sintering applications,* Powder Technology **363**, 245 (2020).

[6] R. Fuchs, T. Weinhart, M. Ye, S. Luding, H. J. Butt, and M. Kappl, *Initial stage sintering of polymer particles - experiments and modelling of size-, temperature- and time-dependent contacts,* in *EPJ Web of Conferences,* Vol. 140 (EDP Sciences, 2017) pp. 1–4.

[7] S. Berretta, Y. Wang, R. Davies, and O. R. Ghita, *Polymer viscosity, particle coalescence and mechanical performance in high-temperature laser sintering,* Journal of Materials Science **51**, 4778 (2016).

[8] M. Zhao, D. Drummer, K. Wudy, and M. Drexler, *Sintering study of polyamide 12 particles for selective laser melting,* International Journal of Recent Contributions from Engineering, Science & IT (iJES) **3**, 28 (2015).

[9] Y. Y. Lin, C. Y. Hui, and A. Jagota, *The role of viscoelastic adhesive contact in the sintering of polymeric particles,* Journal of Colloid and Interface Science **237**, 267 (2001).

[10] K. Johnson, K. Kendall, and A. Roberts, *Surface energy and the contact of elastic solids,* Proceedings of the Royal Society of London. A. Mathematical and Physical Sciences **324**, 301 (1971).

[11] L. Benedetti, B. Brulé, N. Decraemer, K. E. Evans, and O. Ghita, *Evaluation of particle coalescence and its implications in laser sintering,* Powder Technology **342**, 917 (2019).

[12] S. Mazur and D. J. Plazek, *Viscoelastic effects in the coalescence of polymer particles,* Progress in Organic Coatings **24**, 225 (1994).

[13] C. T. Bellehumeur, M. Kontopoulou, and J. Vlachopoulos, *The role of viscoelasticity in polymer sintering,* Rheologica Acta **37**, 270 (1998).

[14] S. Nosewicz, J. Rojek, K. Pietrzak, and M. Chmielewski, *Viscoelastic discrete element model of powder sintering,* Powder Technology **246**, 157 (2013).

[15] M. Van den Eynde, L. Verbelen, and P. Van Puyvelde, *Assessing polymer powder flow for the application of laser sintering,* Powder Technology **286**, 151 (2015).

[16] K. Chockalingam, V. G. Kouznetsova, O. van der Sluis, and M. G. Geers, *2D phase field modeling of sintering of silver nanoparticles,* Computer Methods in Applied Mechanics and Engineering **312**, 492 (2016).

[17] J. Laube, V. Baric, S. Salameh, L. Mädler, and L. Colombi Ciacchi, *A new contact model for the discrete element method simulation of TiO$_2$ nanoparticle films under mechanical load,* Granular Matter **20**, 28 (2018).

[18] F. Rizzi, M. Khalil, R. E. Jones, J. A. Templeton, J. T. Ostien, and B. L. Boyce, *Bayesian modeling of inconsistent plastic response due to material variability,* Computer Methods in Applied Mechanics and Engineering **353**, 183 (2019).

[19] S. Luding, K. Manetsberger, and J. Müllers, *A discrete model for long time sintering,* Journal of the Mechanics and Physics of Solids **53**, 455 (2005).

[20] T. Weinhart, L. Orefice, M. Post, M. P. van Schrojenstein Lantman, I. F. Denissen, D. R. Tunuguntla, J. M. Tsang, H. Cheng, M. Y. Shaheen, H. Shi, P. Rapino, E. Grannonio, N. Losacco, J. Barbosa, L. Jing, J. E. Alvarez Naranjo, S. Roy, W. K. den Otter, and A. R. Thornton, *Fast, flexible particle simulations — An introduction to MercuryDPM,* Computer Physics Communications **249**, 107129 (2020).

[21] H. Cheng, T. Shuku, K. Thoeni, P. Tempone, S. Luding, and V. Magnanimo, *An iterative Bayesian filtering framework for fast and automated calibration of DEM models,* Computer Methods in Applied Mechanics and Engineering **350**, 268 (2019).

[22] P. Hejmady, L. C. Van Breemen, P. D. Anderson, and R. Cardinaels, *Laser sintering of polymer particle pairs studied by in situ visualization,* Soft Matter **15**, 1373 (2019).

[23] S. Luding, *Cohesive, frictional powders: Contact models for tension,* Granular Matter **10**, 235 (2008).

[24] C. A. Schneider, W. S. Rasband, and K. W. Eliceiri, *NIH Image to ImageJ: 25 years of image analysis,* (2012).

[25] S. Nosewicz, J. Rojek, M. Chmielewski, K. Pietrzak, and D. Lumelskyj, *Application of the Hertz formulation in the discrete element model of pressure-assisted sintering,* Granular Matter **19**, 1 (2017).

[26] O. Pokluda, C. T. Bellehumeur, and J. Vlachopoulos, *Modification of Frenkel's Model for Sintering,* AIChE Journal **43**, 3253 (1997).

[27] K. Shinagawa, *Simulation of grain growth and sintering process by combined phase-field/discrete-element method,* Acta Materialia **66**, 360 (2014).

2

3

CONTACT RHEOLOGY MODEL FOR VISCO-ELASTIC POWDERS DURING LASER SINTERING

Laser sintering is a widely used process for producing complex shapes from particulate materials. However, understanding the complex interaction between the laser and particles is a challenge. This investigation provides new insights into the sintering process by simulating the laser source and the neck growth of particle pairs. First, a multi-physics discrete element method (DEM) framework is developed to incorporate temperature-dependent contact rheological and thermal properties, incorporating heat transfer and neck formation between the particles. Next, energy transport by ray tracing is added to allow for computing the amount of laser energy absorbed during sintering. The DEM model is calibrated and validated using experimental data on neck growth and temperature evolution of particle pairs made of polystyrene (PS) and Polyamide 12 (PA12). The findings show that the proposed DEM model is capable of accurately simulating the neck growth during the laser sintering paving the way for better controlling and optimizing the process. As a study case, it is shown that the calibrated model can be used to predict the shrinkage of laser-irradiated zones of thin polymer layers.

3.1. INTRODUCTION

Laser sintering (LS) is an additive manufacturing technique that offers cost-efficient production of complex geometries and a variety of material options, including metals, ceramics, and polymers. The use of LS for polymer printing is rapidly expanding, with the potential for large-scale manufacturing in the near future [1]. Although multi-physics frameworks have been used to simulate the laser sintering process in polymers, accurately predicting the interaction between the laser heat source and the particulate polymer during sintering remains a challenge. Therefore, there is a critical need to develop more advanced rheological contact models and gain new insights into the underlying mechanisms of the process.

To accurately describe the LS process of a particulate polymer and the laser interaction, the flow behaviour of the material during contact (contact rheology) is a relevant characteristic to be explored as a function of the energy absorbed from the incident beam. An increasing number of studies have investigated sintering and heat transfer of polymer powders [2–5], either using the discrete element method (DEM) [6–9] or the finite element method (FEM) [10], and by including the laser beam as a Gaussian heat source function [11–13]. Nonetheless, these descriptions of polymer sintering present a discrepancy compared to experimental data due to the transient contact rheology, thermal properties and material degradation state that polymers suffer while flowing and for which the aforementioned descriptions are unable to predict. For instance, Hejmady *et al.* [14] showed that the sintering kinetics is determined by a complex interplay between the sintering mechanisms caused by the relaxation times of polymers, such as polystyrene, and the time-dependent temperature profile which also affects the polymer flow resistance. Even further, the model implemented to describe the neck growth disagreed with the experimental observations due to the aforementioned events. Polychronopoulos *et al.* [15] proposed a model for neck growth by assuming planar extensional flow for a Newtonian fluid, which results were compared with experimental data on polymer particles. Even though the predictions

showed relatively good agreement on the densification rates, it was less accurate for the neck growth rate itself.

In this study, we numerically investigate the neck growth of polymer powders during laser sintering. To achieve this, we analyse the contact rheology of PA12 and PS particle pairs, sintered by different energy inputs reported by Hejmady *et al.* [14, 16]. The discrete element method (DEM) for heat transfer problems [17–19] is used and implemented in the open-source software package MercuryDPM [20] along with an improved definition of a sintering regime map for temperature-dependent visco-elastic deformations [21]. Additionally, a new ray-tracing approach is proposed to analyse the laser beam interaction on 3D spheres, which allows to compute the energy absorbed by the materials during particle-particle inter-penetrations accurately. The DEM model parameters are calibrated using GrainLearning [22, 23], which is an efficient data-driven calibration software package. The findings indicate that the proposed framework accurately simulates the neck growth and temperature evolution when particle pairs are sintered using a laser source. As an application case of laser sintering, it is studied the laser irradiated zone on thin polymer layers based on the calibrated model.

3.2. EXPERIMENTAL DATA

Experimental data on laser sintering of PA12 and PS particle pairs were reported by Hejmady *et al.* [14, 16]. The authors measured the neck growth rate of particle pairs under different conditions and laser set-ups. Thus, several case studies were discussed in detail such as the effect of particle size, heating chamber temperature, laser pulse duration and laser energy. In this work, we have collected the reported information on the effect of laser energy on the neck growth of particle pairs and the temperature evolution of the system during the laser interaction. Fig. 3.1 depicts a schematic illustration of the experimental procedure.
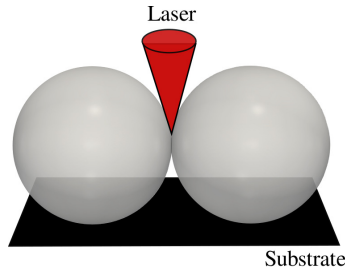
Figure 3.1: Schematic representation of the experimental procedure.

Two particles of similar size are positioned on a substrate within a heating chamber. The interface between the particles is aligned with the laser beam, as well as with the optical focus. A laser pulse is then directed locally at the contact point between the particles, and the neck sintering is captured through optical imaging. Table 3.1 summarizes the properties of the polymers and laser set-up used in the experimental configuration [14,

16].

Table 3.1: Material properties and laser configuration.

Property, symbol - units	PA12	PS
Radius, R_i - [μm]	125	60
Density, ρ - [kg/m^3]	1020	1040
Thermal conductivity, k_{cond} - [W/(mK)]	0.240	0.167
Thermal expansion, δ_{aT} - [1/°C]	1.0×10^{-4}	1.7×10^{-5}
Heat capacity, c_p - [J/(kg K)]	1200	1320
Surface tension, γ - [mN/m]	34.3	35.6
Young's Modulus, E - [MPa]	1650	1226
Poisson's ratio, ν - [-]	0.34	0.35
Chamber Temperature, T_c - [°C]	155	53
Pulse duration, t_L - [ms]	1	800
Laser radius R_L - [μm]	15	20
Laser irradiated energy, E_{in} - [μJ]	192	19 - 27

The pulse duration and laser irradiated energy in both experiments are different, as indicated in Table 3.1. In the case of PA12 particles, sintering occurred around the melting point ($T_{melt} \sim 180$ °C), predominantly during the cooling stage. This configuration closely approximates the thermal evolution of a real 3D printing process. Conversely, PS particles were sintered slightly above the glass temperature ($T_g \sim 62$ °C, $T_{melt} \sim 100$ °C) and during the pulse duration, while the laser was still active. This configuration facilitated a slower sintering process, while still imparting sufficient energy for particle pairs to undergo sintering under the influence of surface tension.

3.3. METHODS

This section describes the discrete element model (DEM) used to simulate the sintering of particles by a laser beam, which is based on momentum and heat balance [17, 19], implemented in MercuryDPM [20].

3.3.1. DEM AND HEAT TRANSFER

To model heat transfer using a DEM framework, the descriptions of conduction, convection and radiation proposed by Peng *et al.* [19] are utilized. The particles physically need to come into contact, see Fig. 3.2 (left). Conversion of heat and balance are employed to estimate the change of temperature of a particle i of radius R_i, with the assumption of no temperature gradient within a particle.

In the following, we will assume that the laser heat is applied instantaneously, and thus only affects the initial conditions. Therefore, we assume that there is no heat source and the evolution of particle temperature is described by
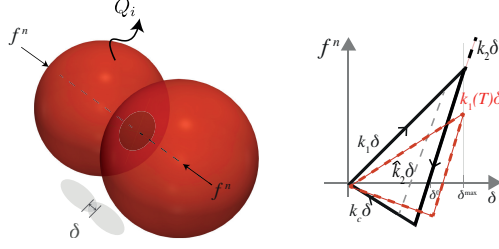
Figure 3.2: (Right) Two particle contact with overlap δ. (Left) Thermo visco-elastoplastic contact law. The contact displacement is related to δ (overlap) and the normal contact force f^n. Right/left-pointing arrows are used to distinguish the forces obtained during the loading and unloading stages, respectively. The dotted line represents the loading stiffness k_1 variation according to the increment of temperature T, k_2 is the unloading stiffness, k_c is the cohesive stiffness.

$$m_i c_{p,i} \frac{\mathrm{d} T_i}{\partial t} + \sum_{j=1}^{n} k_{i,cond}(T_j - T_i) \frac{a_{ij}}{l_{ij}} = Q_{i,conv} + Q_{i,rad}, \tag{3.1}$$

where m_i is the particle mass, $c_{p,i}$ is the heat of material, and T_i, T_j are the temperatures of particles i, j, respectively. k_{cond} is the conductivity of material, l_{ij} the distance between the centers of particles, Q_i represent the external heat fluxes associated to particle i by convection ($Q_{i,conv}$) and radiation ($Q_{i,rad}$) with units [W], and n is the number of interacting neighbors of particle i. The area of heat transmission, a_{ij}, can be correlated to the overlap $\delta_{ij} = (R_i + R_j) - (\mathbf{r}_i - \mathbf{r}_j) \cdot \mathbf{n}$, where $\mathbf{r}_i$ is the position of particle i with unit vector $\mathbf{n} = (\mathbf{r}_i - \mathbf{r}_j)/|\mathbf{r}_i - \mathbf{r}_j|$, and the effective particle radius $R_{ij} = R_i R_j / (R_i + R_j)$, so that:

$$a_{ij} \simeq 2\pi R_{ij} \delta_{ij}, \tag{3.2}$$

for $\delta_{ij} \ll R_{ij}$.

The convective heat transfer can be expressed as:

$$Q_{i,conv} = k_{i,conv} A_i (T_f - T_i), \tag{3.3}$$

where A_i is the surface area available on particle i, with T_i, $k_{i,conv}$ is the convective heat transfer coefficient, T_f is the surrounding temperature, and $Q_{i,conv}$ represents the heat flux of particle i with the environment.

The radiative heat transfer is expressed as:

$$Q_{i,rad} = \sigma \varepsilon A_i (T_{i,local}^4 - T_i^4), \tag{3.4}$$

where $\sigma = 5.67 \times 10^{-8}$ W/m^{2}K^4 is the Stefan-Boltzmann constant, ε represents the emissivity with dimensionless quantity, and $T_{i,local}$ is the temperature of the environment.

Subsequently, the motion of particles is solved based on Newton's equations of motion, where the corresponding translational and rotational degrees of freedoms are simultaneously updated with Eq. (3.1), which are expressed as,

$$m_i \ddot{r}_i = m_i g + \sum_j f_{ij}^n \qquad (3.5)$$

$$I_i \ddot{\theta}_i = \sum_j (r_{ij} \times f_{ij}^n), \qquad (3.6)$$

where $\ddot{r}_i$ is translational acceleration, m_i mass of the particle i, g acceleration due to gravity, f_{ij}^n force at contact with particles. $\ddot{\theta}_i$ is angular acceleration, r_{ij} the branch vector directed from the center of particle i to the contact point with particle j, and I_i is the mass moment of inertia of particle i.

For the inter-particle collision, the temperature dependence contact model proposed by Luding [17] is used, see Fig. 3.2, (right). The normal force f_{ij}^n describes the interaction as:

$$f_{ij}^n = \left\{ \begin{array}{ll} k_1(T)\delta_{ij} & \text{if } \delta_{ij} > \delta_{ij}^{\max} \\ k_2(\delta_{ij} - \delta_{ij}^0) & \text{if } \delta_{ij}^{\min} < \delta_{ij} \leq \delta_{ij}^{\max} \\ -k_c \delta_{ij} & \text{if } 0 < \delta_{ij} \leq \delta_{ij}^{min} \end{array} \right\} - f_{ij}^a - \eta^n v_{ij}^n. \qquad (3.7)$$

The computation of the repulsive visco-elastoplastic forces f_{ij}^n during sintering is governed by the loading stiffness $k_1(T)$. It decreases as T approaches the melting point of a material, and therefore, the material can deform significantly so that the contact area becomes larger at the contact. The dependency of k_1 on T may be described as:

$$k_1(T) = \frac{k_1}{2}\left[1 + \tanh\left(\frac{T_{\text{melt}} - T}{T_{\text{var}}}\right)\right], \qquad (3.8)$$

where T_{var} defines the range of temperatures in which the melting takes place. In the transition regime where $| T_{\text{melt}} - T | / T_{\text{var}}$, the particles are significantly softer than in the cold limit $T_{\text{melt}} - T \gg T_{\text{var}}$. Subsequently, the unloading process follows the slope of $\hat{k}_2$, which varies between $k_1(T)$ at a given temperature and a constant k_2, depending on the plastic deformation at zero force δ_{ij}^0. Note that k_2 is not changed directly when T increases. For overlaps smaller than $\delta_{ij}^{\max}$, the unloading stiffness is interpolated linearly between k_2 and $k_1(T)$ as:

$$\hat{k}_2 = \left\{ \begin{array}{ll} k_1(T) + (k_2 - k_1(T))\frac{\delta_{ij}^{\max}}{\phi_f R_{ij}} & \text{if } \delta_{ij}^{\max} < 2\phi_f R_{ij} \\ k_2 & \text{if } \delta_{ij} \geq \delta_{ij}^{\max} \end{array} \right\}, \qquad (3.9)$$

where $\phi_f = \sqrt[3]{2}$ and R_{ij} represents the effective particle radius. After the contact force becomes negative, for $\delta_{ij} < \delta_{ij}^0$, the model introduces a cohesive force limited by the cohesion stiffness k_c.

The additional adhesive force f_{ij}^a is assumed constant in Eq. (3.7). In the case of collisions of particles and large deformations, dissipation occurs due to the hysteretic

nature of the force-law described by a viscous, dissipative, velocity-dependent force $\eta^n v_{ij}^n$, with η^n as the viscous dissipation coefficient. This coefficient is related to the restitution coefficient e as $\eta^n = \sqrt{2mk_1}/(\sqrt{\pi} + \sqrt{\log e})\log e$, and therefore, this force-displacement model depends only on particle mass, not relative velocity[1].

Finally, if particles are heated, in general, their density increases. Thus, we assume that the particle radius changes in linear approximation as

$$R_i(T) = R_i(T_{\text{melt}})[1 + \delta a_T(T_{\text{melt}} - T)], \tag{3.10}$$

with the relative change of the radius per unit temperature δa_T.

3.3.2. CONTACT RHEOLOGICAL MODEL FOR POLYMER SINTERING

The sinter bonding of polymer particles occurs between their glass transition and melting points, resulting in the formation of necks that reduce surface area and lower surface energy. The necks grow through atomic-level transport of polymer chains along grain boundaries and bulk grain. Various mechanisms influence sintering, with visco-elastic deformation and viscous flow being the most dominant for polymer particles [21, 24, 25]. Fig. 3.3 illustrates the stages of a polymer sintering process.
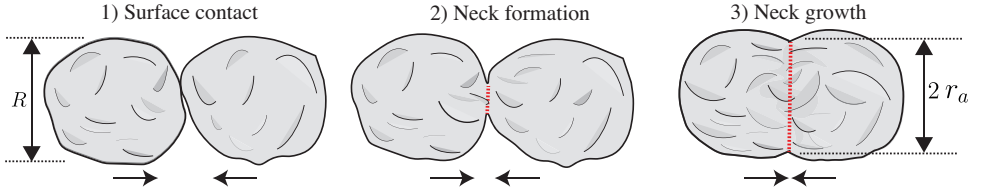
Figure 3.3: Schematic illustration of the polymer sintering process. 1) Surface contact. 2) Neck formation. 3) Neck growth. R represents particle radius, r_a is contact radius, with contact area $a_{ij} = \pi r_a^2$.

The mechanisms for the polymer sintering process involve three stages: surface contact, neck formation and neck growth. First, the surface contact represents the adhesion stage, in which the particles first attract each other via van der Waals adhesion forces. Second, neck formation occurs while the visco-elastic deformation is balanced by quick inter-surface adhesive forces during the material's unrelaxed state. The last stage corresponds to the relaxation of molecular rearrangement, and is related to the action of surface tension in the viscous flow regime. By defining the evolution of contact radius a_{ij}/R_{ij} during the three mentioned stages, it is possible to include each stage into a DEM approach correlating the particle-particle overlap δ_{ij} during the computation of the normal force f_{ij}^n, see Eq. (3.7). Our previous investigation has discussed mathematically a_{ij}/R_{ij} for polymer sintering, and therefore, the reader is referred to [21] for more details. Nonetheless and most important, the latest stage of the process (3) is improved with Frenkel-Pokluda model [26], leading to a temperature dependent fluidity $C_1(T)$[2]. Fig. 3.4 illustrates the sintering regime map, remarkably

---

[1]This is a particular case by assuming $k_1 = k_2$.
[2]Fluidity, C_1, is the term adopted to describe the non-opposition to flow

controlled by only one parameter $C_1(T)$ at the last stage.
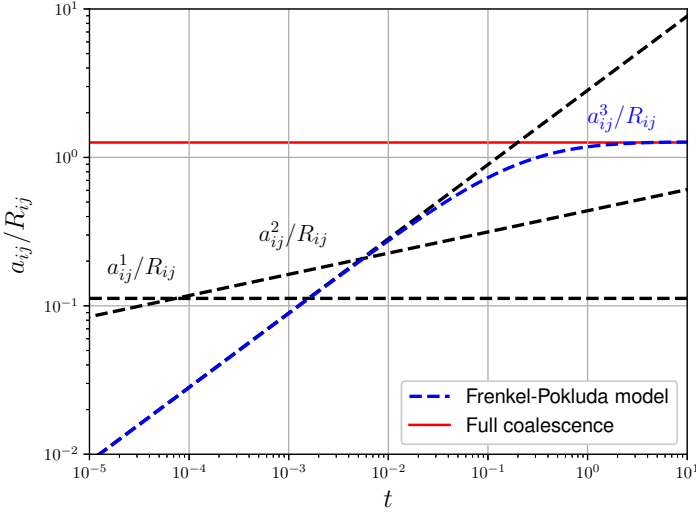
Figure 3.4: Sintering regime map with three mechanisms for flow simulation: (1) adhesive contact, (2) adhesive inter-surface forces, and (3) surface tension.

We briefly summarize the three-stage model. In stage 1, the non-dimensional neck radius a_{ij}^1/R_{ij} was derived by Johnson, Kendall, and Roberts [27] at very short times ($t \ll t_0$) for the equilibrium deformation of two elastic bodies under the influence of surface tension, as:

$$\frac{a_{ij}^1}{R_{ij}} = \left(\frac{9\pi(1-\nu^2)\gamma}{ER_{ij}}\right)^{1/3},$$ (3.11)

where γ is the surface tension, ν the Poisson's ratio, and E the Young's modulus.

In stage 2, for intermediate times in the interval $t_0 < t < t_{vis}$, the growth of contact radius a_{ij}^2 is predicted to be

$$\frac{a_{ij}^2}{R_{ij}} = \left(\frac{63\pi^3}{16}\right)^{1/7}\left(\frac{\delta_c}{R_{ij}}\right)^{2/7}\left(\frac{2C_1(T)\gamma t}{R_{ij}}\right)^{1/7},$$ (3.12)

where the separation distance δ_c is specified to ensure the work of adhesion, defined as the range of the adhesive force, and t is time.

The third stage is described using the Frenkel-Pokluda model [26], which describes the sintering process balancing the work of surface tension and viscous dissipation, expressed as:

$$\frac{a_{ij}^3}{R_{ij}} = \sin(\theta) \left[\frac{4}{(1+\cos(\theta))^2(2-\cos(\theta))} \right]^{1/3},$$ (3.13)

where the re-scaled time,

$$\theta = \left(\frac{8\gamma C_1(T) t}{R_{ij}} \right)^{1/2}.$$ (3.14)

To include a_{ij}^1, a_{ij}^2, and a_{ij}^3 in the contact description (Eq.(3.7)), we compute the rate of the plastic overlap $\dot{\delta}_{ij}^0$. Knowing that the overlap between the particles nearly equals the plastic overlap, $\delta_{ij} \approx \delta_{ij}^0$ for stiff particles ($k_1 \gg (f_{ij}^n + f_{ij}^a)/R_{ij}$), the contact radius may be approximated as $a_{ij}/R_{ij} \approx \sqrt{\delta_{ij}/R_{ij}}$ (small overlaps $\delta_{ij}^0 \ll R_{ij}$). It can be controlled by setting the growth rate $\dot{\delta}_{ij}^0$ according to Eq. (3.11), Eq. (3.12), and Eq. (3.13).

3.3.3. RAY TRACING APPROACH FOR LASER ENERGY ABSORPTION

An absorption model is needed to describe the interaction of a laser source and the particles. According to the Beer-Lamber law, the decrease of attenuation of the light intensity while propagating inside a material can be described as:

$$I(x) = I_0 e^{-\mu x},$$ (3.15)

where I_0 is the initial light intensity, μ represents the attenuation coefficient of a material, x is the path. Yaagoubi *et al.* [28] presented a model to describe the laser as a set of rays, where each ray is traced along the path that it follows, with step size Δl and by which particles it is absorbed until it is completely absorbed or has left the material. However, the equation only applies to 2D cases. In our study, the 3D equation to determine the starting intensity of each ray is based on a Gaussian laser profile, scaled such that the total intensity of all rays equals 1 and set to:

$$I_0\left(d, R_{laser}, N_{ray}\right) = \frac{2}{N_{ray}\left(1 - \frac{1}{e^2}\right)} e^{\frac{-2d^2}{R_{laser}^2}}, \text{ if } d < R_{laser}, 0 \; else,$$ (3.16)

where N_{ray} represents the number of rays, d is the distance from the laser centre perpendicular to the propagation direction, and R_{laser} is laser radius. The implemented ray tracing model, whose accuracy depends on the number of rays, step size Δl, and dissipation threshold $v_{threshold}$, is documented and can be downloaded via Github[3], and the details in Appendix 3.7.1. Fig. 3.5 illustrates the approach, implemented in MercuryDPM.

Since each simulation in the ray tracing approach is performed for a single time step, the simulations provide the amount of energy that particles absorb in each time step using the momentum of particle-particle interpenetration. This allows for the computation of the heating rate of a certain particle, which is given by,

---

[3]https://github.com/BertNijkamp/Laser-Beam-Absorption
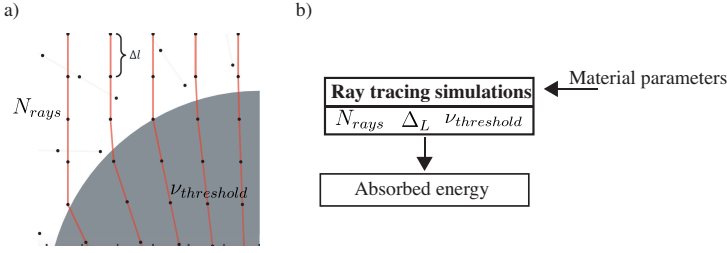
Figure 3.5: a) A laser beam represented by several light rays interacts with a particle, causing the rays to be split into reflected and refracted rays. b) The ray tracing simulation is set with material, laser parameters and model configuration such as the number of rays N_{rays}, step size Δl, dissipation threshold $\nu_{thershold}$.

$$\frac{\Delta T}{\Delta t} = \frac{E_{in} e_{abs}}{m c_p}, \tag{3.17}$$

where E_{in} is the total irradiated laser energy, e_{abs} the portion of absorbed energy out of the total incoming energy, Δt the time step, m and c_p are mass and heat capacity of the particle.

3.4. RESULTS AND DISCUSSION

This section presents a computational analysis of the contact rheology of visco-elastic powders during laser sintering, using the experimental data on PA12 and PS discussed in Sec. 3.2, and earlier reported in [21]. The analysis begins with ray tracing simulations to determine the amount of energy absorbed by the particles when irradiated by the laser beam. Next, the neck growth and the calibration procedure were used.

3.4.1. ABSORPTION ANALYSIS

To determine the portion of energy absorbed (e_{abs}) by particles while a laser beam irradiates the surface, ray tracing simulations are conducted (see Sec. 3.3.3). First, the refraction index and the attenuation coefficient of PA12 and PS are extracted from the literature [16, 29], as summarized in Table 3.2.

Table 3.2: Optical interaction coefficients.

Property, symbol - units	PA12	PS
Refraction index, n [-]	1.525	1.5997
Attenuation coefficient, μ [m^{-1}]	33500.0	27400.0

It is noticed that PA12 presents a larger attenuation coefficient compared to PS, i.e. the incident energy beam becomes more attenuated as it passes through the material, and therefore, more energy would be absorbed by this polymer per length. Subsequently, the laser spot radius is set to 15 μm and 20 μm for PA12 and PS, respectively, according

to the experimental data (Table 3.1). The laser beam has an angle of incidence of 60°
related to the particle bed surface normal. It is also assumed that the bed perfectly
reflects the light rays and the laser impacts precisely at the contact point of the two
adjacent particles. The temperature is homogeneously diffused inside the particles as
suggested by Balemans *et al.* [11]. Finally, the ray tracing discretization parameters are
set to $N_{rays} = 10000$, step size $\Delta l = 10\%$, and a dissipation threshold $\nu_{thresh} = 1\%$. The
parameters were tested and adjusted until the simulations converged with less than 1%
of variation. The ray tracing simulation for a PA12 particle pair is illustrated in Fig. 3.6.
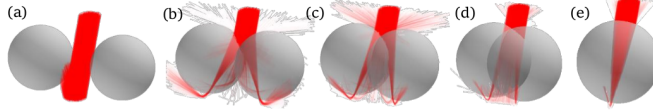
Figure 3.6: Ray tracing simulations for PA12 particle pairs, depicting incident beam rays onto two spherical
particles at different overlaps: (a) $\delta_{ij} = -1/3$, (b) $\delta_{ij} = 1/20$, (c) $\delta_{ij} = 1/3$, (d) $\delta_{ij} = 1/2$, (e) $\delta_{ij} = 1$.

Fig. 3.6 shows the simulation of ray tracing while particle pairs are overlapping from
$\delta_{ij} = -1/3$ to $\delta_{ij} = 1.0$, being δ_{ij} the relative overlap if positive. The simulation shows
differences in light reflection when the relative overlap is varied. For instance, a relatively
big portion of the energy is reflected away from the top at $\delta_{ij} = 1/20$, and the light rays
are more converging to each other when $\delta_{ij} \sim 1$. It is evidenced that the energy absorbed
by a polymer not only depends on the shape on which the laser impacts but also on the
amount of overlap caused by sintering. Subsequently, the absorbed energy portion e_{abs}
can be defined as a function of particle overlap, as depicted in Fig. 3.7.
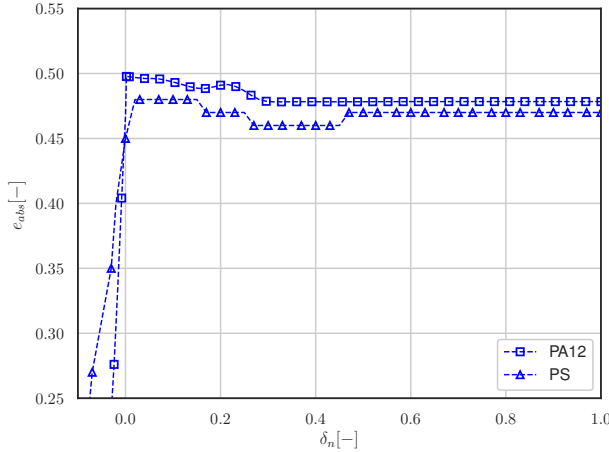
Figure 3.7: The absorbed energy portion of a particle in pair, as a function of overlap $\delta_n/2R$, where contacts
are positive. Squared shapes represent the results using PA12 properties while triangle shapes indicate the
computations using PS properties.

Fig. 3.7 shows that PA12 absorbs slightly more energy (2 ∼ 3%), as it attenuates stronger compared to PS. Furthermore, the two systems absorb the incident energy differently. For PA12, the highest absorption is identified at the initial contact $\delta_{ij} = 0$, and it decreases with particle overlap up to 30%, the moment at which the absorbed energy is constant, losing about 5% of the initial laser irradiated energy. For PS, the highest absorption is at the initial contact with $1 - 3\%$ of loss compared to the incident energy, it fluctuates, until reaching its asymptotic limit at $> 45\%$ of the overlap, leading to a 7% loss of total energy. The fluctuating behaviour in the case of PS material is the consequence of the smaller particle radius (60 μm), the lower attenuation coefficient, and also due to internal reflections of the beam inside the particle. It is relevant to mention that the curvature effect at the particle contact does not significantly affect light propagation. Since our ray tracing simulations are conducted for equal-sized spheres, the rays may bend uniformly. Future studies can focus on different particle sizes and the consequence bending of light.

The absorbed energy curves presented in Fig. 3.7 are set into MercuryDPM as polynomial coefficients, and once the sintering simulation starts, the temperature of the system is updated every time step according to the laser irradiated energy E_{in}, pulse duration t_L (reported in Table 3.1) and the modes of heat transfer (conduction, convection and radiation).

3.4.2. NECK GROWTH CONTACT RHEOLOGY

Laser sintering of powders is a multi-physics process that involves three different time scales. First, the time scale from the laser energy source, in which the laser is active. Here, we model the absorption process by the ray tracing approach, which assumed the absorption to occur instantaneously. Secondly, the time scale of heat diffusion, which is described throughout particle contacts using DEM for heat transfer problems. We also assume this process acts instantaneously and attributes an uniform temperature within each particle. Thirdly, the time scale from the neck formation, which is addressed by the current sintering regime map (Fig. 3.4). The later stage depends on the contact rheology of the material, and therefore it is strictly necessary to be defined as evidenced by experimental data [14, 16, 30].

The assumption of the uniform temperature inside each particle applies to all simulations. To determine the validity of this assumption, the thermal resistance of a polymer powder can be analysed based on the Biot number (Bi) [31, 32], being estimated as:

$$\text{Bi} = \frac{hL_c}{k_{cond}} = \frac{h(R/3)}{k_{cond}}, \tag{3.18}$$

where h is the heat transfer coefficient, L_c is the characteristic length scale which is defined as volume/surface area, and R is the particle radius. k_{cond} represents the thermal conductivity of the particle. For the case of PA12 and PS particles, $\text{B}_i \ll 0.1$, which indicates that the intraparticle heat transfer resistance is negligible compared to the external resistance around the particle [19]. In other words, the interior of the particles can be considered to be at a nearly uniform temperature.

Subsequently, to calibrate the contact rheology of PA12 and PS for sintering simulations, the open-source package GrainLearning [22] is utilized. It finds the most likely set of model parameters that reproduce the experimental data, based on constrained conditional probability distributions. The calibration package GrainLearning is a Bayesian calibration tool for estimating micro-parameter uncertainties in mechanical models. It uses the recursive Bayes' rule to quantify the evolution of the probability distribution of parameters over data history. The coupled implementation with MercuryDPM is illustrated in Fig. 3.8.
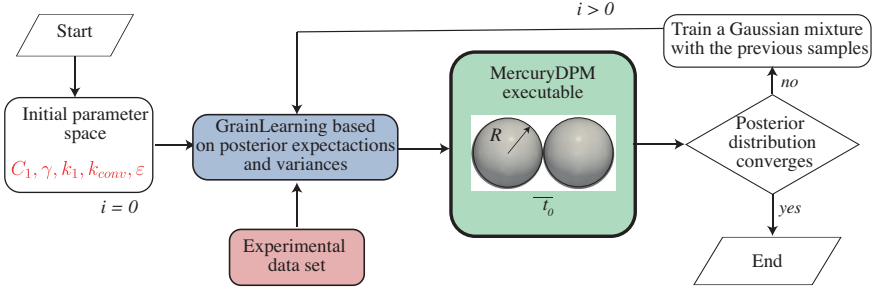
Figure 3.8: Flowchart illustrating the iterative coupled implementation using MercuryDPM and GrainLearning. The parameter space is initially set at iteration $i = 0$ and progressively updated until convergence is achieved.

Using the experimental data on *the evolution of the neck growth* and *temperature evolution* during laser sintering, reported by Hejmady *et al.* [14, 16], our DEM model requires the calibration of fluidity C_1, surface tension γ, loading stiffness k_1, thermal convectivity k_{conv} and emissivity ε. For this, an initial parameter space is defined as reported in Table 3.3.

Table 3.3: Parameter space

C_1 - [1/(Pa s)]	γ - [N/m]	k_1 - [N/m]	k_{conv} - [W/(mK)]	ε [-]
$0.001 - 0.1$	$0.01 - 0.05$	$0.0001 - 0.003$	$100 - 1000$	$0.1 - 1.0$

The remaining contact parameters are summarized in Table 3.4 [17, 33]

Table 3.4: System parameters

k_2 - [N/m]	k_c - [N/m]	δ_c - [1/m]	e -	ϕ [-]
$5.0\,k_1$	$2.0\,k_1$	$1.0/4.0R$	0.15	$\sqrt[3]{4}$

To simulate the visco-elastic sintering of polymer powders, a pair of 3D spheres of equal diameter is placed next to each other with negligible non-zero overlap between them, as visualized in Fig. 3.8. The particles are set just in contact at time t_0; the gravitational force is neglected. A small adhesive force $f^a = k_1 \delta_a$ is set to the particles to start the motion, where $\delta_a = 1.0$ mm. The range of softening is $T_{var} = 10$ °C with respect to the melting temperature of the material. Six iterations have been defined for the calibration procedure with eighty samples in each iteration for both PA12 and PS models. The

normalized covariance parameter at the first iteration is set to 0.7, resulting in an effective sample size of the Bayesian calibration larger than 20%. Fig. 3.9 shows the iterative calibration procedure for the PA12 model.
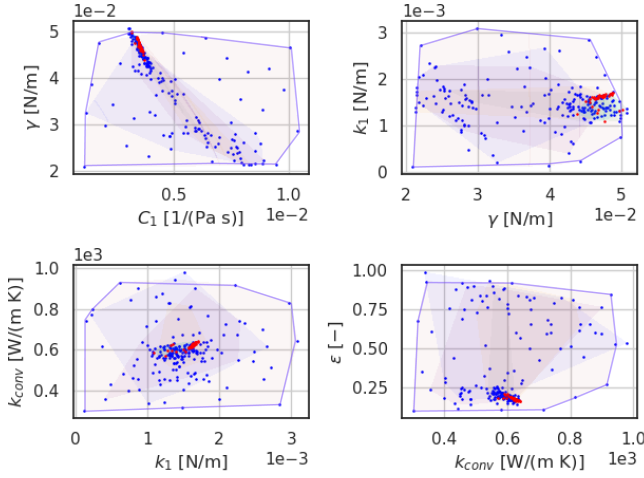
Figure 3.9: Calibration of model parameters for sintering simulations of PA12 particle pairs. Layers indicate the space of the parametric sample at every iteration, being the first layer of the initial parametric space. Blue dots represent the sample points, which progressively converge to a narrowed area. Red dots represent the last estimation of the parameters at the last iteration.

The illustration of the re-sampling process presented in Fig. 3.9 depicts the posterior modes localized progressively after each iteration. The agreement of the posterior expectations before and after one iteration of Bayesian filtering is adopted as the convergence criterion. The posterior expectation of each micro-parameter converges after the fifth iteration. Note that if the initial guesses for the model parameters are not able to capture at least one posterior distribution, the re-sampling scheme could explore outside the parameter ranges specified at the first iteration. Table 3.5 summarizes the calibrated parameters. Consequently, the DEM results are reported.

Table 3.5: Calibrated parameters

Property - units	PA12	PS				
Irradiated energy, E_{in} - [μJ]	**192.0**	**19.0**	**21.0**	**23.0**	**25.0**	**27.0**
C_1 - [1/(Pa s)]	3.41	0.03	1.92	7.36	21.51	72.8
γ - [mN/m]	48.56	50.09	42.42	42.19	25.72	24.71
k_1 - [mN/m]	1.67	0.11	0.11	0.12	0.12	0.148
k_{conv} - [W/(mK)]	635.73	304.10	334.4	301.11	309.2	304.74
ε [-]	0.164	0.21	0.275	0.76	0.805	0.814

It is noticed from Table 3.5 that surface tension corresponds to the expected ranges of calibration, and it increases according to lower irradiated energies, indicating that the

material opposes the flowability. Fig. 3.10 presents the calibrated simulation of PA12 particle pairs at different snapshots and temperature evolution.

Figure 3.10: Image sequence of sintering PA12 particles of radii R_i = 125 μm. Temperature evolution is recorded by the colour change from the first contact at t = 0.0 s to t = 0.7 s.

The simulation result of the temperature evolution on PA12 particles is presented in Fig. 3.11.
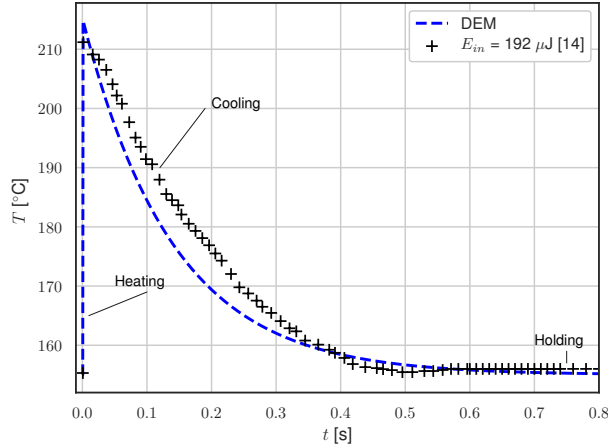
Figure 3.11: Temperature evolution while sintering PA12 particle pairs with E_{in} = 192 μJ. Initial temperature is set to T_0 = 155 °C. Cross markers correspond to the experimental data extracted from [14], while the dashed line is the DEM simulation results.

Three stages are indicated during thermal evolution. The heating stage, which increments quickly until the end of the pulse duration at t = 0.01 s. Then, the cooling stage starts from the maximum absorbed energy and decays exponentially to the initial or chamber temperature at 0.6 s. It happens because once the particle absorbs the incoming energy and the laser is switched off, the dissipation by radiation and convection reduces the temperature of the system until it reaches the initial conditions. The maximum temperature distributed within the particles when the laser impacts the surface is around 5% of loss over the irradiated energy. According to the characteristic time for heat diffusion t_{diff} [31], heat diffuses completely through the particles at t = 0.4 s, the moment at which the particles are to achieve the temperature of the

holding period as indicated by the experimental data. It is shown that the heat transfer model describes the experimental data relatively well, with only a slightly faster cooling than expected during the cooling stage.

Subsequently, the neck growth of particle pairs (Fig. 3.10) is computed and the results presented in Fig. 3.12.
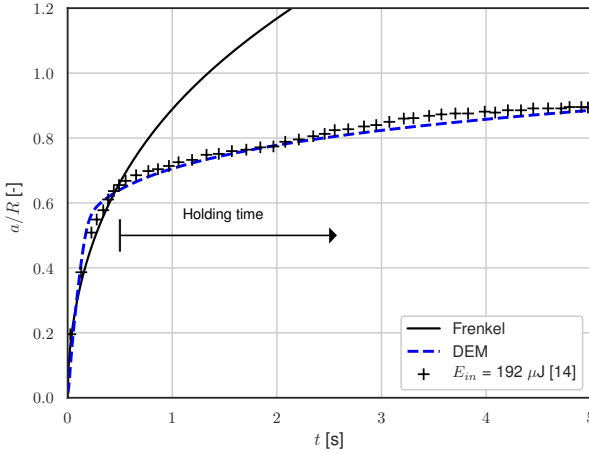
Figure 3.12: Neck growth of PA12 particle pairs. The dashed line corresponds to a calibrated DEM simulation, the solid line describes the modified Frenkel prediction using $\mu = 270$ Pa s, and crosses are the experimental data [14].

According to the experimental set-up, the sintering of PA12 particle pairs occurs principally during the holding stage ($t > 0.6$ s) after the temperature reaches the initial condition, as indicated by the horizontal arrow in Fig. 3.12. This is the consequence of letting the system remain at a temperature above the glass point, which allows the material to permanently deform under the influence of visco-plastic forces. Frenkel's model has been usually employed in the literature to describe sintering of particle pairs [34–36]. However, the model is only valid for the initial stage of the process as evidenced in Fig. 3.12, being fitted with a viscosity of $\mu = 270$ Pa s. Our proposed model evidences a better approximation during the whole process.

Similarly to PA12 particles, the simulations of PS pairs using the calibrated parameters reported in Table 3.5 are visualized in Fig. 3.13 and Fig. 3.15.

As visualized in Fig. 3.13, faster sintering and higher interpenetration are achieved when higher laser intensities are applied. The laser hits the interface of the particles at $t = 0$ s, and the neck is formed which tends to grow up to the pulse duration of the laser beam at 0.8 s. Following the absorption analysis and experimental information, irradiating 27 μJ on PS particle surface leads to the absorption of 93.7% of the incident energy. The energy absorbed under the different laser setups is summarized in Table 3.6.

The absorption analysis suggests that PS reflects around 6% of the incoming energy, which is 1% more than predicted by Hejmady *et al.* [16]; the authors measured
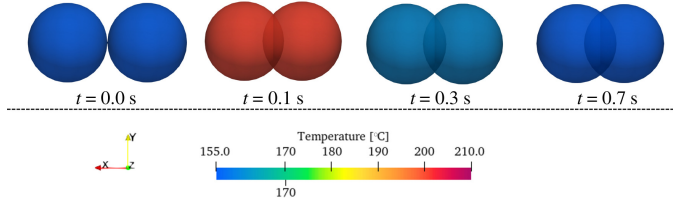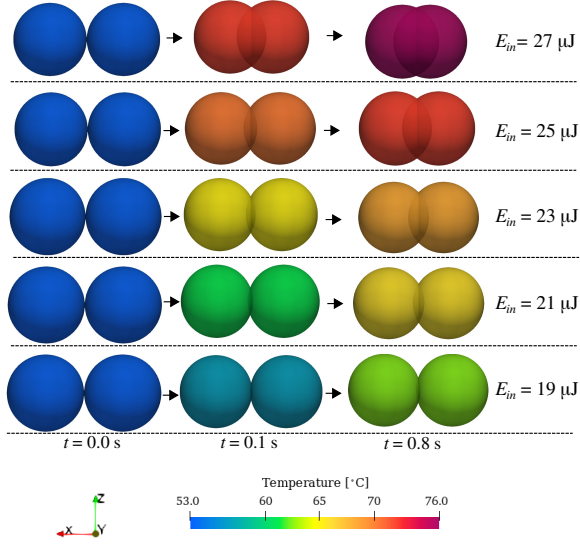
Figure 3.13: Imagine sequences of sintering PS particles of radii $R_i = 60$ μm. The temperature evolution is indicated by the colour change from the first contact at $t = 0.0$ s to $t = 0.8$ s, for different overlaps δ_{ij}.

Table 3.6: Comparison between laser irradiated energy and energy portion absorbed e_{abs} by particle pairs using the current ray tracing model.

E_{in} [μJ]	27.0	25.0	23.0	21.0	19.0
$e_{abs}E_{in}$ [μJ]	25.3	23.4	21.5	19.5	17.6
e_{abs} [%]	93.7	93.6	93.4	92.9	92.6

absorption on a flat polymeric surface.

The simulation result of the temperature evolution on PS particle pairs is presented in Fig. 3.14.

According to the experimental set-up, the sintering of PS particle pairs occurs slow and principally during the heating stage ($t < 0.8$ s). The DEM simulation and the absorption analysis predict the window in which the temperature evolves as a function of the irradiated laser energy, as reported by Hejmady *et al.* [16].

Subsequently, the evolution of the neck radius as a function of time is determined through particle-particle overlap. The result is presented in Fig. 3.15.

Fig. 3.15 shows the effect of laser energy on the sintering of particle pairs, which is maximum for the case of $E_{in} = 27$ μJ that leads to overlap of the particles of 90%; it reduces to around 25% when decreasing the irradiated energy to $E_{in} = 19$ μJ. The stress relaxation for flowability is achieved almost instantaneously after the consolidation starts letting surface tension dominate the process. This behaviour is expected since PS powders sinter faster compared to other polymers [21]. These simulations of particle pairs reveal the influence of the laser energy on the achieved neck radius. For the design of sintering procedures, a lower limit for solid-state sintering would be desirable
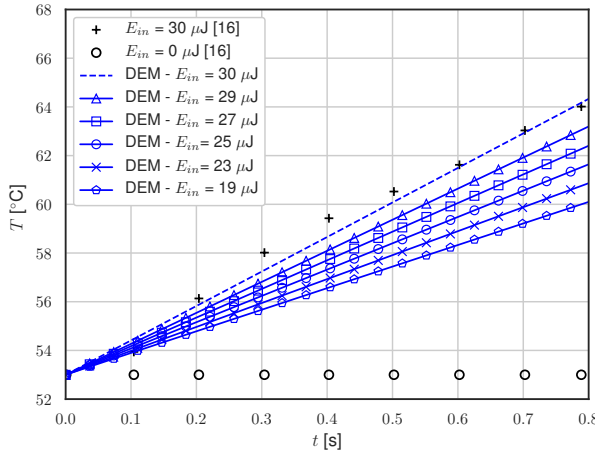
Figure 3.14: Temperature evolution while sintering PS particle pairs. Initial temperature is set to $T_0 = 53$ °C. Cross markers correspond to the data extracted from [16], while the dashed and marked lines are the DEM simulation results.
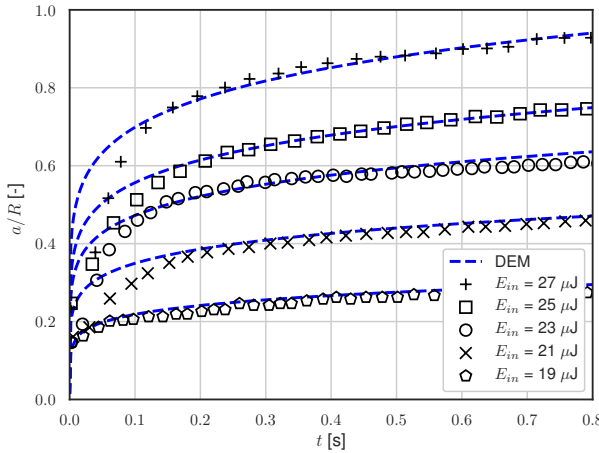
Figure 3.15: Neck growth of PS particle pairs as a function of time, for different applied laser energies. The dashed lines correspond to calibrated DEM simulations, symbols are the experimental data from [16].

$(a/R > 0.7)$ to avoid breakage. A deviation in the simulations and experimental data is evidenced in the early stage $t < 0.1$ s. One possible reason could be the recording process that limits measurements in short time frames.

Crystallization can occur during cooling if the rate of temperature decrease is too high, especially for semi-crystalline materials such as PS. Whereas the material contact

rheology determines the kinetics of the sintering of the neck region, the crystallization kinetics will affect the solidification. We have neglected in our model any crystallization effect for brevity, and future studies can discuss crystallization models to describe the aforementioned phase, such as the proposed by Shen *et al.* [37].

Raising the laser power also enhances the flowability of the particles, a trend supported by the model parameter fluidity denoted as C_1, which exhibits a notable increase with the rise in irradiated energy. This exponential relationship is depicted in Figure 3.16.

3
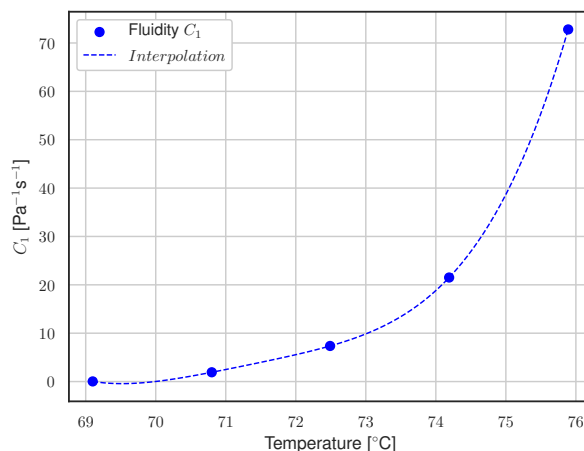
Figure 3.16: Temperature-dependent fluidity values, C_1, of PS fitted with an exponential regression (dotted line).

As the temperature within a polymer increases, the thermal energy of the polymer chains also increases, leading to an increase in the kinetic energy of the molecules. This causes the polymer chains to vibrate more vigorously and move more freely, which in turn reduces the entanglement and cross-linking of the chains. This decrease in inter-molecular forces reduces the viscosity of the polymer and increases its fluidity as illustrated in Fig. 3.16. The relationship between temperature and fluidity of polymers near their melting point can depend on several factors, including the specific polymer and its properties, such as molecular weight, degree of branching, and presence of cross-linking. Additionally, the conditions under which the polymer is being heated or cooled can affect its behaviour, including the heating rate and duration, as well as the cooling rate. However, these details are beyond the scope of this study.

3.4.3. A CASE STUDY: LASER SINTERING OF THIN POLYMER LAYERS

This section examines the application of laser sintering on thin polymer particle layers using the calibrated model discussed in Sec.3.4.2. To investigate the bulk behaviour, the temperature changes and average layer height are measured after subjecting surface particles to a localized thermal gradient due to energy input within the laser radius.

Thus, the linear shrinkage of the heat-affected zone (HAZ) in the z-direction and the evolution of the surface temperature is measured. The simulations take into account the effect of gravity ($g = 9.81$ m/s^2). Fig. 3.17 depicts the measuring zone and length parameters, assuming that the laser spot diameter is approximately equal to the hatch distance.
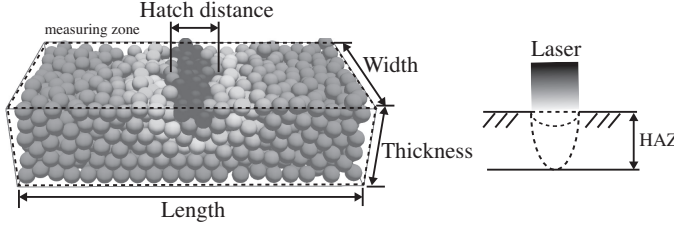
Figure 3.17: A schematic of the measuring zone for simulations of laser sintering of thin polymer layers.

To analyse the densification of thin polymer layers, a domain of width = 5 mm L_x, length = 1 mm (L_y), and thickness = 1.25 mm (L_z) is simulated. These dimensions are chosen to ensure that the system encompasses the relevant laser, diffusion, and sintering time and length scales.

The energy density resulting from laser irradiation is calculated using the equation:

$$E_A = \frac{E_{in}(1 - R_L)}{h_L \, v_L},$$ (3.19)

where E_{in} represents the total laser irradiated power per area, R_L is the reflectance, h_L is the hatch distance, and v_L is the scan speed. It is assumed that particles within the hatch distance absorb the same amount of energy as particle pairs in simulations (refer to Fig. 3.7). We simulate particle beds made from two different materials, PA12 and PS. Table 3.7 provides a summary of the process parameters.

Table 3.7: Process parameters

Material	PA12	PS
Hatch distance, h_L - μm	250.0	120.0
Pulse duration, t_L - ms	1.0	1.0
Reflectance, R_L - [−]	0.05	0.06

Fig. 3.18 presents the simulation results obtained using the calibrated contact properties of PA12 under different laser intensities.

In the simulations, the surface particles within the hatch distance are exposed to various laser intensities and pulse duration, see Table 3.7. The thickness of the HAZ is influenced by the irradiated energy E_{in}, as depicted in Fig. 3.18. It is observed that at low values of irradiated energy, the HAZ and the layer height exhibit similar behaviour. However, for laser intensities above 800 μJ, the difference between the initial and final shrinkage becomes evident, indicating the sintering of the particles. Fig. 3.19 illustrates
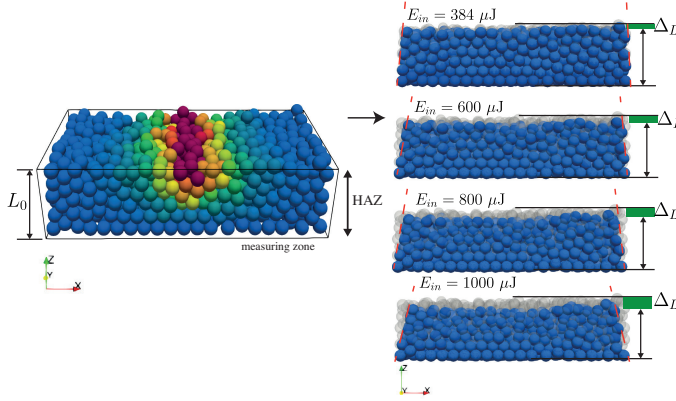
Figure 3.18: Simulation results for a thin PA12 layer under the influence of energy area density E_{in}. ΔL represents the height change measured at the heat-affected zone (HAZ) at the last time step.

the numerically calculated temperature evolution over time for different irradiated laser intensities on a PA12 layer.
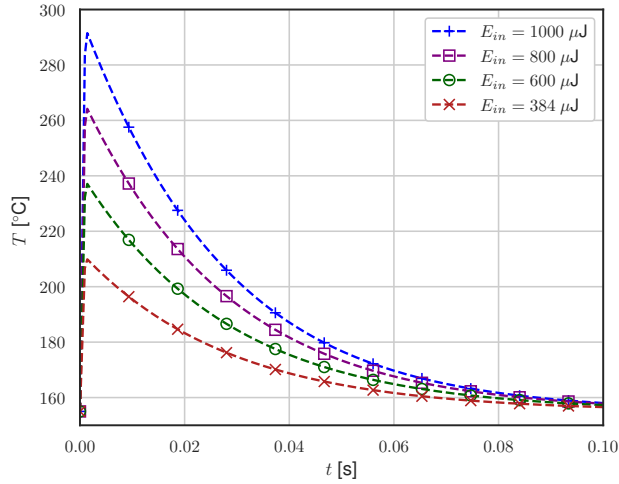
Figure 3.19: Temperature evolution (hatch distance) as a function of time for different irradiated energies on a PA12 layer.

Once the maximum temperature is reached based on the irradiated energy, the temperature gradually decreases and approaches the external temperature of the system, $T_0 = 155$ °C. During this cooling period, energy is released from the system through convection (more dominant) and radiation. The convection and radiation effects are likely overestimated because we do not account for the heating up of the gas phase; i.e. it is assumed that the system does not exchange energy with the

surroundings. It is observed that increasing the laser energy, such as to 1000 μJ, leads to a faster cooling rate $1/t_r$ of approximately e^{t/t_r}, where $t_r = 4R\eta/3\gamma$, γ is surface tension, R is radius, and η is viscosity. This phenomenon can be primarily attributed to the increased maximum temperature and the larger temperature difference with the powder bed.

Subsequently, the final shrinkage of the thickness ($\Delta L/L_0$) can be analytically estimated with the Mackenzie-Shuttleworth sintering model based on surface tension [38, 39], it is:

$$\frac{\rho}{\rho_0} = e^{\frac{-3\gamma t}{4R\eta}}\left(\frac{\rho_B}{\rho_0} + 1\right), \quad \frac{\rho}{\rho_0} = \frac{1}{\left(1 - \frac{\Delta L}{L_0}\right)^3}, \tag{3.20}$$

where ρ_0 is the green or solid density, ρ_B is the powder bulk density. The values are extracted from [38]. Fig. 3.20 displays the results for the average shrinkage of the heat-affected zone (HAZ) as a function of energy area density E_A.
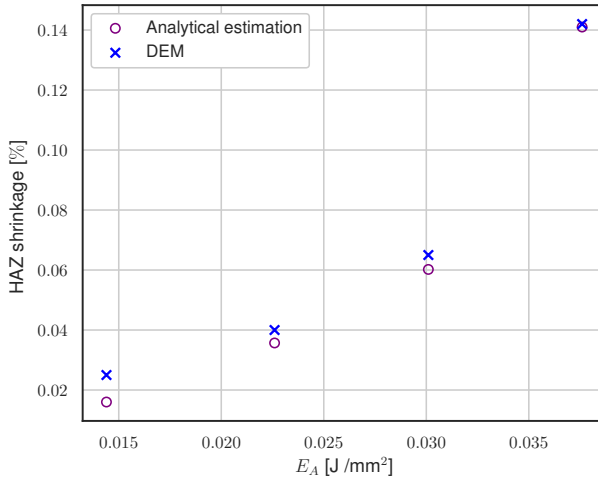
Figure 3.20: Shrinkage of the heat-affected zone (HAZ) as a function of energy area density E_A of a PA12 layer. The crossed shapes represent the results obtained from discrete element method (DEM) simulations, while the circles represent the analytical estimation.

The shrinkage of the heat-affected zone (HAZ) exhibits an exponential relationship with the increase in energy density. It reaches a shrinkage of approximately 14% when the energy density range is 0.04 J/mm^2. For small energy density values and quick interaction times, the heat diffusion occurs predominantly in ($x - y$) plane, normal to the z-direction. This phenomenon can be attributed to its low conductivity and diffusivity, which effectively confines the heat to the irradiated area, as described by Franco *et al.* [40], providing a reasonable explanation for the simulation results.

The analytical estimation of the HAZ shrinkage is calculated based on the viscous flow mechanism proposed by Frenkel [25]. However, it underestimates the shrinkage by 3.7%

because the model does not account for the flowability of polymers as a function of time, which is primarily governed by their temperature-dependence contact mechanics. The viscosity ranges used in the analysis were extracted from the work of Balemans *et al.* [11].

Similarly, the shrinkage behaviour of a PS powder layer is investigated. Fig. 3.21 illustrates the temperature evolution of the system for different irradiated energies.
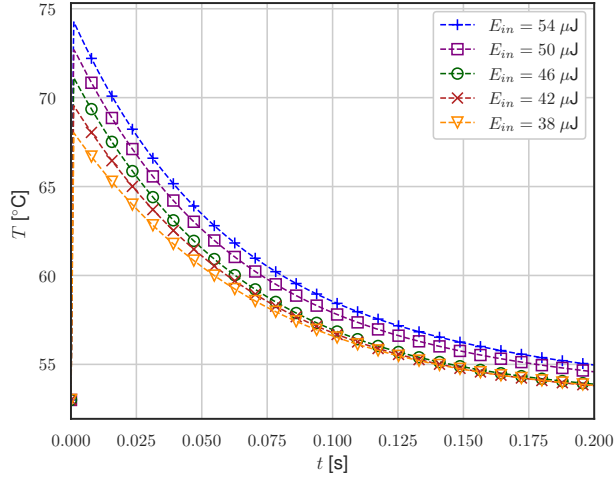
Figure 3.21: Temperature evolution (hatch distance) over time for different irradiated energies on a PS (polystyrene) sample.

Fig. 3.21 presents the temperature evolution during the sintering process. In comparison to Fig. 3.19 for the PA12 sample, the PS system absorbs the maximum energy at t = 1.0 ms, leading to the highest temperature achieved for the given irradiated laser energy. From an experimental perspective, if the PS system absorbs the same energy as the particle pair experiment (see Fig. 3.15), the scan speed of the laser would have to increase significantly to reach speeds up to 1000 m/s. This scanning rate is exceptionally high compared to the conventional speed at which the laser operates, $v_t = 0.01 - 1.0$ m/s. It can cause particles to experience significant displacement as they may be ejected from the target surface or vaporize. The simulation further indicates that thermal diffusion occurs within microseconds, as evidenced by the surface temperature reaching the initial temperature at t = 0.2 s. Fig. 3.22 displays the results for the average shrinkage of the heat-affected zone (HAZ) as a function of energy area density E_A on a PS layer.

Fig. 3.22 reveals that the shrinkage of the heat-affected zone (HAZ) increases as a function of energy density E_A. When the surface absorbs 0.41 J/mm^2, the HAZ can compact by approximately 16.5%. For the case of PS, with an increase in laser energy of 4 μJ, the HAZ experiences an additional 2% shrinkage. However, it should be noted that the shrinkage increases exponentially for energy densities above 0.036 J/mm^2.
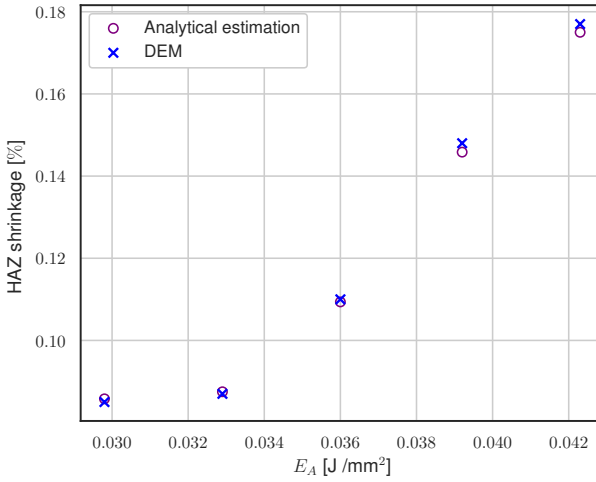
Figure 3.22: Shrinkage of the heat-affected zone (HAZ) as a function of energy density E_A on a PS (polystyrene) layer. The circles represent the analytical estimation, while the crossed shapes represent the results obtained from discrete element method (DEM) simulations.

3.5. CONCLUSIONS AND OUTLOOK

In this study, we developed a numerical approach utilizing the discrete element method (DEM) to analyse the laser sintering process with a specific emphasis on neck growth contact rheology. This approach was integrated into the MercuryDPM software package.

First, we collected reported experimental data related to laser sintering. The experiments recorded the neck growth and temperature evolution of PA12 and PS particle pairs undergoing sintering via laser beam; for PA12, this occurred above the melting point, whereas for PS, it took place above the glass transition temperature.

Second, we developed a multi-physics DEM model. This model accounted for the intricate thermal energy balance resulting from particle contact with thermal disruption, including mechanisms such as conduction, convection, and radiation. Additionally, we incorporated the external influence of a laser beam through a ray tracing approach. To enhance the capability of our model, we introduced a novel sintering description that encompasses three distinct mechanisms to simulate the contact rheology of visco-elastic particles.

Then, guided by the experimental data, we conducted simulations using the GrainLearning package. These simulations required the calibration of model parameters, including surface tension, stiffness, thermal convection, emissivity, and fluidity. The outcomes of these simulations presented good agreement with the temperature evolution recorded experimentally, as well as the dependence of energy absorption on facilitating neck growth on the particle pairs. Notably, our investigation

revealed that fluidity, a key parameter controlling sintering rates, exhibited exponential behaviour concerning high temperatures. It paves the way for further exploration of laser sintering simulations via the proposed approach.

Finally, the calibrated DEM approach of pairs in contact was applied to analyse the sintering of thin PA12 and PS layers. The axial shrinkage (HAZ shrinkage) of the layers contracted as a function of the energy inputs, paving the way to analyse the relation between process and material parameters during laser sintering.

Further work can focus on exploring the influence of different mechanical properties like crystallinity, and particle properties such as particle size, poly-disperse size distributions, and the bulk volume fraction on sintering. Additionally, the proposed approach could be extended to sintering processes for metallic and ceramic powders and multiple layers of heterogeneous powders.

3.6. ACKNOWLEDGMENTS

3.7. APPENDICES

3.7.1. APPENDIX: 3D IRRADIATED ENERGY EQUATION

The energy intensity of each ray depends on the distance to the centre of the beam,

$$I_0(d,\sigma) = \frac{1}{\sigma\sqrt{2\pi}} e^{\frac{-d^2}{2\sigma^2}}, \tag{3.21}$$

with d the distance from the laser centre perpendicular to the propagation direction and σ the standard deviation, which is half the laser radius in this situation. However, this equation only applies for 2D: it has a surface area of 1 when integrating from $-\infty$ to ∞. In 3D, the equation needs to be rotated around the axis parallel to the propagation direction and integrated from 0 to 2σ, then the volume needs to be 1:

$$V = \int_0^{2\sigma} 2\pi d \cdot I(d,\sigma)\, \mathrm{d}d = \int_0^{2\sigma} \frac{2\pi d}{\sigma\sqrt{2\pi}} e^{\frac{-d^2}{2\sigma^2}}\, \mathrm{d}d = \int_0^{2\sigma} \frac{d\sqrt{2\pi}}{\sigma} e^{\frac{-d^2}{2\sigma^2}}\, \mathrm{d}d, \tag{3.22}$$

$$u = \frac{-d^2}{2\sigma^2}, \ \mathrm{d}u = \frac{-d}{\sigma^2}\mathrm{d}d, \tag{3.23}$$

$$V = \int_0^{2\sigma} -\sigma\sqrt{2\pi} e^u\, \mathrm{d}u = \left[-\sigma\sqrt{2\pi} e^{\frac{-d^2}{2\sigma^2}} \right]_0^{2\sigma} = \\ -\sigma\sqrt{2\pi} e^{\frac{-4\sigma^2}{2\sigma^2}} + \sigma\sqrt{2\pi} e^0 = \sigma\sqrt{2\pi}\left(1 - e^{-2}\right), \tag{3.24}$$

Which is not equal to 1. Therefore, Eq. (3.21) needs to be divided by $\sigma\sqrt{2\pi}\left(1 - e^{-2}\right)$:

$$I(d,\sigma) = \frac{1}{2\pi\sigma^2\left(1-e^{-2}\right)}e^{\frac{-d^2}{2\sigma^2}}, \tag{3.25}$$

In here, 2σ can be replaced by the laser radius r_{radius}:

$$I(d,r_{laser}) = \frac{2}{\pi r_{laser}^2\left(1-e^{-2}\right)}e^{\frac{-2d^2}{r_{laser}^2}}. \tag{3.26}$$

When considering rotation around an axis parallel to the laser beam's propagation direction and integrating from 0 to r_{laser}, this procedure does yield a result of 1 in terms of volume. However, in our simulations, where the laser beam is discretized into many light rays, it is essential to ensure dimensional consistency. Therefore, when assigning energy to each light ray based on its location within the laser beam, we must multiply the energy by an appropriate length parameter, rather than an area, to create a volume-like quantity. This ensures that the total sum of energies across all rays equals 1. The correct length parameter to use is the diameter of the laser beam, $2r_{\text{laser}}$, rather than the average area. Hence, the equation employed in our simulations to determine each ray's individual energy is as follows:

$$I_0\left(d, r_{laser}, N_{ray}\right) = \frac{2}{N_{ray}\left(1-e^{-2}\right)}e^{\frac{-2d^2}{r_{laser}^2}}. \tag{3.27}$$

When creating the starting coordinates of the light rays, each ray is given the following information:

- A coordinate, which is randomly chosen in a circle with radius r_{laser} just above the bed

- A direction vector, for example pointing downwards: [0 0 -1]

- A position-dependent energy according to Eq. 3.27

REFERENCES

[1] S. C. Ligon, R. Liska, J. Stampfl, M. Gurr, and R. Mülhaupt, *Polymers for 3D printing and customized additive manufacturing,* Chemical reviews **117**, 10212 (2017).

[2] P. Rando and M. Ramaioli, *Numerical simulations of sintering coupled with heat transfer and application to 3D printing,* Additive Manufacturing **50**, 102567 (2022).

[3] Q. Meng, X. Song, S. Han, F. Abbassi, Z. Zhou, B. Wu, X. Wang, and S. Araby, *Mechanical and functional properties of polyamide/graphene nanocomposite prepared by chemicals free-approach and selective laser sintering,* Composites Communications **36**, 101396 (2022).

[4] D. M. Sassaman, M. S. Ide, J. J. Beaman, and D. Kovar, *A model for bonding mechanisms in indirect laser powder bed fusion of nylon/alumina blends,* Additive Manufacturing **59**, 103163 (2022).

[5] C. Bierwisch, S. Mohseni-Mofidi, B. Dietemann, M. Gruenewald, J. Rudloff, and M. Lang, *Universal process diagrams for laser sintering of polymers,* Materials & Design **199**, 109432 (2021).

[6] B. J. Dorussen, M. G. Geers, and J. J. Remmers, *A discrete element framework for the numerical analysis of particle bed-based additive manufacturing processes,* Engineering with Computers **38**, 1 (2022).

[7] R. Ganeriwala and T. I. Zohdi, *A coupled discrete element-finite difference model of selective laser sintering,* Granular Matter **18**, 21 (2016).

[8] K. Shinagawa, *Simulation of grain growth and sintering process by combined phase-field/discrete-element method,* Acta Materialia **66**, 360 (2014).

[9] S. Nosewicz, J. Rojek, M. Chmielewski, K. Pietrzak, and D. Lumelskyj, *Application of the Hertz formulation in the discrete element model of pressure-assisted sintering,* Granular Matter **19**, 1 (2017).

[10] T. Mukherjee, W. Zhang, and T. DebRoy, *An improved prediction of residual stresses and distortion in additive manufacturing,* Computational Materials Science **126**, 360 (2017).

[11] C. Balemans, M. A. Hulsen, and P. D. Anderson, *On the validity of 2D analysis of non-isothermal sintering in SLS,* Chemical Engineering Science **213**, 115365 (2020).

[12] C. Körner, F. Osmanlic, D. Drummer, K. Wudy, T. Laumer, and M. Schmidt, *Modeling of laser beam absorption in a polymer powder bed,* Polymers **10**, 784 (2018).

[13] L. Dong, A. Makradi, S. Ahzi, Y. Remond, and X. Sun, *Simulation of the densification of semicrystalline polymer powders during the selective laser sintering process: Application to nylon 12,* Polymer Science Series A **50**, 704 (2008).

[14] P. Hejmady, L. C. van Breemen, D. Hermida-Merino, P. D. Anderson, and R. Cardinaels, *Laser sintering of PA12 particles studied by in-situ optical, thermal and X-ray characterization,* Additive Manufacturing **52**, 102624 (2022).

[15] N. D. Polychronopoulos, I. E. Sarris, and J. Vlachopoulos, *A viscous sintering model for pore shrinkage in packings of cylinders,* Rheologica Acta **60**, 397 (2021).

[16] P. Hejmady, L. C. Van Breemen, P. D. Anderson, and R. Cardinaels, *Laser sintering of polymer particle pairs studied by in situ visualization,* Soft Matter **15**, 1373 (2019).

[17] S. Luding, K. Manetsberger, and J. Müllers, *A discrete model for long time sintering,* Journal of the Mechanics and Physics of Solids **53**, 455 (2005).

[18] S. Luding, *Cohesive, frictional powders: contact models for tension,* Granular matter **10**, 235 (2008).

[19] Z. Peng, E. Doroodchi, and B. Moghtaderi, *Heat transfer modelling in discrete element method (DEM)-based simulations of thermal processes: Theory and model development,* Progress in Energy and Combustion Science **79**, 100847 (2020).

[20] T. Weinhart, L. Orefice, M. Post, M. P. van Schrojenstein Lantman, I. F. Denissen, D. R. Tunuguntla, J. M. Tsang, H. Cheng, M. Y. Shaheen, H. Shi, P. Rapino, E. Grannonio, N. Losacco, J. Barbosa, L. Jing, J. E. Alvarez Naranjo, S. Roy, W. K. den Otter, and A. R. Thornton, *Fast, flexible particle simulations — An introduction to MercuryDPM,* Computer Physics Communications **249**, 107129 (2020).

[21] J. Alvarez, H. Snijder, T. Vaneker, H. Cheng, A. Thornton, S. Luding, and T. Weinhart, *Visco-elastic sintering kinetics in virgin and aged polymer powders,* Powder technology **397**, 117000 (2022).

[22] H. Cheng, T. Shuku, K. Thoeni, P. Tempone, S. Luding, and V. Magnanimo, *An iterative Bayesian filtering framework for fast and automated calibration of DEM models,* Computer Methods in Applied Mechanics and Engineering **350**, 268 (2019).

[23] P. Hartmann, H. Cheng, and K. Thoeni, *Performance study of iterative Bayesian filtering to develop an efficient calibration framework for DEM,* Computers and Geotechnics **141**, 104491 (2022).

[24] S. Li, J. S. Marshall, G. Liu, and Q. Yao, *Adhesive particulate flow: The discrete-element method and its application in energy and environmental engineering,* (2011).

[25] S. Kang, *Sintering: densification, grain growth and microstructure* (Elsevier Science, Korea, 2004).

[26] O. Pokluda, C. T. Bellehumeur, and J. Vlachopoulos, *Modification of Frenkel's model for sintering,* AIChE Journal **43**, 3253 (1997).

[27] K. Johnson, K. Kendall, and A. Roberts, *Surface energy and the contact of elastic solids,* Proceedings of the Royal Society of London. A. Mathematical and Physical Sciences **324**, 301 (1971).

[28] H. Yaagoubi, H. Abouchadi, and M. Taha Janan, *Simulation of the heat laser of the selective laser sintering process of the polyamide 12,* E3S Web of Conferences **297**, 01050 (2021).

[29] N. Sultanova, S. Kasarova, and I. Nikolov, *Dispersion proper ties of optical polymers,* Acta Physica Polonica-Series A General Physics **116**, 585 (2009).

[30] S. Berretta, Y. Wang, R. Davies, and O. R. Ghita, *Polymer viscosity, particle coalescence and mechanical performance in high-temperature laser sintering,* Journal of Materials Science **51**, 4778 (2016).

[31] W. M. Rohsenow, J. P. Hartnett, and Y. I. Cho, *Handbook of heat transfer* (McGraw-Hill New York, US, 1998).

[32] R. Ganeriwala and T. I. Zohdi, *Multiphysics modeling and simulation of selective laser sintering manufacturing processes,* Procedia Cirp **14**, 299 (2014).

3

[33] Y. Y. Lin, C. Y. Hui, and A. Jagota, *The role of viscoelastic adhesive contact in the sintering of polymeric particles,* Journal of Colloid and Interface Science **237**, 267 (2001).

[34] J. Frenkel, *Viscous flow of crystalline bodies under the action of surface tension,* Journal of Phyiscs **9**, 385 (1945).

[35] C. T. Bellehumeur, M. Kontopoulou, and J. Vlachopoulos, *The role of viscoelasticity in polymer sintering,* Rheologica Acta **37**, 270 (1998).

[36] M. Zhao, D. Drummer, K. Wudy, and M. Drexler, *Sintering study of polyamide 12 particles for selective laser melting,* International Journal of Recent Contributions from Engineering, Science & IT (iJES) **3**, 28 (2015).

[37] F. Shen, W. Zhu, K. Zhou, and L.-L. Ke, *Modeling the temperature, crystallization, and residual stress for selective laser sintering of polymeric powder,* Acta Mechanica **232**, 3635 (2021).

[38] M. Grünewald, K. Popp, J. Rudloff, M. Lang, A. Sommereyns, M. Schmidt, S. Mohseni-Mofidi, and C. Bierwisch, *Experimental, numerical and analytical investigation of the polyamide 12 powder bed fusion with the aim of building dimensionless characteristic numbers,* Materials & Design **201**, 109470 (2021).

[39] S. Singh, A. Sachdeva, and V. S. Sharma, *Optimization of selective laser sintering process parameters to achieve the maximum density and hardness in polyamide parts,* Progress in Additive Manufacturing **2**, 19 (2017).

[40] A. Franco and L. Romoli, *Characterization of laser energy consumption in sintering of polymer based powders,* Journal of Materials Processing Technology **212**, 917 (2012).

4

DENSIFICATION OF VISCO-ELASTIC POWDERS DURING FREE AND PRESSURE-ASSISTED SINTERING

This study provides a computational model to analyse densification of visco-elastic powders during sintering. It includes the discrete method (DEM) for thermo-mechanical problems, and a rheological model to describe the rate of sintering when visco-elastic particles overlap. First, a novel rheological contact model is developed and calibrated using experimental data obtained from dilatometeric experiments on PA12 pellets. The calibration process involves measuring the linear (axial) shrinkage of compacted powder pellets by dilatometers, instrument that measures the volume changes caused by temperature increments. This calibration step shows that our proposed model predicts the linear shrinkage of the PA12 pellets, particularly in proximity to the material's melting point. Subsequently, the study investigates the impact of process parameters on the evolution of bulk density, referred to relative density. The tests evaluates the effect of maximum process temperature, holding time, process time, and the dependence of external pressure. The findings indicate that longer process times and the application of external pressure play significant roles to promote densification. These findings contribute to a better understanding of densification of visco-elastic powders, and provide a tool for analysis the process through DEM models.

4.1. INTRODUCTION

Sintering is a widely used manufacturing process that involves the consolidation and bonding of powder, resulting in the formation of a solid object. During this process, the powder material can undergo two key phenomena: dilation or contraction. Dilation occurs under shear, but also as necks form between contacting particles and the material expands. Contraction arises from ongoing neck growth and the consequent void elimination and reduction of porosity. The two phenomena lead to the change of bulk density, which is typically named as **densification**. Understanding densification is crucial for achieving high-density and low-porosity sintered materials, with significant importance in various industries. For example, the industry relies on sintering to produce materials with high strength and exceptional thermal properties [1–3]. Likewise, sintering plays a critical role in manufacturing low-porosity objects that exhibit favourable dielectric and piezoelectric properties [4, 5]. Furthermore, in the field of additive manufacturing, comprehending how heat distribution affects the densification of powder-based samples may provide valuable insights into the understanding of the influence of material and process parameters [6]. Fig. 4.1 illustrates the different stages of densification during sintering using a simple lattice configuration of particles.

Densification during sintering can be categorized into three distinct stages: neck growth, the evolution of pores, and pore closure [7]. The process initiates from the green or apparent density, which represents the volume fraction occupied by the powder material, considering both the particles' volume and the occupied mass. As the temperature increases, necks among particles begin to grow at the contact area, accounting for approximately 3% densification relative to the apparent density. Subsequently, the pores among particles get close to each other by the growth of the contact area among the particles, contributing to nearly 90% of densification. Finally, the pores reach a state of isolation, leading to a higher-density material.
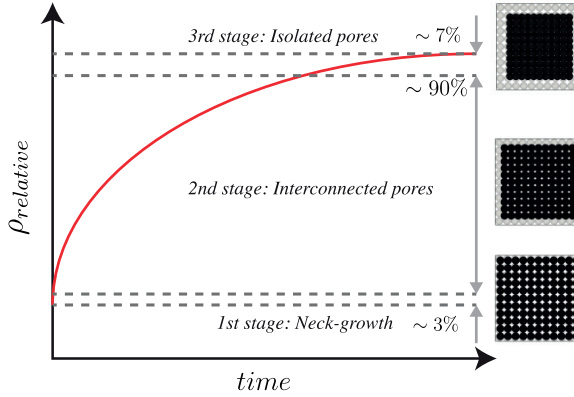
Figure 4.1: Densification during sintering.

Densification of powder materials during sintering has been extensively investigated using the discrete element method (DEM) by various researchers [8–15]. For example, Nosewicz *et al.* [9] studied pressure-assisted sintering of NiAl powder to describe densification using a two-elastic contact model, which was validated against experimental data. Similarly, Ivannikov *et al.* [11] combined DEM with solid-state diffusion equations to simulate the early stage of densification of metallic powder. Iacobellis *et al.* [12] developed a DEM model to investigate densification, elasticity, and temperature variations of particles, incorporating a weighted transition between a Hertz-Mindlin type contact and a sintering model during the heating stage.

Complementary to the aforementioned studies, this work presents a novel DEM approach that specifically focuses on the contact rheology of visco-elastic powder materials to describe densification during sintering. Our approach investigates the process through a material parameter called fluidity, which is incorporated through the contact overlap to control the rate of sintering [16]. The temperature and pressure contact model is implemented in MercuryDPM [17], calibrated with GrainLearning [18, 19], and used to analyse the experiments of dilatometric data of PA12 pellets. The results demonstrate that an accurate numerical description of the linear shrinkage of PA12 pellets is achieved, and the capability of the model for describing the influence of temperature and pressure on the process.

4.2. EXPERIMENTAL INVESTIGATION

To analyse the densification of powder material experimentally, pellets of PA2200 are analysed under dilatometric experiments. The experiment provides the measurement of the linear (axial) shrinkage, and therefore, the change of density can be computed; as relative density. The powder is supplied by EOS E-Manufacturing Solutions. Table 4.1 summarizes the properties.

The powder is in a pristine white state with an average particle diameter of 30 μm. First, cylindrical pellets of 16.17 mm in diameter and 5.71 mm in height are formed under an

Table 4.1: Material properties

Property, symbol - units	PA12
Radius, R - [μm]	30
Material density, ρ - [kg/m^3]	1000
Green density, ρ_g - [kg/m^3]	450
Heat capacity, c_p - [J/kg K]	1200
Melting point, T_m - [$^\circ$C]	186

uni-axial pressure of 10 kPa inside a copper die. Subsequently, the resulting pellets were inserted into a NETZSCH 402C dilatometer that controls the temperature and pressure. Simultaneously, it measures the linear (axial) shrinkage over time via a thermocouple. Fig. 4.2 shows the overview of the experimental procedure.
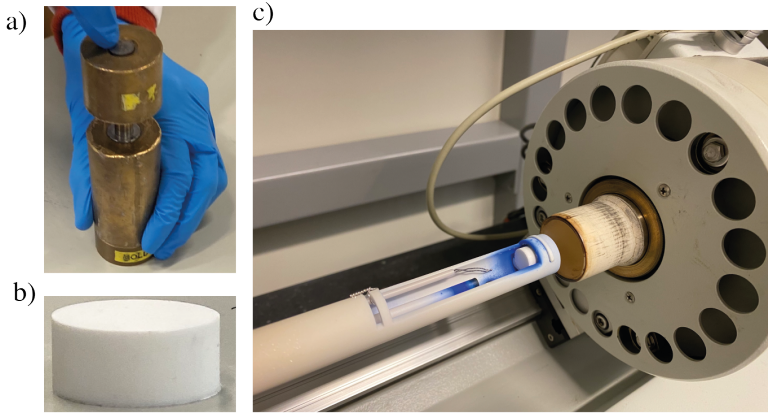
Figure 4.2: Experimental procedure to measure the densification of a PA12 pellet. a) PA12 powder is compacted inside a die to form the pellet. b) PA12 pellet to sinter. c) The pellet is in the furnace heating element.

In dilatometric experiments, the furnace heating element, where the pellet is held, is at room temperature (T_0) first. Then, the temperature of the system increases at a constant rate, reaching enough temperature to let the compacted pallet slowly start sintering. This activation temperature (T_a) is approximately 50% of the material's melting temperature (T_m). Subsequently, the temperature of the system reaches the process temperature (T_p), and it is maintained for a specific duration or holding time. Finally, the temperature of the system decreases at a constant rate to reach the initial room temperature. Fig. 4.3 provides a typical temperature profile for reference.

4.3. DEM CONTACT MODEL

DEM is utilized to model the densification process, including the visco-elastoplastic contact model developed by Luding *et al.* [15] and implemented in MercuryDPM [17]. This model is temperature and pressure-dependent, and its hysteretic behaviour is
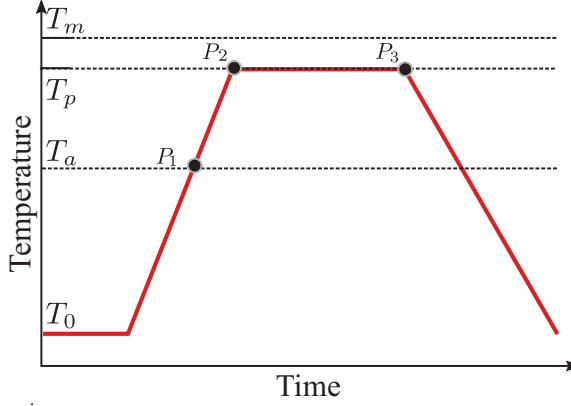
Figure 4.3: A typical temperature profile that can be used in a dilatometric experiment consists of several key temperatures: T_0 denotes the initial temperature, T_a represents the activation temperature at which the powder material begins to flow, T_p denotes the process temperature, and T_m indicates the melting temperature of the powder material. Additionally, there are three special points to be monitored during the experiment: P_1, P_2 and P_3.

monitored through the particle-particle overlap δ and normal force f_{ij}^n, illustrated in Fig. 4.4.
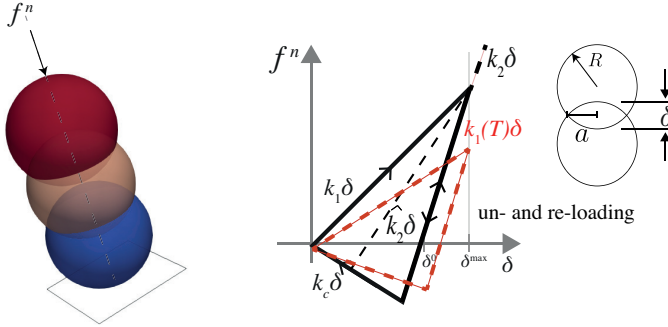
Figure 4.4: (Left) Three particles of radius R overlap due to a normal force f^n. (Right) visco-elasto-plastic contact law. The contact displacement is related to δ (overlap) and the normal contact force f^n. Right/left-pointing arrows are used to distinguish the forces obtained during the loading and unloading stages, respectively. The dotted line represents the loading stiffness k_1 reduction according to an incremented temperature T, k_2 is the unloading stiffness, k_c is the cohesive stiffness, and a represents the contact area radius.

The hysteretic behaviour of the normal contact force is described as:

$$f_{ij}^n = \left\{ \begin{array}{ll} \hat{k}_1(T)\delta_{ij} & \text{if } \delta_{ij} > \delta_{ij}^{\max} \\ \hat{k}_2(\delta_{ij} - \delta_{ij}^0) & \text{if } \delta_{ij}^{\min} < \delta_{ij} \leq \delta_{ij}^{\max} \\ -k_c\delta_{ij} & \text{if } 0 < \delta_{ij} \leq \delta_{ij}^{\min} \end{array} \right\} + \eta^n v_{ij}^n. \tag{4.1}$$

The computation of the repulsive visco-elasto-plastic forces f_{ij}^n during sintering follows the loading stiffness $\hat{k}_1$. It decreases according to the temperature, T, approaches the melting point of a material, and therefore, the material can deform significantly because the contact area becomes much larger at the particle level. We assume $\hat{k}_1$ as:

$$\hat{k}_1(T) = \frac{k_1}{2}\left[1 + \tanh\left(\frac{T_m - T}{T_{var}}\right)\right], \tag{4.2}$$

where T_{var} corresponds to the range in which the melting occurs. In the transition regime $T_m - T \approx T_{var}$, the particles are significantly softer than in the cold limit $T_m - T \gg T_{var}$. Note that $\delta^{max} = 2\phi_f R_{ij}$ is setting as the maximal plastic overlap, where $\phi_f = \sqrt[3]{2}$ and R_{ij} represents the effective particle radius. On the other hand, δ_{ij}^{max} is the maximum overlap of their pairs contact, which is a memory parameter. The illustration of $\hat{k}_1$ as a function of temperature is depicted in Fig. 4.5.
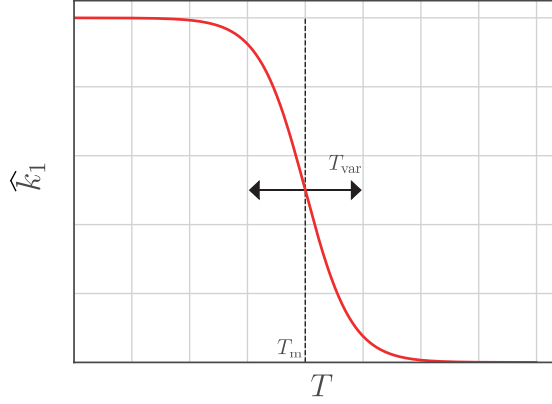
Figure 4.5: Schematic illustration of the stiffness $\hat{k}_1$ as a function of the temperature.

The un-loading and re-loading normal interactions, see Fig. 4.4 follows the slope of $\hat{k}_2$, which varies between $\hat{k}_1(T)$ and k_2 with plastic deformation at zero force δ_{ij}^0. Note that k_2 is not changed directly when T increases. For overlaps smaller than δ^{max}, the unloading stiffness is interpolated linearly between k_2 and $\hat{k}_1(T)$ as

$$\hat{k}_2 = \left\{\begin{array}{ll} \hat{k}_1(T) + (k_2 - \hat{k}_1(T))\frac{\delta_{ij}^{max}}{\phi_f R_{ij}} & \text{if } \delta_{ij}^{max} < \delta^{max} \\ k_2 & \text{if } \delta_{ij} \geq \delta^{max} \end{array}\right\}, \tag{4.3}$$

After the contact force becomes negative, for $\delta_{ij} < \delta_{ij}^0$, the model introduces cohesive forces using the cohesion stiffness k_c.

Furthermore, if particles are heated, in general, their density decreases. Thus, we assume that the particle radius changes in linear approximation as

$$R_i(T) = R_i(T_m)[1 + \delta a_T(T_m - T)], \tag{4.4}$$

with the relative change of the radius per unit temperature (thermal expansion) δa_T. This approximation can be used if the range of temperatures is relatively narrow and the changes per unit temperature are very small [15].

In the case of collisions of particles and large deformations, dissipation occurs due to the hysteretic nature of the force-law and by a viscous, see Eq. (4.1), dissipative, velocity-dependent force $\eta^n v_{ij}^n$, with η^n as viscous dissipation coefficient. This coefficient is related to the restitution coefficient e as $\eta^n = \sqrt{2mk_1}/(\sqrt{\pi} + \sqrt{\log e})\log e$, and therefore, this force-displacement model depends only on particle mass, not relative velocity [17]. This is a particular case assuming $k_1 = k_2$. The contribution of the normal forces act in the normal direction to the contact area, $\mathbf{n}_{ij}$.

Therefore, the total contact force during the collision of the particles may be given as:

$$\mathbf{f}_{ij} = (f_{ij}^n + f_{ij}^a)\mathbf{n}_{ij} + \mathbf{f}_{ij}^t, \tag{4.5}$$

The additional adhesive force $f_{ij}^a = k_1\delta_a$ is assumed constant in Eq. (4.5). For the tangential force calculation $\mathbf{f}_{ij}^t$ in the current implementation, see Eq. (4.5), the contributions of sliding, rolling and torsional friction are assumed temperature-independent for simplicity and defined similarly to the normal forces. For a detailed explanation, the reader is referred to the tangential force and torque models introduced in [20] and implemented in MercuryDPM [17]. Here, we summarize the model.

An elastic and dissipative lateral (sliding) force can be defined as:

$$\mathbf{f}_{ij}^{sl} = k^{sl}\delta_{ij}^{sl} + \gamma^{sl}\mathbf{v}_{ij}^{sl}, \tag{4.6}$$

where k^{sl} represents the sliding stiffness, δ_{ij}^{sl} is the tangential elastic displacement, γ^{sl} is the sliding dissipation, and $\mathbf{v}_{ij}^{sl}$ defines the lateral relative velocity. If the later force exceeds a certain level, the particle begins to slide. This is modelled by a Coulomb yield criterion, cutting off the elastic displacement when it exceeds a certain fraction μ^{sl}, the sliding friction coefficient, of the normal force.

$$\mid \mathbf{f}_{ij}^{sl} \mid \le \mu^{sl} f_{ij}^n. \tag{4.7}$$

Similarly, rolling and torsion torques are modelled to resist angular motion such as:

$$\tau_{ij}^{ro} = a_{ij}^{eff}\mathbf{n}_{ij}(k^{ro}\delta_{ij}^{ro} + \gamma^{ro}\mathbf{v}_{ij}^{ro})\mathbf{n}_{ij}, \tag{4.8}$$

$$\tau_{ij}^{to} = a_{ij}^{eff}\mathbf{n}_{ij} \times (k^{to}\delta_{ij}^{to} + \gamma^{to}\mathbf{v}_{ij}^{to}), \tag{4.9}$$

with $a_{ij}^{eff} = \frac{|\mathbf{r}_{ij}||\mathbf{r}_{ij}|}{|\mathbf{r}_{ij}|+|\mathbf{r}_{ij}|}$ the effective length of the branch vectors. k^{ro} and γ^{ro} represent the rotational stiffness and dissipation, respectively. k^{to} and γ^{to} represent the torsional

stiffness and dissipation, respectively. If the torques exceed a certain fraction of the normal contact force, the particle begins to roll and torque. Thus, the elastic displacement is cut off to satisfy

$$| \tau^{to} | \leq \mu^{to} \mathsf{a}_{ij}^{eff} f_{ij}^n, \tag{4.10}$$

$$| \tau^{ro} | \leq \mu^{ro} \mathsf{a}_{ij}^{eff} f_{ij}^n, \tag{4.11}$$

where μ^{to} and μ^{ro} are the torsional and rolling friction coefficients.

4.3.1. CONTACT EVOLUTION FOR TEMPERATURE-DEPENDENT SINTERING

By defining the evolution of the relative contact radius $f(\delta) = a_{ij}/R_{ij}$ (or neck growth), it is possible to include the various stages of visco-elastic sintering [21] into the DEM approach, by relating the particle-particle overlap δ_{ij} to the computation of the normal force f_{ij}^n, see Eq.(4.1). Our previous investigation has discussed mathematically a_{ij}/R_{ij} for sintering, and therefore, the reader is referred to [16] for more detail. Fig. 4.6 illustrates the definition of the sintering regime map.
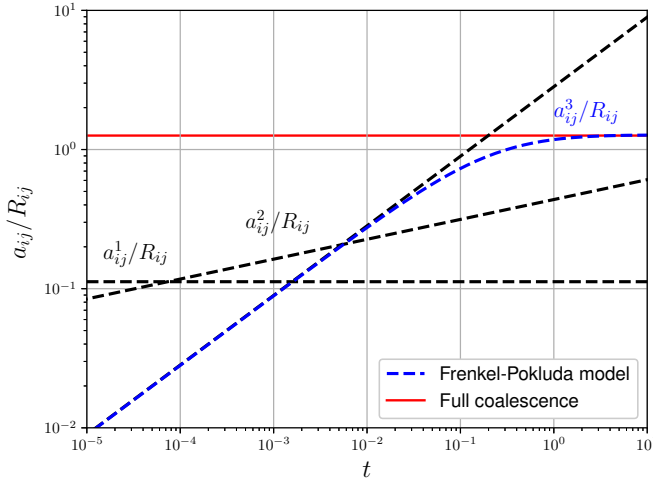
Figure 4.6: Sintering regime map with three mechanisms for flow simulation: (1) Adhesive contact, (2) Adhesive inter-surface forces, and (3) Surface tension regimes.

The non-dimensional neck radius a_{ij}^1/R_{ij} was derived by Johnson, Kendall, and Roberts [22] at very short times t_0, for the equilibrium deformation of two elastic bodies under the influence of surface tension may be described as:

$$\frac{a_{ij}^1}{R_{ij}} = \Big(\frac{9\pi(1-\nu^2)\gamma}{ER_{ij}} \Big)^{1/3}, \tag{4.12}$$

where γ is surface tension, ν is Poisson's ratio, and E is Young's modulus.

For intermediate times in the interval $t_0 < t < t_{vis}$, the growth of contact radius a_{ij}^2 is predicted to be:

$$\frac{a_{ij}^2}{R_{ij}} = \left(\frac{63\pi^3}{16}\right)^{1/7}\left(\frac{\delta_c}{R_{ij}}\right)^{2/7}\left(\frac{2C_1(T)\gamma t}{R_{ij}}\right)^{1/7}. \tag{4.13}$$

The separation distance δ_c is specified to add the contribution of adhesion to the contact model, defined as the range of the adhesive force acting between two surfaces. The time duration is represented by t. The fluidity of the material is characterized by the rheological temperature and contact parameter $C_1(T)$, which describes the flowability of the matter under deformation. We assume this coefficient similarly as $\hat{k}_1(T)$ (see Eq. (4.2)), as:

$$C_1(T) = C_1\left[1 - \tanh\left(\frac{T_m - T}{T_{var}}\right)\right]. \tag{4.14}$$

The third stage computes the evolution of the contact area according to the model proposed by Pokluda [23], which describes the sintering process balancing the work of surface tension and viscous dissipation for the maximum particle-particle overlapping. It is expressed as:

$$\frac{a_{ij}^3}{R_{ij}} = \sin(\theta)\left[\frac{4}{(1+\cos(\theta))^2(2-\cos(\theta))}\right]^{1/3}, \tag{4.15}$$

where

$$\theta = \left(\frac{8\gamma C_1(T)t}{R_{ij}}\right)^{1/2}. \tag{4.16}$$

To include $a_{ij}^1, a_{ij}^2,$ and, a_{ij}^3 in the contact description, Eq.(4.1), the rate of the plastic overlap $\dot{\delta}_{ij}^0$ is computed . Knowing that the overlap between the particles nearly equals the plastic overlap, $\delta_{ij} \approx \delta_{ij}^0$ for stiff particles ($k_1 \gg (f_{ij}^n + f_{ij}^a)/R_{ij}$), the contact relative radius may be approximated as $a_{ij}/R_{ij} \approx \sqrt{\delta_{ij}/R_{ij}}$. Therefore, the interpenetration among the particles is controlled by setting the growth rate $\dot{\delta}_{ij}^0$ according to Eq. (4.12), Eq. (4.13), Eq. (4.15).

4.4. RESULTS AND DISCUSSION

This section presents the computational analysis of densification. First, the calibration step is developed: insert particles into a cylindrical domain to generate the representative cylindrical pellet, homogenize particles on the top surface, and increase the system's temperature to induce sintering, measuring the linear (axial) shrinkage of the pellet and calibrating the model parameters via GrainLearning. Second, the influence of process parameters on the evolution of the bulk density of the calibrated pellet. The contact parameters are summarized in Table 4.2.

Table 4.2: Particle pair contact properties.

Property, symbol	units	Value
Loading stiffness, k_1	[N/m]	$\beta E R$
Unloading stiffness, k_2	[N/m]	$10k_1$
Cohesion stiffness, k_c	[N/m]	k_1
Gravity, g	[m/s^2]	9.81
Sliding stiffness, k^{sl}	[N/m]	$0.2k_1$
Rolling stiffness, k^{ro}	[N/m]	$0.1k_1$
Torsional stiffness, k^{to}	[N/m]	$0.1k_1$
Sliding friction, μ^{sl}	[-]	0.05
Rolling friction, μ^{ro}	[-]	$0.1\mu^{sl}$
Torsional friction, μ^{to}	[-]	$0.1\mu^{sl}$
Dissipation, η_o	[mg/s]	1.0
Sliding dissipation, γ_o^{sl}	[mg/s]	$0.2\gamma_o$
Rolling dissipation, γ_o^{ro}	[mg/s]	$0.05\gamma_o$
Torsional dissipation, γ_o^{to}	[mg/s]	$0.05\gamma_o$
Range of melting, T_{var}	[°C]	$0.1\,T_m$
Adhesive distance, δ_a,	[m]	0.001
Relative change of particle radius, δa_T	[1/K]	0.0001

The magnitude of stiffness k_1 is chosen based on the micro-macro relation $k_1 = \beta E R$ [10], where $\beta = 0.1$ and $E = 1.0$ GPa are used in our work, with $R = R_{ij}$.

4.4.1. PELLET PREPARATION

The particles are contained within a cylindrical domain (W) that has a diameter of 1.16 mm and a height of 1.9 mm. It is assumed that sintering only occurs among the particles and any thermal effects of the boundary are neglected. The properties of the container are summarized in Table 4.3.

Table 4.3: Particle-wall contact properties.

Property, symbol - units	Value
Loading stiffness, k_1^W - [N/m]	$100k_1$
Unloading stiffness, k_2^W - [N/m]	$200k_1$
Cohesion stiffness, k_c^W - [N/m]	0.0
Penetration depth, ϕ_f^W - [-]	0.001
Friction, μ^W [-]	0.0
Dissipation, η_o^W [mg/s]	0.0

The particle size distribution is generated and the insertion process from the upper surface of the system is started using a cuboidal insertion boundary procedure in MercuryDPM. This procedure inserts particles into a rectangular region of the domain by defining the insertion rate, particle size distribution, and velocity distribution.

Fig. 4.7 illustrates some steps of the procedure using PA12 properties (Table 4.1) and a mono-disperse size distribution.
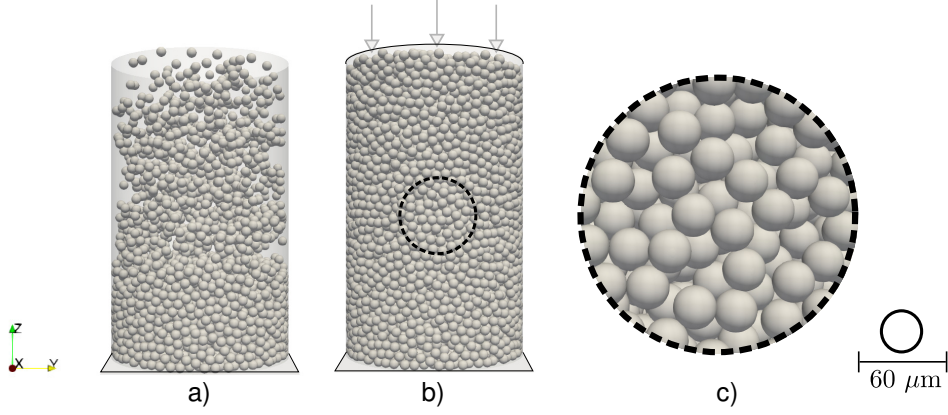
Figure 4.7: a) Particles are inserted in a cylindrical domain. b) Pressure is applied onto the top surface to compact the pellet. c) A close view of the system.

The insertion process begins with 30 μm particles falling from the upper part of the system due to gravity ($g = 9.81$ m/s^2). The accumulation process continues until the system reaches its maximum height at 1.9 mm height, resulting in a configuration with a realistic distribution of particles and low porosity. A total of 10,572 particles are inserted into the domain. To ensure a homogenous distribution of particles and a level surface, a compacting pressure of 1.0 kPa is applied to the particles located on the top surface boundary; similar to the dilatometric experiment. The objective is to generate pellets that represent a green condition before the sintering process and accurately capture the correct volume, as the pellets from the experiment in Fig. 4.2. To determine the volume fraction (ϕ_{VF}) of the pellets, we utilize the spatial coarse-graining approach developed by Weinhart *et al.* [24]. The volume fraction is defined as follows:

$$\phi_{VF}(\mathbf{r}, t) = \frac{\rho(\mathbf{r}, t)}{\rho_p} = \sum_{i=1}^{N} \mathcal{V} \mathcal{W}(\mathbf{r} - \mathbf{r}_i(t)), \tag{4.17}$$

where $\mathcal{V} = \frac{\pi}{6} R^3$ is the particle volume. A Lucy function is used for coarse-graining, which for three spatial dimensions is

$$\mathcal{W}(\mathbf{r}) = \frac{105}{16\pi c^3} \left(-3(r/c)^4 + 8(r/c)^3 - 6(r/c)^2 + 1 \right), \text{ if } r := |\mathbf{r}| < c, \text{ 0 else,} \tag{4.18}$$

with c the range and $w = c/2$ the half-width, or standard deviation.

Thus, a plane can be defined through the axis of the cylinder (at $y = 0.58$ mm), See Fig. 4.7 and the macroscopic field of volume fraction is extracted at the last time step of the compaction stage, with a coarse-graining width $w = 3.0 \times 10^{-4}$ m. The results are presented in Fig. 4.8.
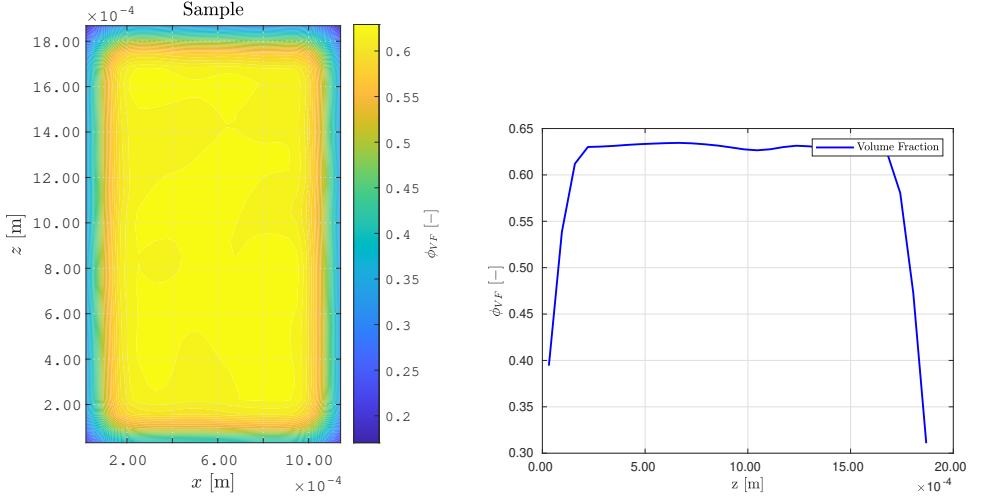
Figure 4.8: Pellet at the last time step. a) Volume fraction field. b) Volume fraction profile $\phi_{VF}(z)$ defined through the axis of the cylinder (at $y = 0.58$ mm).

The volume fraction is an essential parameter in DEM simulations, as it provides insights into the macroscopic properties of the system, such as its ability to withstand mechanical loads, flow properties, and thermal properties. As shown in Fig. 4.8 a), the numerical pellet is a good representative of the PA12 pellet, with a homogenous distribution of particles occupying around $\phi_{VF} = 0.63$ of the domain. For simplicity, we conducted all simulations using a mono-disperse size distribution in the system. Our findings indicate that aspect ratios with a maximum-to-minimum ratio (R_{max}/R_{min}) below 4.0 exhibited negligible effects on the further sintering process. Note that polydispersity affects the packing density of particles, and therefore, may impact the degree of sintering and the final properties of the material. Polydispersity in a pellet can result in larger pores, lower packing density, lower mechanical strength, and less efficient thermal conductivity. Therefore, future studies should be conducted to investigate the effects of polydispersity on densification.

4.4.2. CALIBRATION OF THE SINTERING MODEL

To calibrate the contact rheology of PA12, GrainLearning [18] is used, coupled with MercuryDPM [17]. The open package determines the best probabilistic distribution of experimental and model parameters, allowing for more accurate predictive simulations. From the dilatometric experiments (see Sec. 4.2), the linear (axial) shrinkage and temperature evolution are the observations to track, while the model parameters to calibrate are fluidity $C_1(T)$ and surface tension γ. Firstly, we define the possible space for the variables, as listed in Table 4.4.

We define the calibration procedure with five iterations, each containing fifty samples, equal weight of 1.0 for all samples. At the first iteration, the normalized covariance parameter is set to 0.7, ensuring an effective sample size greater than 20%. The

Table 4.4: Upper and lower limits of the parameters to generate homogeneous quasi-random numbers for the first iteration.

Property	$C_1 [\mathrm{Pa}^{-1}\mathrm{s}^{-1}]$	γ [N/m]
Θ_{min}	0.001	0.020
Θ_{max}	0.011	0.053

convergence criterion is based on the agreement of the posterior expectations after each single iteration of Bayesian filtering. After the third iteration, the posterior expectation of each micro-parameter converges. This means that they have stabilized, and further iterations are not significantly changing these expectations. Therefore, the filtering process may stop at this point because the desired level of stability or accuracy has been achieved. Fig. 4.9 depicts the re-sampling process.
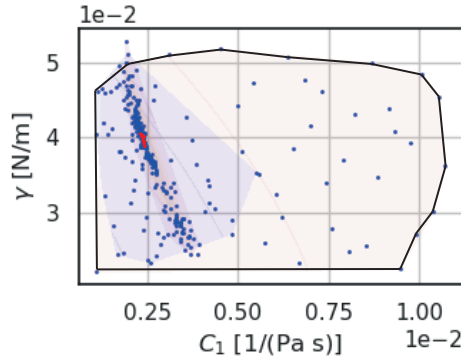
Figure 4.9: Calibration of C_1 and γ for DEM simulations. Layers indicate the space of the parametric sample at every iteration, from the first layer of the initial parametric space represented by a line, blue dots represent the sample points, which progressively converge to a narrowed area. Red dots represent the best estimation of the parameters at the last iteration $i = 5$.

The illustration of the re-sampling process presented in Fig. 4.9 depicts the posterior modes localized progressively after each iteration. Table 4.5 summarizes the results after the completion of the calibration procedure.

Table 4.5: Calibrated model parameters

symbol - units	Value
C_1 - $[\mathrm{Pa}^{-1}\mathrm{s}^{-1}]$	$0.00240 \pm 1.0\%$
γ - [N/m]	$0.0393 \pm 1.0\%$

High precision is obtained, with only 1.0 ~ 2.0% range of error. In addition, γ is within the expected range according to the literature [25]. Thereby, our DEM model is calibrated based on macroscopic observations from dilatometric experiments.

Fig. 4.10 illustrates the temperature profile of the process, with a heating rate of 1 °C/min from an initial temperature of $T_0 = 20$ °C to the target temperature

$T_p = 185\ ^\circ$C. The point at which the density of the pellet starts to change is denoted as P_1, while P_2 indicates the point at which the maximum temperature of the process is reached. The holding time (from P_2 to P_3) is set to 60 min, however, we considered only the data until 15 min after reaching the process temperature T_p, due to technical issues with the dilatometers.
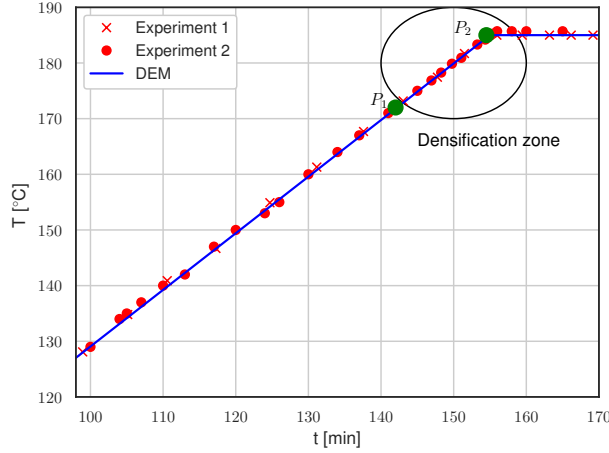
Figure 4.10: Temperature evolution during the dilatometric experiment. The shapes represent the experimental measurements contrasted to the calibrated DEM simulation denoted by the solid line.

The densification zone of the pellet is above P_1 in Fig. 4.10. This zone is marked by a circle and corresponds to the window of analysis for simulations.

The density evolution of the pellet is visualized in Fig. 4.11, where ΔL represents the relative reduction in length, linear (axial) shrinkage with respect to the initial length L_0, measured at the initial configuration.
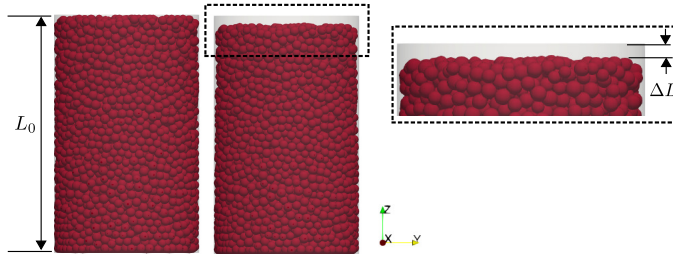
Figure 4.11: Densification of a PA12 pellet with initial length L_0: (left) before sintering, (right) after sintering. ΔL represents the linear (axial) shrinkage. The zoom-in window highlights the densification.

The linear shrinkage of the pellet has been monitored during the simulation, assuming that the temperature within the particles is homogeneous. The results in comparison

with the two experimental data sets are presented in Fig. 4.12.
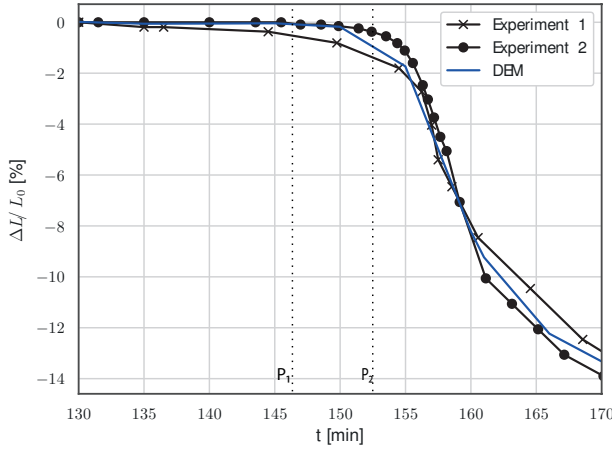
Figure 4.12: Experimental and numerical results of the relative Linear (axial) shrinkage of the PA12 pellet.

As shown in Fig. 4.12, the proposed DEM model captures the reduction in length, linear (axial) shrinkage, of the pellet. Specifically, our simulation predicts an average shrinkage of 13.5 %. Note that this reduction is inside the circular window of analysis. After this window, the densification rate is expected to be constant, allowing the particles to sinter further until reaching the end of the holding period at P_3, see Fig. 4.3. Interestingly, pellet swelling can occur during the holding stage (from P_2 to P_3), especially for metallic or ceramic powders if the process temperature T_p exceeds the melting temperature T_m. Surface porosity within the aforementioned powders can be sites for trapped gases, which at high sintering temperatures will generate internal pressure, leading to swelling [26]. After the holding period, the temperature of the process starts decreasing, lowering the sintering rate until reaching the initial temperature of the process T_0. Future studies based on further experimental data can focus on the end of the holding period (P_3), and the modelling of the contraction during the cooling stage.

4.4.3. Effect of process temperature

To study the effect of the process temperature T_p on the densification of the PA12 pellets, the calibrated DEM model, described in Sec. 4.4.2, is first tested with different temperature profiles, as presented in Fig. 4.13.

Four temperature profiles have been defined by setting the maximum temperature $T_{p,max}$ from 185 °C to 176 °C. The end of the holding time (P_3) is constant for all profiles, $t_h = 162$ min. As the maximum temperature of the process $T_{p,max}$ decreases, the cooling rate decreases slowly in order to maintain the end of the cooling period constant at $t = 164$ min. The total process time is constant for all simulations,
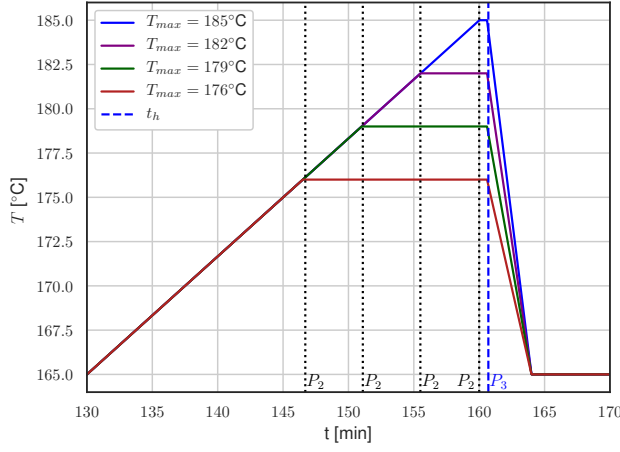
Figure 4.13: Solid lines represent the temperature profiles of the process, and the dashed lines are the start of each holding period P_2, with duration t_h at P_3.

.

t_f = 170 min. By monitoring the relative and linear (axial) shrinkage $\Delta L/L_0$ of the pellet, it is possible to calculate the relative density ρ_{rel} as,

$$\rho_{rel} = \frac{\rho}{\rho_g} = \frac{1}{1 - \frac{\Delta L}{L_0} + \delta_a (T - T_0)^3}, \tag{4.19}$$

where ρ_g represents the green or apparent density of the pellet before sintering (see Table 4.1), δ_a is the thermal expansion (see Table 4.2), T_0 is the initial temperature of the process, $T_0 = 165\,°C$. The results are depicted in Fig. 4.14.

The relative density of the pellet increases as the process temperature approaches the melting point, $T_m = 186\,°C$. It is described in our DEM model by fluidity $C_1(T)$. Fig. 4.14 shows that an increment of 3 °C in the maximum process temperature, $T_{p,max}$, approximately let to $\rho_{rel} = 2\%$ ahead of the previous achieved relative density during the same process time. Furthermore, if T_{max} decreases, the holding period, from P_2 to P_3, increases, which leads to a lower densification rate. It suggests that a higher densification of a PA12 pellet is reached for temperatures close to the melting point, and as a consequence, a lower process time is required.

The influence of the process temperature on the relative density of the pellet is visualized in Fig. 4.15.

As visualised in Fig. 4.15, higher temperatures are beneficial from the process view, since they lead to higher densification, and therefore, stronger bonds among the particles. However, temperatures close to the melting point and extended *holding times* (from P_2 to P_3) can cause thermal decomposition and distortion of the pellet. This effect is analysed in the next section.
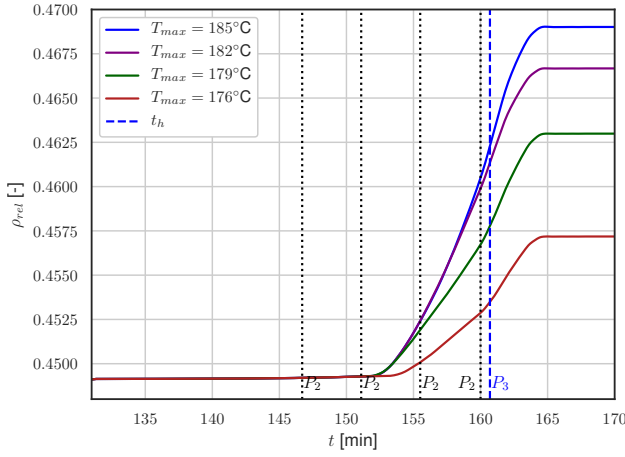
Figure 4.14: Relative density of the PA12 pellet according to different process target temperatures.
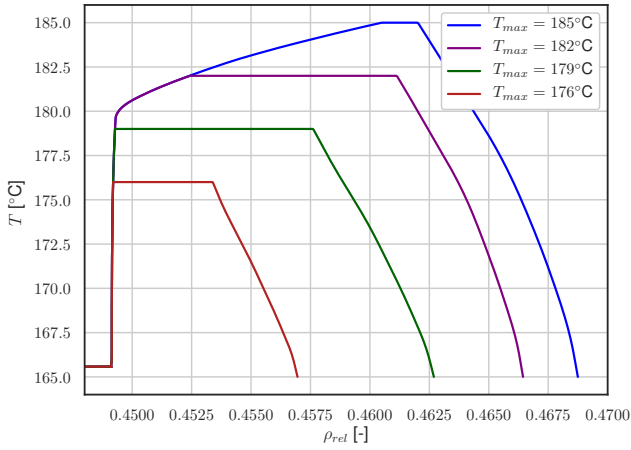
Figure 4.15: Influence of temperature on the relative density (ρ_{rel}) of a PA12 pellet.

4.4.4. Effect of holding time

The holding time, t_h, refers to the period when the pellet is maintained at the process temperature T_p for a specific duration (from P_2 to P_3, see Fig. 4.3 for reference). Thus, further densification is achieved and uniformity within the microstructure. Four different holding times are set to the process temperature, $T_p = 185\,°\text{C}$ in order to assess the effect on the PA12 calibrated pellet, see Fig. 4.16.

The cooling period finishes at $t = 164$ min for all profiles, the moment at which it reaches
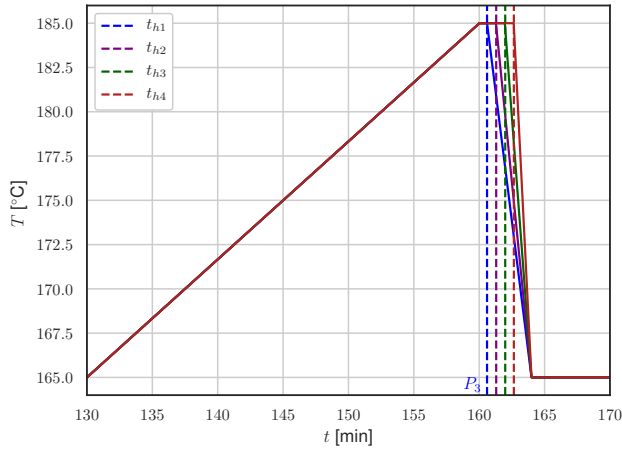
Figure 4.16: Solid lines represent the temperature profiles of the process, and dashed lines are the end of the holding periods, P_3.

the initial temperature $T_0 = 165\ ^\circ\text{C}$ of the process, and then the temperature is constant until the end of the process time at $t = 170$ min. Note that extended holding times are out of the scope of the present investigation since more experimental data are required to describe the DEM model. The results of relative density over time are presented in Fig. 4.17.
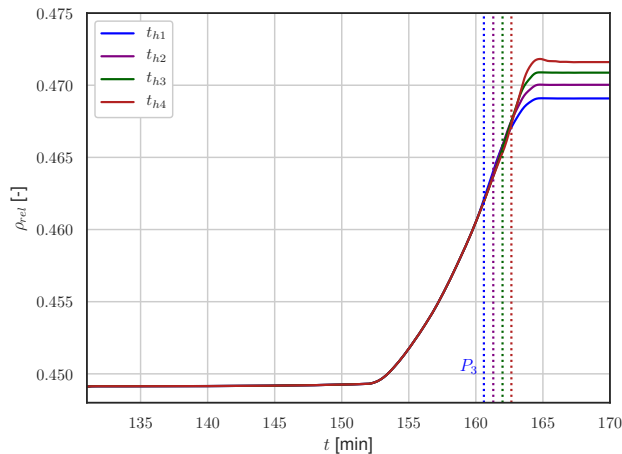
Figure 4.17: Relative density of the PA12 pellet according to different holding times t_h.

Increasing the holding time, t_h, during the densification of the pellet results in higher

densification. In general, if the pellet is held for periods longer than 1 min (from P_2 to P_3), a linear increment of 1% in relative density is achieved. It is observed that the effect of the holding time on densification is more significant during the cooling period, after P_3. We suggest that for small increments of holding times and for temperatures close to the melting point, higher densification may be achieved only in the cooling period of the pellet, as a consequence of a faster cooling rate.

The influence of the holding time t_h on the relative density of the pellet is visualized in Fig. 4.18.
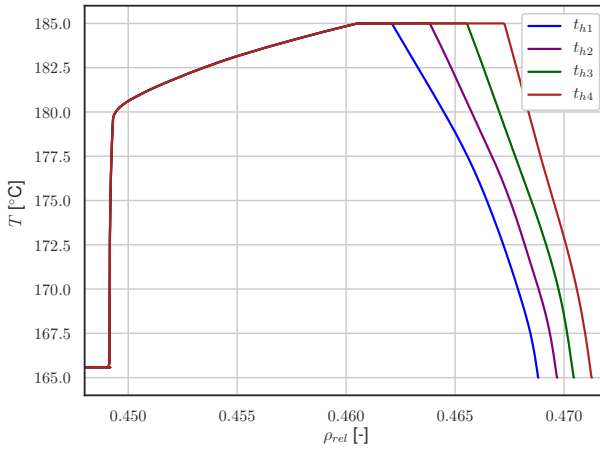
Figure 4.18: Influence of holding time t_h on the relative density (ρ_{rel}) of a PA12 pellet.

Experimentally, extended holding times, t_h, allow the particles to rearrange, create stronger bonds and assist densification. It results in higher compacted powder pellets, which in turn may reduce the process temperature. As visualised in Fig. 4.18, small increments of holding times do not significantly assist the densification of the pellet. In contrast, if the holding time is excessive, the *process time* requires to be prolonged, which may lead to grain growth and coarsening of the micro-structure, impacting negatively the mechanical properties of the pellet. The next section discusses the effect of process time on the densification of the PA12 pellet.

4.4.5. EFFECT OF PROCESS TIME

In densification, process time t_f refers to the duration for which a pellet is heated, held (from $P2$ to $P3$) and cooled. Four process times are set to the calibrated PA12 pellet for a process temperature $T_p = 185°C$, see Fig. 4.19.

The process temperature t_f is varied with intervals of 6 min longer, as depicted in Fig. 4.19. The cooling rate for the simulations is maintained constant, extending the holding period similarly; 6 min longer, from P_2 to P_3. The effect of process time on the
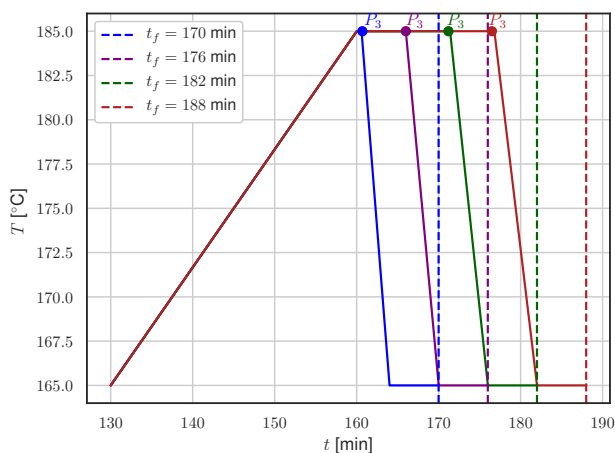
Figure 4.19: Solid lines represent the temperature profiles of the process, and dashed lines are the end of the process time t_f. P_3 represents the end of the holding period.

relative density is visualized in Fig. 4.20.
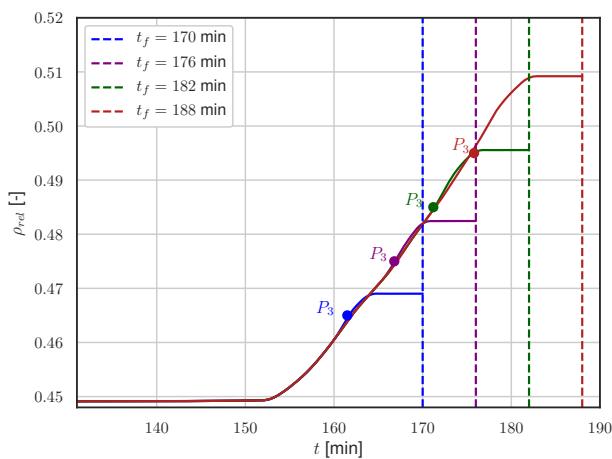
Figure 4.20: Relative density of the PA12 pellet according to different process times t_f. Dashed lines represent the end of the process time. P_3 indicates the end of the holding period.

As shown in Fig. 4.20, if the process time t_f increases by 6 min, the densification of the pellet also increases, approximately 10%. The transition between the holding period (P_3) to the end of the cooling period leads to a parabolic behaviour in the prediction of densification, which expands as long as t_f increases due to the contraction of the

sample.

The influence of the process time t_f on the relative density of the pellet is visualized in Fig. 4.21.
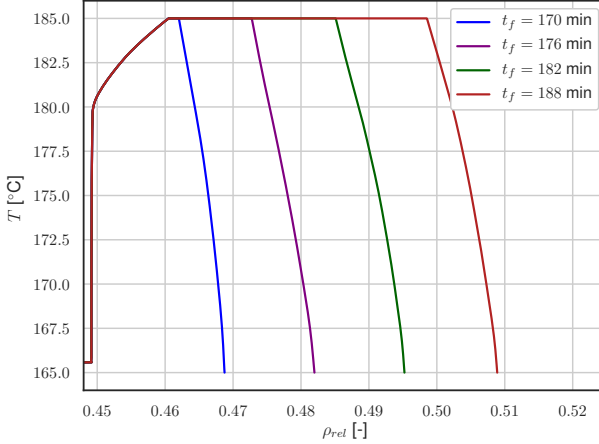
Figure 4.21: Influence of process time t_f on the relative density (ρ_{rel}) of a PA12 pellet.

In general, the process time is the most relevant process parameter in our simulations to achieve higher densification of the PA12 pellet, while keeping the temperature close to the melting point, see Fig. 4.21. However, the process time during densification must be carefully controlled to avoid excessive sintering among the particles and the thermal degradation of pellets. To decrease the process time during densification, an external *pressure* can assist the process and minimise the effect of poor sintering. The influence of pressure during densification is discussed in the following section.

4.4.6. PRESSURE-ASSISTED SINTERING

An external pressure during densification can significantly improve the mechanical properties of a pellet by increasing the level of particle packing, reducing the void space between particles, and decreasing the process time t_f. Three process temperature profiles under the influence of constant pressure are designed and visualized in Fig. 4.22.

The temperature profiles are set to the calibrated PA12 pellet, ranging from a maximum process temperature $T_{max} = 185°$C to $T_{max} = 179°$C. The holding period (from P_2 to P_3) increases as the maximum temperature of the process decreases since the end of the cooling period is maintained constant for all simulations, at $t = 182$ min. The total process time is set to $t_f = 188$ min. Additionally, a pressure P = 1000 Pa is applied to the particles located at the top surface while subjected to the temperature. The results of relative density are presented in Fig. 4.23.

4
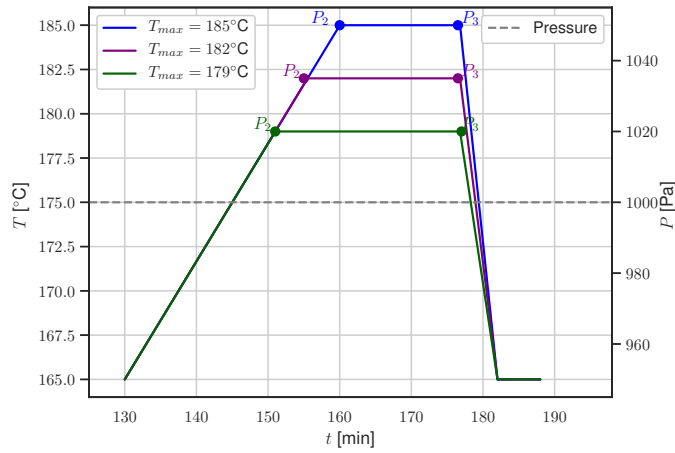
Figure 4.22: Solid lines represent the temperature profiles of the process, and the dashed line is the applied pressure. P_2 and P_3 mark the interval of the holding period.
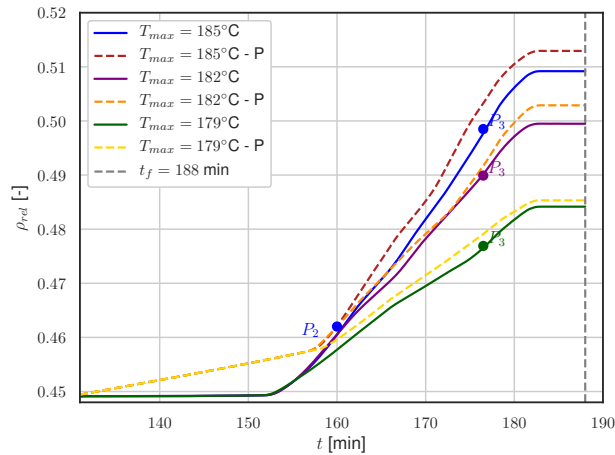
Figure 4.23: Relative density of the PA12 pellet according to different process temperatures, and applied pressure $P = 1000$ Pa.

The results demonstrate that an external pressure during the process assists the densification of the PA12 pellet, especially when the temperature of the process is close to the melting point $T_m \sim 186°C$. Furthermore, the simulation reveals that the process time may be reduced for applied pressures, for example, $P > 1000$ Pa.

The influence of the pressure on the relative density of the pellet is visualized in Fig. 4.24.
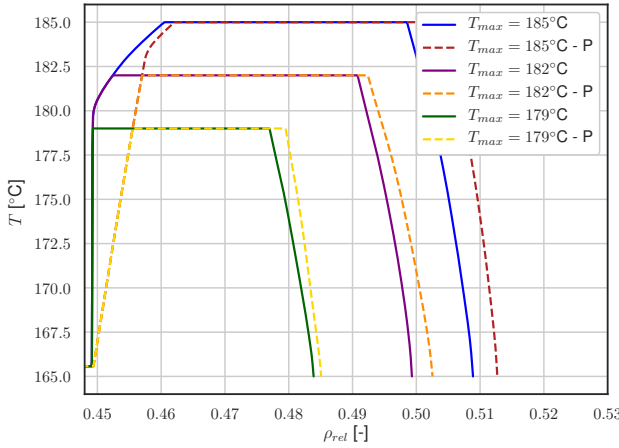
Figure 4.24: Influence of pressure P on the relative density (ρ_{rel}) of a PA12 pellet.

It is evidenced that either the process time t_f or the external pressure P are the most significant process parameters during the densification analysis of the PA12 pellet. Applying external pressure may lead to a denser and stronger pellet with improved strength and hardness. Furthermore, it can also prevent dilation (swelling) during the heating and holding periods, as a result of entrapped air. However, excessive pressure may lead to deformation or even fracture of the pellet.

4.5. CONCLUSIONS AND OUTLOOK

The understanding of densification of visco-elastic powders while sintering can provide a tool to optimize materials for industrial applications. This investigation provided a computational approach to analyse this process based on the discrete element method (DEM). First, a temperature and pressure-dependent contact model is implemented in MercuryDPM, along with a novel rheological contact model to describe the rate of sintering. Then, dilatometric experimental data were collected on PA12 compacted pellets in order to calibrate the simulations. The calibration process included Bayesian filtering to infer the range of two model parameters, fluidity and surface tension, based on temperature evolution and linear (axial) shrinkage of the pellet during the experiment. The simulation results showed that the proposed model predicted the linear shrinkage of the PA12 pellets with good agreement. Subsequently, different process parameters were tested on the calibrated model such as the maximum process temperature, holding time, process time, and pressure. Despite the analyses being developed within a short time window, close to the material's melting point, the simulations revealed that the process time and pressure are the process parameters more relevant to assist densification.

Future studies could include the crystallization effect in the contact model as well as

the analysis of densification during the cooling period of visco-elastic pellets; based on experimental data. Overall, the combination of experimental data and DEM simulations offers a powerful approach to understanding and optimizing the densification of powder materials.

4.6. ACKNOWLEDGMENTS

REFERENCES

[1] S. Krishnan, A. Haseeb, and M. R. Johan, *Preparation and low-temperature sintering of Cu nanoparticles for high-power devices,* IEEE Transactions on Components, Packaging and Manufacturing Technology **2**, 587 (2012).

[2] H. Hao, Y. Wang, H. R. Jafari Nodooshan, Y. Zhang, S. Ye, Y. Lv, and P. Yu, *The effects of sintering temperature and addition of TiH2 on the sintering process of Cu,* Materials **12**, 2594 (2019).

[3] X. Xu, P. Lu, and R. M. German, *Densification and strength evolution in solid-state sintering part II strength model,* Journal of materials science **37**, 117 (2002).

[4] C. Manière, S. Chan, G. Lee, J. McKittrick, and E. A. Olevsky, *Sintering dilatometry based grain growth assessment,* Results in Physics **10**, 91 (2018).

[5] J.-H. Ji, J. Kim, and J.-H. Koh, *Improved dielectric and piezoelectric properties of K/Na excessed (Na, K) NbO3 lead-free ceramics by the two step sintering process,* Journal of Alloys and Compounds **698**, 938 (2017).

[6] F. Wang, S. You, D. Jiang, and F. Ning, *Study on sintering mechanism for extrusion-based additive manufacturing of stainless steel through molecular dynamics simulation,* Additive Manufacturing **58**, 102991 (2022).

[7] S.-J. L. Kang, *Sintering: densification, grain growth and microstructure* (Elsevier, 2004).

[8] R. Guo, M. Wang, L. Ming, S. Cheng, and K. Ning, *Research on effect of particle size and sintering parameters on porous transducer,* in *2018 IEEE International Conference on Manipulation, Manufacturing and Measurement on the Nanoscale (3M-NANO)* (IEEE, 2018) pp. 37–41.

[9] S. Nosewicz, J. Rojek, M. Chmielewski, and K. Pietrzak, *Discrete element modeling and experimental investigation of hot pressing of intermetallic NiAl powder,* Advanced Powder Technology **28**, 1745 (2017).

[10] S. Nosewicz, J. Rojek, M. Chmielewski, K. Pietrzak, and D. Lumelskyj, *Application of the Hertz formulation in the discrete element model of pressure-assisted sintering,* Granular Matter **19**, 1 (2017).

[11] V. Ivannikov, F. Thomsen, T. Ebel, and R. Willumeit-Römer, *Coupling the discrete element method and solid state diffusion equations for modeling of metallic powders sintering,* Computational Particle Mechanics , 1 (2022).

[12] V. Iacobellis, A. Radhi, and K. Behdinan, *Discrete element model for ZrB2-SiC ceramic composite sintering,* Composite Structures **229**, 111373 (2019).

[13] S. Martin, S. Navarro, H. Palancher, A. Bonnin, J. Léchelle, M. Guessasma, J. Fortin, and K. Saleh, *Validation of DEM modeling of sintering using an in situ X-ray microtomography analysis of the sintering of NaCl powder,* Computational Particle Mechanics **3**, 525 (2016).

[14] T. Matsuda, *Development of a DEM taking account of neck increments caused by surface diffusion for sintering and application to analysis of the initial stage of sintering,* Computational Materials Science **196**, 110525 (2021).

[15] S. Luding, K. Manetsberger, and J. Müllers, *A discrete model for long time sintering,* Journal of the Mechanics and Physics of Solids **53**, 455 (2005).

[16] J. Alvarez, H. Snijder, T. Vaneker, H. Cheng, A. Thornton, S. Luding, and T. Weinhart, *Visco-elastic sintering kinetics in virgin and aged polymer powders,* Powder technology **397**, 117000 (2022).

[17] T. Weinhart, L. Orefice, M. Post, M. P. van Schrojenstein Lantman, I. F. Denissen, D. R. Tunuguntla, J. M. Tsang, H. Cheng, M. Y. Shaheen, H. Shi, P. Rapino, E. Grannonio, N. Losacco, J. Barbosa, L. Jing, J. E. Alvarez Naranjo, S. Roy, W. K. den Otter, and A. R. Thornton, *Fast, flexible particle simulations — An introduction to MercuryDPM,* Computer Physics Communications **249**, 107129 (2020).

[18] H. Cheng, T. Shuku, K. Thoeni, P. Tempone, S. Luding, and V. Magnanimo, *An iterative Bayesian filtering framework for fast and automated calibration of DEM models,* Computer Methods in Applied Mechanics and Engineering **350**, 268 (2019).

[19] P. Hartmann, H. Cheng, and K. Thoeni, *Performance study of iterative Bayesian filtering to develop an efficient calibration framework for DEM,* Computers and Geotechnics **141**, 104491 (2022).

[20] S. Luding, *Cohesive, frictional powders: Contact models for tension,* Granular Matter **10**, 235 (2008).

[21] Y. Y. Lin, C. Y. Hui, and A. Jagota, *The role of viscoelastic adhesive contact in the sintering of polymeric particles,* Journal of Colloid and Interface Science **237**, 267 (2001).

[22] K. Johnson, K. Kendall, and A. Roberts, *Surface energy and the contact of elastic solids,* Proceedings of the Royal Society of London. A. Mathematical and Physical Sciences **324**, 301 (1971).

[23] O. Pokluda, C. T. Bellehumeur, and J. Vlachopoulos, *Modification of Frenkel's model for sintering,* AIChE Journal **43**, 3253 (1997).

[24] T. Weinhart, A. R. Thornton, S. Luding, and O. Bokhove, *From discrete particles to continuum fields near a boundary,* Granular Matter **14**, 289 (2012).

[25] P. Hejmady, L. C. van Breemen, D. Hermida-Merino, P. D. Anderson, and R. Cardinaels, *Laser sintering of PA12 particles studied by in-situ optical, thermal and X-ray characterization,* Additive Manufacturing **52**, 102624 (2022).

[26] E. Thian, N. Loh, K. Khor, and S. Tor, *Dilation of Ti-6Al-4V/HA composite tensile parts,* Advanced Composites Letters **11** (2002), https://doi.org/10.1177/096369350201100204.

5

A THERMO-MECHANICALLY COUPLED MULTI-SCALE MODEL OF GRANULAR MEDIA

This study presents a thermo-mechanically coupled multi-scale approach for bridging the physics between discrete and continuum descriptions of heated granular media. The scale bridging between micro (discrete) and macro (continuum) models is achieved within an overlapping volume using the discrete element method (DEM) to represent individual particles and the finite element method (FEM) to describe the bulk behaviour of many grains. To map between FEM and DEM, "coarse-graining" enriched homogenization, a spatial smoothing technique is used. The investigation begins with a comprehensive overview of the governing equations for thermo-mechanical problems, formulated into Galerkin's method of weighted residuals for continuum analysis. The coupling terms for individual physics are then derived and formulated using Galerkin's method. To verify the proposed volume coupling approach, a series of numerical tests are conducted. These tests showcase the approach's capability of accurately describing unsteady heat transfer and thermo-viscoelasticity problems. As an application example, a multi-scale simulation of the laser sintering process is performed. The coupled simulation accurately captures the contact rheology of powder particles at a micro-scale during sintering, while efficiently modelling heat transfer through the particle bed using a macro-scale approach. By combining accuracy and efficiency, this coupling framework allows for the design of multi-physics scenarios.

5.1. INTRODUCTION

The sintering of visco-elastic powders is a complex multi-physical process that has drawn significant attention in the field of materials science and engineering. This process involves subjecting powdered materials to heat and pressure, which triggers a series of physical transformations, leading to the formation of 3D objects. Two crucial physical phenomena are the multi-physics of individual particles where they become sintered and the transition of the material's bulk behavior between discrete and continuum. Addressing these challenges requires a multi-scale approach. Moreover, it helps reduce the computational cost of a simulation where the particle dynamics are solved explicitly, making the model applicable for large-scale industrial applications.

At the micro-scale, the discrete element method (DEM) is a well established and effective technique for simulating the sintering process. This approach involves modelling each particle as a discrete element and applying contact interaction laws to simulate particle-particle interactions. This allows capturing a wide range of mechanical interactions such as elastic, visco-elastic, plastic and dissipation [1, 2]. Furthermore, the contact model can include the contact rheology of the material to take into account either the rate of inter-penetration based on the rate of deformation and sintering mechanism [3–8]. The influence of external heat sources such as the laser beam on the particle dynamics can be well captured through the energy balance [9–12].

The finite element method (FEM) is a widely used technique for describing the behaviour of solid bodies at the macro-scale, particularly useful in analysing the strength and deformation of materials. In the context of sintering, FEM can be utilized to simulate the macroscopic behaviour of powder during the sintering process by accounting for macroscopic phenomena including heat transfer and mechanical deformation [13–15]. FEM has been applied in various investigations, including a 3D

micro-scale model that explored the thermal evolution of porous beds during selective laser sintering of metal powders [16]. Similarly, Chauhan *et al.* [17] conducted a comprehensive study of the thermal behaviour of SS316 using a non-linear, transient, three-dimensional FEM-based simulation with the Simufact Additive tool. Ganci *et al.* [18] proposed a numerical approach to model the selective laser sintering of polypropylene, where a 3D thermal model was developed to predict temperature fields and the extension of the sintered area in the powder bed, taking into account phase change when multiple laser passes.

However, there is still a need for a better understanding of when and where micro-scale resolution is specifically required, such as in selective regions, while also accounting for large-scale simulations. In this investigation, we propose a thermo-mechanical model framework that provides a comprehensive analysis of multi-physics processes. To accomplish this, two open-source software packages are coupled, MercuryDPM [19] and oomph-lib [20], for the analyses at the micro-scale and macro-scale. The coupling between these software packages is achieved using a volume coupling technique previously developed by Cheng *et al.* [21], which we extend in this study to address thermo-mechanical problems. Additionally, the coupling framework is enriched with a micro-macro transition technique, known as "coarse-graining" [22]. An illustration of the modelling approach is provided in Fig. 5.1.
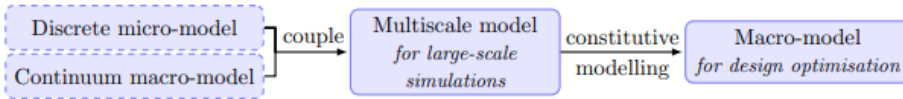
Figure 5.1: Modelling approach.

To verify the implementation of the multi-scale framework, numerical tests are conducted at the micro-scale and the macro-scale respectively, and later put together within the coupling framework. These tests encompass various independent yet interconnected scenarios, including unsteady heat transfer and thermo-viscoelasticity. Furthermore, we report a multi-scale simulation of the selective laser sintering process using a sintering contact model for visco-elastic materials previously developed [8]. The proposed framework enables simulations that consider different effects in distinct media and involve diverse constitutive relations, paving the way for a comprehensive understanding of the influence of material and process parameters at reduced computational costs.

The investigation is organized as follows: Section 5.2 summarizes the governing equations to describe thermo-mechanical problems, the principle of virtual displacements for the finite element formulation, and its implementation within the oomph-lib package [20]. We introduce the volume coupling technique, enriched with coarse-graining in Section 5.3. The numerical examples and discussion are provided in Section 5.4. Finally, Section 5.5 gives the concluding remarks and outlook.

The equations analysed in this document employ two distinct notations: tensor notation and vector notation.

5.2. GOVERNING EQUATIONS IN THERMO-ELASTICITY

The general governing equations used to describe the thermo-elastic behaviour in continuum mechanics are momentum and thermal energy balance equations.

5.2.1. MOMENTUM BALANCE AND ELASTIC DEFORMATION

We consider a solid object occupying the volume V, with the boundary referred to as ∂V. Based on the linear momentum balance equation and infinitesimal strain theory, under the assumption of small deformations, the deformation of a solid body is described by

$$\frac{\partial}{\partial x_j}(\sigma_{ij}) + f_i = \rho \frac{\partial^2 u_i}{\partial t^2}. \tag{5.1}$$

It shows that the second derivative of displacement u_i with respect to time t is proportional to the divergence of the stress tensor σ_{ij} at any referential position $\mathbf{x} \in V$ and time $t \geq t_0$. On the surface A of the solid, we prescribe Neumann boundary conditions by specifying the traction t_i. Thus

$$t_i = \sigma_{ij} n_j \text{ on } x \in A \text{ for } t \geq t_0. \tag{5.2}$$

We further assume that the angular momentum of the body is in equilibrium, and thus the stress tensor is symmetric, at all positions $x \in V, t \geq t_0$, which ensures that the net moment acting on the body is zero.

$$\sigma_{ij} = \sigma_{ji}, \tag{5.3}$$

5.2.2. THERMAL ENERGY FOR AN ISOTROPIC ELASTIC BODY

The transport of thermal energy is assumed to be governed by the first law of heat conduction or Fourier's law. It describes the heat flux q in a material as a function of the temperature gradient ($\frac{\partial T}{\partial x}$), and the thermal conductivity k_{cond} of the material, which is assumed to be isotropic. It can be expressed as

$$q_i = -k_{cond} \frac{\partial T}{\partial x_i}. \tag{5.4}$$

Eq. (5.4) can be applicable for steady-state conditions. However, to account for non-steady or transient conditions, Fick's second law of diffusion may be used. This law is derived from the principle of thermal energy conservation. It states that the time rate of change in the heat density, $\rho c_p T$, is equal to the heat source H applied to the solid body, and the spatial gradient of the heat flux q_i,

$$\rho c_p \frac{\partial T}{\partial t} = -\frac{\partial q_i}{\partial x_i} + H, \tag{5.5}$$

The heat energy equation is thus calculated as

$$\rho c_p \frac{\partial T}{\partial t} = k_{cond} \frac{\partial}{\partial x_i}\left(\frac{\partial T}{\partial x_i}\right) + H. \tag{5.6}$$

Eq. (5.1) and Eq. (5.6) must be simultaneously solved for displacement u_i and the rate of change of temperature with time $\frac{\partial T}{\partial t}$. In the theory of thermo-elasticity, the solution of which requires the determination of temperature and deformation simultaneously, the mechanical work done to balance the flux reads

$$H = \frac{\partial}{\partial x_i}\left(\sigma_{ij}v_i\right),\tag{5.7}$$

where σ_{ij} is the Cauchy stress tensor and v_i is the velocity vector. It represents the work done by the internal force on the displacement of the material, and it is used for coupled thermo-mechanical analyses [23]. However, in the present investigation, we consider only the left part of Eq. (5.6) for the modelling of discrete and solid media. We assume that the changes in temperature do not significantly affect the changes in mechanical deformation, and vice-versa. For this approximation, we should consider [24]:

- The temperature variation is small. The temperature does not induce significant thermal strain.

- Low thermal expansion material. The thermal strain resulting from temperature changes may be negligible.

- High thermal conductivity material. Temperature gradients within the material are minimised, therefore, the thermal effect on mechanical deformation may be small.

- Scenarios where the thermal transients occur faster than the mechanical response time. Thus, the mechanical deformation can be considered independent of temperature changes.

The heat transfer equation (Eq. 5.4) can be generalized to include all three modes of heat transfer: conduction, convection, and radiation. In the present thermo-mechanical coupling implementation, it is only considered heat transfer by conduction.

5.2.3. Principle of virtual displacements

This section presents the formulation of the equilibrium and heat flux equations using the principle of virtual displacements, first in the residual form. The residual form of an equation is a generic class of methods developed to obtain the approximate solution to a differential equation, which allows for the automatic discretization of a problem domain V into elements. Then, the non-dimensionalization of the residual equations to remove physical dimensions is provided, allowing for a sustainable approach to generalize mechanics problems. We assume that the deformable body behaves as a three-dimensional elastic solid and describe its behaviour using finite strain theory. A finite-strain framework is essential to correctly handle the impact of granular materials, in particular for deformable structures that have large displacements and/or geometrical nonlinearity. To be consistent with the implementation described in oomph-lib [20], we adopt the term "element" to represent a total or partial physical volume of the domain, which is assembled to form a common global geometrical object

and governed by the residual constitutive equation. An illustration of a body divided into sub-volumes or *elements*, is presented in Fig. 5.2.
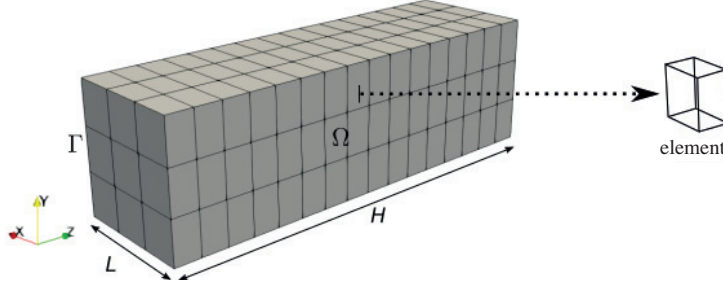
Figure 5.2: The left side of the image shows a discretization of the geometry into smaller sub-volumes, referred to as "elements". The domain is represented by Ω, while Σ denotes the boundary, with H and L representing the height and length, respectively. On the right side, a representative element is depicted, which is governed by a local residual constitutive model.

WORK BALANCE EQUATION

The principle of virtual work (PVW) is a fundamental principle in theoretical and computational mechanics that states that a system is in equilibrium if and only if the virtual work done by external forces (EVW) is equal to the virtual work done by internal forces (IVW). Then, Eq. (5.8) is derived based on the *principle of virtual displacement* $\delta\mathbf{u}$ field in the body. This field is unrelated to the real displacement field in the body and, $\mathbf{u} = \mathbf{X} - \boldsymbol{\xi}$, where $\mathbf{X}$ and ξ are the vectors to define the undeformed and deformed configuration, respectively. $\delta\mathbf{u}$ is arbitrary except that it vanishes on the part of the boundary where the actual displacement field is prescribed, i.e., $\delta\mathbf{u} = 0$ on A. The action of external forces on the body is defined by EVW as

$$EVW = \int_V \left(\mathbf{f} - \rho \frac{\partial \mathbf{u}}{\partial t} \right) \cdot \delta\mathbf{u} \, dV, \tag{5.8}$$

where $\mathbf{p}$ is the external force per unit volume, and V is the volume of the body. Associated with the virtual displacement field is a virtual strain field $\delta\varepsilon_{ij}$, which measures the deformation of the body under virtual displacements. The virtual strain is defined as

$$\delta\varepsilon_{ij} = \frac{1}{2}\left(\frac{\partial \delta u_i}{\partial x_j} + \frac{\partial \delta u_j}{\partial x_i} \right), \tag{5.9}$$

where $\frac{\partial \delta u_i}{\partial x_j}$ and $\frac{\partial \delta u_j}{\partial x_i}$ are the components of the virtual displacement gradient tensor. Since the virtual displacement gradient tensor is symmetric, the virtual strain tensor is also symmetric. To satisfy the principle of virtual work, the internal virtual work (IVW) must be equal to the EVW, and it can be expressed in terms of the 2nd Piola-Kirchhoff stress tensor $\mathbf{S}$ and the Green-Lagrange strain tensor $\boldsymbol{\varepsilon}$ as

$$IVW = \int_V \delta\boldsymbol{\varepsilon} : \mathbf{S}\mathrm{d}V, \tag{5.10}$$

the symbol : denotes the double dot product between two second-order tensors. The 2nd Piola-Kirchhoff stress tensor $\mathbf{S}$ is symmetric and is related to the Cauchy stress tensor $\boldsymbol{\sigma}$ (because finite strain) by

$$\mathbf{S} = \boldsymbol{F}^{-1}\boldsymbol{\sigma}\boldsymbol{F}^{-T}, \tag{5.11}$$

where $\boldsymbol{F}$ is the deformation gradient. Therefore, the principle of virtual work states that a body is in equilibrium if the integral of the difference between the internal forces and the external forces over the volume of the body is zero, i.e.

$$\int_V (\nabla\cdot\boldsymbol{\sigma})\cdot\delta\mathbf{u}\mathrm{d}V + \int_V \mathbf{f}\cdot\delta\mathbf{u},\mathrm{d}V - \int_V \rho\frac{\partial^2\mathbf{u}}{\partial t^2}\cdot\delta\mathbf{u}\mathrm{d}V = 0. \tag{5.12}$$

To transform the volume integral to a surface integral, the divergence theorem is applied as follows

$$\int_V (\nabla\cdot\boldsymbol{\sigma})\cdot\delta\mathbf{u}\mathrm{d}V = \int_{\partial V} (\boldsymbol{\sigma}\cdot\delta\mathbf{u})\cdot\mathbf{n}\mathrm{d}A - \int_V (\boldsymbol{\sigma}\cdot\nabla)\cdot\delta\mathbf{u}\mathrm{d}V. \tag{5.13}$$

where $\mathbf{n}$ is the outward unit normal vector to the surface ∂V. Substituting this into Eq. 5.12, we get

$$\int_{\partial V} (\boldsymbol{\sigma}\cdot\mathbf{n})\cdot\delta\mathbf{u}\mathrm{d}A - \int_V (\boldsymbol{\sigma}\cdot\nabla)\cdot\delta\mathbf{u}\mathrm{d}V + \int_V \mathbf{f}\cdot\delta\mathbf{u}\mathrm{d}V - \int_V \rho\frac{\partial^2\mathbf{u}}{\partial t^2}\cdot\delta\mathbf{u}\mathrm{d}V = 0. \tag{5.14}$$

Recalling the Cauchy stress formulation (Eq. (5.2)) and substituting

$$\int_{\partial V} \mathbf{t}\cdot\delta\mathbf{u}\mathrm{d}A - \int_V \boldsymbol{\sigma} : \delta\boldsymbol{\varepsilon}\mathrm{d}V + \int_V \mathbf{f}\cdot\delta\mathbf{u}\mathrm{d}V - \int_V \rho\frac{\partial^2\mathbf{u}}{\partial t^2}\cdot\delta\mathbf{u}\mathrm{d}V = 0. \tag{5.15}$$

Re-arranging Eq. (5.15) gives

$$\int_V \left\{ \boldsymbol{\sigma} : \delta\boldsymbol{\varepsilon} - \left(\mathbf{f} - \rho\frac{\partial^2\mathbf{u}}{\partial t^2}\right)\cdot\delta\mathbf{u} \right\}\mathrm{d}V - \int_{\partial V} \mathbf{t}\cdot\delta\mathbf{u}\mathrm{d}A = 0. \tag{5.16}$$

Eq. (5.16) represents the equilibrium equation using virtual displacements. It must be augmented by a constitutive equation that determines the stress as a function of the body's deformation, (and possibly the history of its deformation).

HEAT BALANCE EQUATION

To derive the heat balance equation with the virtual temperature, the thermal energy equation is recalled (Eq.(5.6)), in differential form

$$\rho c_p \frac{\partial T}{\partial t} = \nabla\cdot(k_{cond}\nabla T) + H. \tag{5.17}$$

Multiplying both sides by the virtual temperature variation δT and integrating over the volume V gives

$$\int_V \left(\rho c_p \frac{\partial T}{\partial t}\right)\delta T \mathrm{d}V = \int_V [\nabla\cdot(k_{cond}\nabla T)]\delta T \mathrm{d}V + \int_V H\delta T \mathrm{d}V. \tag{5.18}$$

Eq.(5.18) is the heat balance equation with the virtual temperature, which relates the time rate of change of the energy in a control volume to the fluxes of energy due to conduction and generation of heat. The first right term in Eq. (5.18) has second-order derivatives. We will convert these into first-order derivatives using the divergence theorem. First,

$$\int_V [\nabla\cdot k_{cond}\nabla T]\delta T \mathrm{d}V = \int_V \nabla\cdot[\delta T(k_{cond}\nabla T)]\mathrm{d}V - \int_V (\nabla\delta T)\cdot(k_{cond}\nabla T)\mathrm{d}V. \tag{5.19}$$

Applying the divergence theorem to the first term on the right-hand side,

$$\int_V \nabla\cdot[\delta T(k_{cond}\nabla T)]\mathrm{d}V = \int_{\partial V} [\delta T(k_{cond}\nabla T)]\cdot\mathbf{n}\mathrm{d}A. \tag{5.20}$$

Substituting in Eq. (5.18),

$$\begin{aligned}
\int_V \left(\rho c_p \frac{\partial T}{\partial t}\right)\delta T \mathrm{d}V = &\int_{\partial V} [\delta T(k_{cond}\nabla T)]\cdot\mathbf{n}\mathrm{d}A \\
&- \int_V (\nabla\delta T)\cdot(k_{cond}\nabla T)\mathrm{d}V + \int_V H\delta T \mathrm{d}V.
\end{aligned} \tag{5.21}$$

After rearrangement, we get the weak form of the heat equation

$$\begin{aligned}
\int_V \left(\rho c_p \frac{\partial T}{\partial t}\right)\delta T \mathrm{d}V + \int_V (\nabla\delta T)\cdot(k_{cond}\nabla T)\mathrm{d}V = \\
+ \int_{\partial V} [\delta T(k_{cond}\nabla T)]\cdot\mathbf{n}\mathrm{d}A + \int_V H\delta T \mathrm{d}V.
\end{aligned} \tag{5.22}$$

Expressing the flux in normal direction as $q_n = -(k_{cond}\nabla T)\cdot\mathbf{n}$, we get

$$\begin{aligned}
\int_V \left(\rho c_p \frac{\partial T}{\partial t}\right)\delta T \mathrm{d}V + \int_V (\nabla\delta T)\cdot(k_{cond}\nabla T)\mathrm{d}V = \int_{\partial V} \delta T q_n \mathrm{d}A \\
+ \int_V H\delta T \mathrm{d}V.
\end{aligned} \tag{5.23}$$

Finally, assuming the residual is zero,

$$\begin{aligned}
\int_V \left(\rho c_p \frac{\partial T}{\partial t}\right)\delta T \mathrm{d}V + \int_V (\nabla\delta T)\cdot(k_{cond}\nabla T)\mathrm{d}V - \int_{\partial V} \delta T q_n \mathrm{d}A \\
- \int_V H\delta T \mathrm{d}V = 0.
\end{aligned} \tag{5.24}$$

NON-DIMENSIONALISATION

For convenience, Eq.(5.16) and Eq.(5.24) are expressed in terms of dimensionless quantities, and the scaling is now introduced based on the procedure presented in oomph-lib [20]. Henceforth, dimensional quantities are denoted with a "∗" superscript. First, the equation of motion (Eq. 5.16) is considered,

$$\int_V \left\{ \boldsymbol{\sigma}^* : \delta \boldsymbol{\varepsilon} - \left(\mathbf{f}^* - \rho \frac{\partial^2 \mathbf{u}^*}{\partial t^{*2}} \right) \cdot \delta \mathbf{u}^* \right\} \mathrm{d}V^* - \int_{\partial V} \mathbf{t}^* \cdot \delta \mathbf{u}^* \mathrm{d}A^* = 0. \tag{5.25}$$

Some quantities such as strain are already dimensionless, while others, such as density, do not have any non-dimensional counterparts. To non-dimensionalize the remaining quantities in all our examples, the length is scaled with a problem-specific length-scale $\mathcal{L}$, which is chosen to be the length of the solid body as shown in Fig. 5.2, and the timescale is scaled by $\mathcal{T}$, which is the timescale of interest, so that

$$\mathbf{X}^* = \mathcal{L}\mathbf{X}, \quad t^* = \mathcal{T} t. \tag{5.26}$$

To define the remaining variables, the nodal position $\mathbf{x}$, the deformed position $\mathbf{X}^*$, the differential of boundary area $\mathrm{d}A^*$, and the differential of domain volume $\mathrm{d}V^*$ are made dimensionless with the following expressions

$$\mathbf{x}^* = \mathcal{L}\mathbf{x}, \quad \mathrm{d}A^* = \mathcal{L}^2 \mathrm{d}A, \quad \mathrm{d}V^* = \mathcal{L}^3 \mathrm{d}V. \tag{5.27}$$

Subsequently, the characteristic stiffness $\mathcal{S}$ (in the following sections we use the material's Young's modulus) is used to non-dimensionalise the stress and the loads as

$$\boldsymbol{\sigma}^* = \mathcal{S}\boldsymbol{\sigma}, \quad \mathbf{t}^* = \mathcal{S}\mathbf{t}, \quad \mathbf{b}^* = \mathcal{S}/\mathcal{L}\,\mathbf{b}. \tag{5.28}$$

It transforms Eq. (5.25) into

$$\int_V \left\{ \boldsymbol{\sigma} : \delta \boldsymbol{\varepsilon} - \left(\mathbf{p} - \Lambda^2 \frac{\partial^2 \mathbf{u}}{\partial t^2} \right) \cdot \delta \mathbf{u} \right\} \mathrm{d}V - \int_{\partial V} \mathbf{t} \cdot \delta \mathbf{u} \mathrm{d}A = 0, \tag{5.29}$$

where Λ^2 is the ratio of the material-specific "intrinsic" and the problem-specific (extrinsic) time scales, defined by

$$\Lambda^2 = \frac{\mathcal{L}}{\mathcal{T}} \sqrt{\frac{\rho}{\mathcal{S}}}. \tag{5.30}$$

and,

$$T_{intrinsic} = \mathcal{L} \sqrt{\frac{\rho}{\mathcal{S}}}. \tag{5.31}$$

The temperature is non-dimensionalised by introducing a temperature scale $\mathcal{T}_T$, and the distance is non-dimensionalised using the same characteristic length scale $\mathcal{L}$, as described earlier. This gives

$$\int_V \left(\rho c_p \frac{\partial T^*}{\partial t^*}\right) \delta T^* \mathrm{d}V^* - \int_V (\nabla \delta T^*) \cdot (k_{cond}^* \cdot \nabla T^*) \mathrm{d}V^*$$
$$+ \int_{\partial V} \delta T^* q^* \mathrm{d}A^* = 0. \tag{5.32}$$

Scaling,

$$T^* = T_{ref} + \Delta T T, \quad k_{cond}^* = k_{ref} \beta, \quad q^* = k_{ref} \frac{\Delta T}{\mathscr{L}} q, \tag{5.33}$$

where δT^* is the virtual temperature variation that satisfies the boundary and initial conditions. T_{ref} is a reference temperature and ΔT is a characteristic temperature difference. β is the non-dimensionalised thermal conductivity. Subsequently, introducing α as the non-dimensional thermal inertia

$$\alpha = \frac{\rho c_p}{k_{cond}} \frac{\rho^2}{\mathscr{T}}. \tag{5.34}$$

Therefore,

$$\int_V \left\{\alpha \frac{\partial T}{\partial t}\right\} \delta T \mathrm{d}V + \int_V (\nabla \delta T) \cdot (\beta \nabla T) \mathrm{d}V - \int_{\partial V} \delta T q_n \mathrm{d}A$$
$$- \int_V H \delta T \mathrm{d}V = 0. \tag{5.35}$$

5.2.4. THERMO-ELASTICITY FOR SMALL DEFORMATIONS

To solve a thermo-elastic problem described by Eq.(5.29) and Eq.(5.35), a set of boundary conditions needs to be provided. These boundary conditions may include specified displacements, tractions, and temperatures on the boundaries of the domain. Additionally, an initial position, initial velocity, and initial temperature must be specified. The full solution of the nonlinear equations of thermo-elasticity is challenging and is typically treated numerically. However, the system can be simplified by linearizing it to a known strain-free state. In general, non-linearity in continuum mechanics problems arises from two sources: 1) geometric non-linearity, which occurs when the displacements are large and 2) material non-linearity, which results from the constitutive law[1]. By assuming that the deformations are infinitesimal and the constitutive law is linear, it is possible to construct a theory in which the deformations are small, but the material behaviour has a non-linearity. It may be assumed that

$$\mathbf{R} = \mathbf{r} + \mathbf{u} = \mathbf{r} + \Phi \tilde{\mathbf{u}}, \tag{5.36}$$

where $\mathbf{R}$ represents the displacement vector, $\mathbf{r}$ the vector of the reference position, and $\mathbf{u}$ the displacement vector. $\tilde{\mathbf{u}}$ is a perturbation vector that represents the small deviations from the reference displacement $\mathbf{u}$ in $O(1)$. $\Phi \ll 1$ is a small parameter, which is used to scale the perturbation $\mathbf{u}$ to ensure it remains small. Similarly,

$$T = T_0 + \Phi \tilde{T}, \tag{5.37}$$

[1]Andrew Hazel. MATH 45061: Continuum mechanics - Chapter 6: Elasticity. The University of Manchester.

where T represents the temperature at a point in the material. T_0 is the initial temperature, $\tilde{T}$ represents the perturbation. For problems where the temperature distribution changes smoothly over time without sharp variations or discontinuities, the time rate of change of the dilation is expected to be roughly equivalent to that of the temperature, implying that no significant lag or vibrations in the motion of the body should arise. Early in the development of thermo-elastic theory, it was considered whether the inertia terms in the equations could be neglected [23]. It was concluded that the time rate of change of temperature is slow enough that these terms should not be significant. When an external mechanical agency produces strain variations within a body, it generally also causes temperature variations, resulting in a flow of heat and an increase in entropy and energy stored in an irrecoverable manner. However, deformations due to external loads typically only result in small temperature changes, so it is reasonable to calculate these deformations without taking into account thermal expansion. If strains are produced in a body due to a non-uniform temperature distribution, the influence of these strains on the temperature itself should not be too significant. The coupling mechanical term that appears in the heat Eq. (5.7) can be disregarded for all problems except those in which thermo-elastic dissipation is of primary interest. For problems with smoothly changing temperature distributions, an uncoupling process can be considered, where the time history of the displacements closely follows that of the temperature. In isotropic thermo-elastic solid bodies, shear waves are not affected by thermal effects [24, 25].

5.2.5. Constitutive law for thermo-elasticity

To model the thermo-elastic behaviour of a body, the material constitutive relation needs to be specified. For this analysis, the linear Hookean law under the influence of thermal expansion is used to describe the behaviour of small deformations [26]. From Hooke's law, the stress tensor is related to the strain tensor, or the displacement components, and temperature change ΔT as

$$\sigma_{ij} = C_{ijkl}\varepsilon_{kl} + \gamma_{ij}\Delta T, \tag{5.38}$$

where C_{ijkl} is the material 4th-order stiffness tensor, i, j, k, l as referring to the three-dimensional Cartesian coordinate system, which for isotropic materials can be assumed symmetric $C_{ijkl} \approx E$. The strain is denoted by ε_{kl}, γ represents the thermal expansion. Recalling Eq.(5.29) and using Eq.(5.38), it becomes

$$\int_V \left\{ \left(E\varepsilon + \gamma\Delta T \right) : \delta\boldsymbol{\varepsilon} - \left(\mathbf{f} - \Lambda^2 \frac{\partial^2 \mathbf{u}}{\partial t^2} \right) \cdot \delta\mathbf{u} \right\} \mathrm{d}V - \int_{\partial V} \mathbf{t} \cdot \delta\mathbf{u}\mathrm{d}A = 0. \tag{5.39}$$

Eq.(5.39) represents the virtual work equation for a linearly elastic material subject to both mechanical and thermal loads. The equation represents a generalisation of the principle of Lagrange's virtual work for thermo-elastic problems, by incorporating the stress tensor as a function of temperature. It can be treated as an isotropic growth problem assuming a linear dilatation for small deformations and defining the strain as a function of the deformed and undeformed metric tensors such as

$$\varepsilon_{ij} = \frac{1}{2}(G_{ij} - \tilde{g}_{ij}) = \frac{1}{2}(G_{ij} - \Gamma^{2/d}(X^k)g_{ij}), \tag{5.40}$$

where G_{ij} is metric tensor in the deformed configuration, g_{ij} is the metric tensor, d is the body's spatial dimension. The components of the covariant metric tensor are defined via the inner products

$$g_{ij} = \mathbf{g}_i \cdot \mathbf{g}_j, \tag{5.41}$$

where

$$\mathbf{g}_i = \frac{\partial \mathbf{r}}{\partial \xi^i}, \tag{5.42}$$

where ξ^i represents a set of the Lagrangian coordinates, to parametrise the (Eulerian) position vector to material points in the body's undeformed position:

$$\mathbf{r} = \mathbf{r}(\xi^i). \tag{5.43}$$

As the body deforms, the Lagrangian coordinates remain "attached" to the same material points, The body's deformation can therefore be described by the vector field that specifies the position vector to material points in the deformed configuration,

$$\mathbf{R} = \mathbf{R}(\xi^i). \tag{5.44}$$

As in the undeformed coordinate system, it forms the tangent vectors to the deformed coordinates lines $\xi^i = const.$ and denote by

$$\mathbf{G}_i = \frac{\partial \mathbf{R}}{\partial \xi^i}. \tag{5.45}$$

The inner product of these vectors defines the metric tensor in the deformed configuration

$$G_{ij} = \mathbf{G}_i \cdot \mathbf{G}_j. \tag{5.46}$$

In general, the displacements induced by such isotropic expansion will be incompatible and it would be impossible to (re-)assemble the individually grown material elements to a continuous body unless the material elements undergo some deformation. The elements' deformation relative to their stress-free shape will generate internal "growth stresses". when subjected to external loads and body forces the body will undergo further deformations until the stress balances the applied loads.

5.2.6. FINITE ELEMENT IMPLEMENTATION IN OOMPH-LIB

Within oomph-lib, thermo-mechanical problems are regarded as nonlinear and it is assumed that the problem is discretised in time and space [20]. i.e. the problem's (approximate) solution must be represented by M discrete values $V_j(j = 1, ..., M)$; the nodal values in a finite-element mesh. Boundary conditions and other constraints prescribe some of these values, and so only a subset of the M values are unknown.

These unknowns are denoted by $U_i (i = 1, ..., N)$ and assume that they are determined by a system of N non-linear algebraic equations that may be written in the residual form. It is,

$$\mathcal{R}_i(U_1, ..., U_N) = 0 \ \text{ for } i = 1, ..., N. \tag{5.47}$$

To solve the above system, oomph-lib uses Newton's method. The method requires the provision of an initial guess for the unknowns and the repeated solution of the linear system

$$\sum_{i=1}^{N} \mathcal{J}_{ij} \delta U_j = -\mathcal{R}_i \ \text{ for } i = 1, ..., N \tag{5.48}$$

where,

$$\mathcal{J}_{ij} = \frac{\partial \mathcal{R}_i}{\partial U_j}, \ \text{ for } j = 1, ..., N \tag{5.49}$$

is the Jacobian matrix. The solution of the linear system is followed by an update of the unknowns,

$$U_i := U_i + \delta U_i \ \text{ for } i = 1, ..., N. \tag{5.50}$$

The solutions are repeated until the infinity norm of the residual vector $||\mathcal{R}||_\infty$ is sufficiently small. Therefore, implemented a finite-element-type framework in which each "element" provides a contribution to the global Jacobian matrix $\mathcal{J}$, and to the global residual vector, $\mathcal{R}$.

DOMAIN DISCRETISATION

The discretisation is developed via an isoparametric Galerkin approach, in which the domain is divided into elements, and for each element geometric shape functions $\psi_i(x_j)$ (basis functions) are used. In order to represent the unknown vector field $\mathbf{U}(X^j)$ using the basis functions, the following approximation is made

$$U_i(X^k) = \sum_{j=1}^{N} U_{ij} \psi_j(X^k), \tag{5.51}$$

where U_{ij} is treated as the unknown Eulerian nodal position. With this discretisation, the variations in $\mathbf{x}(X^j)$ correspond to variations in the nodal positions X_{ij}, so that

$$\delta \mathbf{U} = \sum_{j=1}^{N} \delta X_{ij} \psi_j \mathbf{e}_i, \tag{5.52}$$

and

$$\frac{\partial \delta \mathbf{U}}{\partial X^k} = \sum_{j=1}^{N} \delta X_{ij} \frac{\partial \psi_j}{\partial X^k} \mathbf{e}_i. \tag{5.53}$$

Making use of the shape functions, the resulting equilibrium equation (Eq. (5.29)) in discretised form using the index notation is

$$
\sum_{k=1}^{N}\sum_{m=1}^{N}\left\{\int_{V}\left[\sum_{i}^{3}\sum_{j}^{3}\sigma_{ij}\left(\sum_{l=1}^{N}X_{kl}\frac{\partial\psi_{l}}{\partial X_{i}}\right)\frac{\partial\psi_{m}}{\partial X_{j}}-\left(f_{k}-\Lambda^{2}\left(\sum_{l=1}^{N}\frac{\partial^{2}X_{kl}}{\partial t^{2}}\psi_{l}\right)\right)\psi_{m}\right]\mathrm{d}V\right.
$$
$$
\left.-\int_{\partial V}t_{k}\psi_{m}\mathrm{d}A\right\}\delta X_{km}=0.
\tag{5.54}
$$

Note that in the equilibrium equation, the contribution of each element to the global Jacobian matrix and the global residual vector is calculated via the integration over its volume and boundary, respectively. The displacement boundary condition determines the positions of all nodes that are located on the boundary A. It also requires that their variations vanish,

$$
X_{ij} = x^{BC}(\Xi_{lj}) \text{ if node j is located on A.}
\tag{5.55}
$$

and

$$
\delta X_{ij} = 0 \text{ if node j is located on A.}
\tag{5.56}
$$

The variations of all other nodal positions are arbitrary (and independent of each other). Therefore, the terms in the curly brackets in Eq.(5.57) must vanish individually. This provides one (discrete) equation for each unknown U_{km}. Finally, this set of equations can be assembled in an element-by-element fashion.

Assuming small displacements and small displacement gradients, the small-strain tensor can decompose into its elastic and viscous components including a dissipative parameter μ. It gives,

$$
\sum_{k=1}^{N}\sum_{m=1}^{N}\left\{\int_{V}\left[\sum_{i}^{3}\sum_{j}^{3}\sigma_{ij}\left(\sum_{l=1}^{N}X_{kl}\frac{\partial\psi_{l}}{\partial X_{i}}\right)\frac{\partial\psi_{m}}{\partial X_{j}}-\left(f_{k}-\Lambda^{2}\sum_{l=1}^{N}\left(\frac{\partial^{2}X_{kl}}{\partial t^{2}}-\mu\frac{\partial X_{kl}}{\partial t}\right)\psi_{l}\right)\psi_{m}\right]\mathrm{d}V\right.
$$
$$
\left.-\int_{\partial V}t_{k}\psi_{m}\mathrm{d}A\right\}\delta X_{km}=0.
\tag{5.57}
$$

The heat equation (Eq.(5.35)) can also be expressed in a discrete form using the following discretisation:

$$
T = \sum_{l=1}^{N}T_{l}\psi_{l},
\tag{5.58}
$$

$$
\dot{T} = \sum_{l=1}^{N}\dot{T}_{l}\psi_{l},
\tag{5.59}
$$

$$
\frac{\partial T}{\partial X_{i}} = \sum_{l=1}^{N}T_{l}\frac{\partial\psi_{l}}{\partial X_{i}},
\tag{5.60}
$$

$$\delta T = \sum_{m=1}^{N} \delta T_m \psi_m \tag{5.61}$$

$$\frac{\partial \delta T}{\partial X_i} = \sum_{m=1}^{N} \delta T_m \frac{\partial \psi_m}{\partial X_i}, \tag{5.62}$$

$$H = \sum_{l=1}^{N} H_l \psi_l. \tag{5.63}$$

Then,

$$\int_V \alpha \, \dot{T} \delta T \mathrm{d}V + \beta \int_V \nabla T \cdot \nabla \delta T \mathrm{d}V - \int_{\partial V} q_\mathrm{n} \delta T \mathrm{d}A \\ - \int_V H \delta T \mathrm{d}V = 0, \tag{5.64}$$

yields

$$\sum_{m=1}^{N} \left[\int_V \alpha \sum_{l=1}^{N} \dot{T}_l \psi_l \psi_m \mathrm{d}V + \beta \sum_{l=1}^{N} \int_V T_l \frac{\partial \psi_l}{\partial X_i} \frac{\partial \psi_m}{\partial X_i} dV - \int_{\partial V} q_n \psi_m dA \\ - \int_V \sum_{l=1}^{N} H_l \psi_l \psi_m \mathrm{d}V \right] \delta T_m = 0 \tag{5.65}$$

Eq.(5.65) can be assembled as an external source to Eq.(5.57), i.e. in the same fashion as the traction condition is assembled, and the derivatives approximated by finite differences.

Overall, the assembly of the multi-physics problem contains the elastic (W_E), inertia (W_I), dissipation (W_D), traction (W_T), conductivity (W_K), thermal capacity (W_{KT}), flux (W_Q) and internal heat generation (Q_H) contributions as

$$W_E + W_I + W_D + W_T + W_K + W_{KT} + W_Q + Q_H = 0. \tag{5.66}$$

where

$$W_E = \sum_{k=1}^{N} \sum_{m=1}^{N} \left\{ \int_V \left[\sum_{i=1}^{3} \sum_{j=1}^{3} \sigma_{ij} \left(\sum_{l=1}^{N} X_{kl} \frac{\partial \psi_l}{\partial X_i} \right) \frac{\partial \psi_m}{\partial X_j} \right] \mathrm{d}V \right\} \delta X_{km}, \tag{5.67}$$

$$W_I = \sum_{k=1}^{N} \sum_{m=1}^{N} \left\{ -\int \left[\left(f_k - \Lambda^2 \left(\sum_{l=1}^{N} \frac{\partial^2 X_{kl}}{\partial t^2} \psi_l \right) \right) \psi_m \right] \mathrm{d}V \right\} \delta X_{km}, \tag{5.68}$$

$$W_D = \sum_{k=1}^{N} \sum_{m=1}^{N} \left\{ -\int \left[\left(\Lambda^2 \mu \sum_{l=1}^{N} \frac{\partial X_{kl}}{\partial t} \psi_l \right) \psi_m \right] \mathrm{d}V \right\} \delta X_{km}, \tag{5.69}$$

$$W_T = \sum_{k=1}^{N} \sum_{m=1}^{N} \left\{ -\int_A t_k \psi_m \mathrm{d}A \right\} \delta X_{km}, \tag{5.70}$$

$$W_K = \sum_{m=1}^{N} \left[\beta \sum_{l=1}^{N} \int_V T_l \frac{\partial \psi_l}{\partial X_i} \frac{\partial \psi_m}{\partial X_i} dV \right] \delta T_m, \tag{5.71}$$

$$W_{KT} = \sum_{m=1}^{N} \left[\int_V \alpha \sum_{l=1}^{N} \dot{T}_l \psi_l \psi_m dV \right] \delta T_m, \tag{5.72}$$

$$W_Q = -\sum_{m=1}^{N} \left[\int_{\partial V} q_n \psi_m dA \right] \delta T_m, \tag{5.73}$$

$$W_H = -\sum_{m=1}^{N} \left[\int_V \sum_{l=1}^{N} H_l \psi_l \psi_m dV \right] \delta T_m. \tag{5.74}$$

5.3. COUPLING THE DISCRETE AND CONTINUUM

After having formulated thermo-viscoelasticity using the oomph-lib implementation of FEM, let us dive into the volume coupling between the discrete element method (DEM) and FEM to perform multi-scale analyses. The coupling is based on the decomposition domain method with the weighting of all governing equations. We have extended the formulation of the coupling method previously developed by Cheng *et al.* [21] for mechanical problems for thermo-elasticity. Fig. 5.3 illustrates the mapping of the velocity vector and temperature of a discrete element onto the FEM nodes.
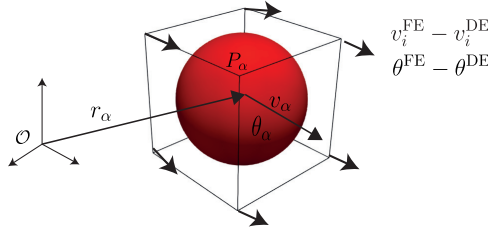
Figure 5.3: Mapping of discrete particle velocity and temperature $(\vec{v}_\alpha^{DE}, \theta_\alpha^{DE})$ onto FEM nodes $(\vec{v}_i^{DE}, \theta^{FE})$. The arrow represents the difference between the DEM solution mapped from the discrete particles and the FEM solution.

First, the coupling weight $w(\mathbf{x})$ is defined as a monotonic function of the position vector $\mathbf{x}$ in the DEM subdomain, and subsequently $1 - w(\mathbf{X})$ in the FEM subdomain, with

$$\begin{aligned} w(\mathbf{x}) &= 1 \ \ \forall \mathbf{x} \in \Omega^{DE} \setminus \Omega^C, \\ w(\mathbf{x}) &= 0 \ \ \forall \mathbf{x} \in \Omega^{FE} \setminus \Omega^C, \\ w(\mathbf{x}) &\in \ [0,1] \ \ \forall \mathbf{x} \in \Omega^C. \end{aligned} \tag{5.75}$$

Here, Ω^{DE} and Ω^{FE} represent the discrete and solid domains, respectively, and Ω^C denotes the interface between these two domains.

5.3.1. COUPLED GOVERNING EQUATIONS

The governing equations for the linear momentum balance of the continuum (see Eq.(5.16)) and the discrete elements are as follows.

$$\int_V \left\{ \boldsymbol{\sigma} : \delta\boldsymbol{\varepsilon} - \left(\mathbf{f} - \rho\frac{\partial^2 \mathbf{u}}{\partial t^2} \right) \cdot \delta\mathbf{u} \right\} \mathrm{d}V - \int_{\partial V} \mathbf{t} \cdot \delta\mathbf{u}\mathrm{d}A = 0, \tag{5.76}$$

where ρ is the density of the undeformed body, $\mathbf{f}$ is a body force density acting on the domain Ω, and $\mathbf{t}$ denotes surface traction acting on a subset of the body's boundary, $\Gamma_t \subset \partial\Omega^{\mathrm{FE}}$. $\boldsymbol{\sigma}$ and $\boldsymbol{\varepsilon}$ are a work conjugate pair of stress and strain tensors, and $\delta\mathbf{X}$ and $\delta\boldsymbol{\varepsilon}$ are the virtual variations of the position vector and strain tensor.

$$m_\alpha \frac{\mathrm{d}\mathbf{v}_\alpha}{\mathrm{d}t} - \mathbf{f}_\alpha^b - \sum_{\beta=1}^{N_\alpha} \mathbf{f}_{\alpha\beta} = 0, \tag{5.77}$$

where $\mathbf{f}_\alpha^b$ is the body force acting at the discrete particle position $\mathbf{x}_\alpha$ and $\mathbf{f}_{\alpha\beta}$ are the contact force acting at the contact point $\mathbf{x}_{\alpha\beta}^c$ for $\beta = 1,...,N_\alpha$, denoting the contact partners of particles $\alpha = 1,...,N_p$.

Multiplying the governing equations with their respective coupling weights, for δW^{FE} and δW^{DE} give the weighted sum of the total virtual work $\delta W = \delta W^{FE} + \delta W^{DE}$, with

$$\delta W^{\mathrm{FE}} = \sum_{e=1}^{N_e} \int_{\Omega_e^{\mathrm{FE}}} (1-w) \left\{ \boldsymbol{\sigma} : \delta\boldsymbol{\varepsilon} - \left(\mathbf{f} - \rho\frac{\partial^2 \mathbf{X}}{\partial t^2} \right) \cdot \delta\mathbf{X} \right\} \mathrm{d}V$$
$$+ \sum_{r=1}^{N_r} \int_{\Gamma_r^{\mathrm{FE}}} \mathbf{t} \cdot \delta\mathbf{X}\mathrm{d}A. \tag{5.78}$$

$$\delta W^{\mathrm{DE}} = \sum_{\alpha=1}^{N_p} \left[w_\alpha \left(m_\alpha \frac{\mathrm{d}^2 \mathbf{x}_\alpha}{\mathrm{d}t^2} - \mathbf{f}_\alpha^b \right) - \sum_{\beta=1}^{N_\alpha} w_{\alpha\beta}\mathbf{f}_{\alpha\beta} \right] \cdot \delta\mathbf{x}_\alpha, \tag{5.79}$$

where N_e and N_r are the total numbers of volume and surface elements in Ω and Γ_t, respectively, and N_p is the number of discrete particles. We use the short-hand notation $w(\mathbf{x}_\alpha)$ and $w(\mathbf{x}_{\alpha\beta}^c)$ for the weights at the particle positions and contact points. $\delta\mathbf{x}_\alpha$ is a variation of the position of particle α.

We require the difference between the FEM and DEM displacements in the last time step, $\mathbf{u}^{\mathrm{FE}} = \mathbf{X}|_t - \mathbf{X}|_{t-\mathrm{d}t}$ and $\mathbf{u}^{\mathrm{DE}} = \mathbf{v}^{\mathrm{DE}}\mathrm{d}t$, to be vanishingly small at the macroscopic scale. A continuous particle velocity field $\mathbf{v}^{\mathrm{DE}}$ is defined using coarse-graining that will be introduced later, in Section. 5.3.2. To enforce the kinematic constraint on Ω^C, we penalize the field of the displacement difference at the macroscopic scale $\mathbf{u}^{\mathrm{FE}} - \mathbf{u}^{\mathrm{DE}}$. This gives rise to an additional term in the virtual work equation, $\delta W = \delta W^{FE} + \delta W^{DE} + \delta C$, with

$$\delta C = \epsilon \int_{\Omega^C} (\mathbf{u}^{\mathrm{DE}} - \mathbf{u}^{\mathrm{FE}}) \cdot (\delta\mathbf{x} - \delta\mathbf{X})\mathrm{d}V$$
$$= \underbrace{\epsilon \int_{\Omega^C} (\mathbf{u}^{\mathrm{DE}} - \mathbf{u}^{\mathrm{FE}}) \cdot \delta\mathbf{x}\mathrm{d}V}_{:=\delta C^{\mathrm{DE}}} + \underbrace{\epsilon \int_{\Omega^C} (\mathbf{u}^{\mathrm{FE}} - \mathbf{u}^{\mathrm{DE}}) \cdot \delta\mathbf{X}\mathrm{d}V}_{:=\delta C^{\mathrm{FE}}}, \tag{5.80}$$

where ϵ is the penalty parameter, which must be strictly positive in the overlapping domain to avoid the singular values. $\mathbf{u}^{\text{DE}}$ and $\mathbf{u}^{\text{FE}}$ are the displacement fields interpolated via the finite element basis functions $\psi_i (i = 1, ..., N)$, respectively, $\delta\mathbf{x}$ and $\delta\mathbf{X}$ denote the variation of position vector at the microscopic and macroscopic scales. Substituting $\mathbf{u}^{\text{FE}} = \sum_{j=1}^{N} \mathbf{u}_j^{\text{FE}} \psi_j$, $\mathbf{u}^{\text{DE}} = \sum_{j=1}^{N} \mathbf{u}_j^{\text{DE}} \psi_j$, $\delta\mathbf{X} = \sum_{i=1}^{N} \delta\mathbf{X}_i \psi_i$, and $\delta\mathbf{x} = \sum_{i=1}^{N} (\sum_{\alpha=1}^{N_p} \Pi_{i\alpha} \delta\mathbf{x}_\alpha) \psi_i$, the discretized forms of δC become

$$
\begin{aligned}
\delta C^{\text{FE}} \quad &= \int_{\Omega^{\text{C}}} \epsilon \underbrace{(\mathbf{u}^{\text{FE}} - \mathbf{u}^{\text{DE}})}_{:= -\mathbf{b}^C} \cdot \delta\mathbf{X} dV \\
&= \sum_{i=1}^{N} \epsilon \underbrace{\sum_{j=1}^{N} \int_{\Omega^{\text{C}}} \psi_i \psi_j dV (\mathbf{u}^{\text{FE}} - \mathbf{u}^{\text{DE}})}_{:= -\mathbf{f}_i^C} \cdot \delta\mathbf{X}_i.
\end{aligned}
\tag{5.81}
$$

$$
\begin{aligned}
\delta C^{\text{DE}} \quad &= \int_{\Omega^{\text{C}}} \epsilon (\mathbf{u}^{\text{DE}} - \mathbf{u}^{\text{FE}}) \cdot \delta\mathbf{x} dV \\
&= \sum_{\alpha=1}^{N_p} \epsilon \underbrace{\sum_{i=1}^{N} \sum_{j=1}^{N} \int_{\Omega^{\text{C}}} \psi_i \psi_j dV (\mathbf{u}^{\text{DE}} - \mathbf{u}^{\text{FE}}) \cdot \Pi_{j\alpha}}_{:= -\mathbf{f}_\alpha^C} \cdot \delta\mathbf{X}_\alpha.
\end{aligned}
\tag{5.82}
$$

where $\Pi_i\alpha$ denotes the projection matrix between the discrete particles and finite elements, α iterates from 1 to N_p, with N_p being the total number of discrete particles per coupled finite element. Substituting Eq. (5.81) and Eq. (5.82) into the virtual work equation δW yields

$$
\begin{aligned}
\delta W = \sum_{e=1}^{N_e} \int_{\Omega_e^{\text{FE}}} (1-w) \left\{ \boldsymbol{\sigma} : \delta\boldsymbol{\varepsilon} - \left(\mathbf{f} + \frac{1}{1-w} \mathbf{b}^C - \rho \frac{\partial^2 \mathbf{X}}{\partial t^2} \right) \cdot \delta\mathbf{X} \right\} \\
textdV \\
+ \int_{\Gamma_r^{\text{FE}}} \mathbf{t} \cdot \delta\mathbf{X} dA + \sum_{\alpha=1}^{N_p} \left[w_\alpha \left(m_\alpha \frac{d^2 \mathbf{x}_\alpha}{dt^2} - \mathbf{f}_\alpha^b - \frac{1}{w_\alpha} \mathbf{f}_\alpha^C \right) - \sum_{\beta=1}^{N_\alpha} w_{\alpha\beta} \mathbf{f}_{\alpha\beta} \right] \cdot \delta\mathbf{x}_\alpha.
\end{aligned}
\tag{5.83}
$$

Similar to the governing equation for linear momentum conservation, the energy balance equations for the continuum (Eq. (5.24), only taking into account the heat transfer within the volume) and the discrete system are coupled using FEM and DEM.

$$
\int_V \left\{ \rho c_p \frac{\partial T}{\partial t} + k_{cond} \nabla^2 T \right\} \delta T dV = 0
\tag{5.84}
$$

and,

$$
\rho_\alpha c_{p,\alpha} \frac{dT_\alpha}{dt} + \sum_{\beta=1}^{n_\alpha} k_{cond,\alpha} (T_\beta - T_\alpha) \frac{a_{\alpha\beta}}{l_{\alpha\beta}} = 0,
\tag{5.85}
$$

where ρ_α is the particle density, $c_{p,\alpha}$ is the specific heat of the material, T_α, T_β are the temperatures of particles α, β, respectively. $k_{cond,\alpha}$ is the conductivity of the material, $l_{\alpha\beta}$ and $a_{\alpha\beta}$ are the distance between the centres of particles and the contact area,

respectively. Now, multiplying the governing equations with their respective coupling weights for δH^{FE} and δH^{DE} gives the weighted sum of the total virtual work $\delta H = \delta H^{\text{FE}} + \delta H^{\text{DE}}$, with

$$\delta H^{\text{FE}} = \sum_{e=1}^{N_e} \int_{\Omega_e^{\text{FE}}} (1-w) \left\{ \rho c_p \frac{\partial T}{\partial t} + k_{cond} \nabla^2 T \right\} \delta T^{\text{FE}} \mathrm{d}V. \tag{5.86}$$

The above equation is the virtual heat equation for the finite element analysis of heat transfer. It relates the virtual heat done by external flux to the temperature distribution within the continuum. Subsequently, the virtual heat done by external flux to the temperature distribution within a collection of discrete particles is related to

$$\delta H^{\text{DE}} = \sum_{\alpha=1}^{N_p} \left[w_\alpha \rho_\alpha c_{p,\alpha} \frac{\mathrm{d}T_\alpha}{\mathrm{d}t} + \sum_{\beta=1}^{n_\alpha} w_{\alpha\beta} k_\alpha (T_\beta - T_\alpha) \frac{a_{\alpha\beta}}{l_{\alpha\beta}} \right] \cdot \delta T_\alpha. \tag{5.87}$$

We require the difference between the FEM and DEM temperature in the last time step, $\theta^{\text{FE}} = \mathrm{T} \mid_t - \mathrm{T} \mid_{t-dt}$ and $\theta^{\text{DE}} = \dot{\theta}^{\text{DE}} \mathrm{d}t$ to be vanishingly small. The homogenization operation including coarse-graining that maps any physical variables between the discrete particles and finite elements will be introduced later in Section. 5.3.2. To enforce the constraint on thermal in the overlapping domain Ω^{C}, we penalize the rate of temperature at the macroscopic scale. This gives rise to an additional term in the virtual work equation, $\delta H = \delta H^{\text{FE}} + \delta H^{\text{DE}} + \delta C^T$, with

$$
\begin{aligned}
\delta C^T \quad &= \epsilon^T \int_{\Omega^{\text{C}}} (\theta^{\text{DE}} - \theta^{\text{FE}}) \cdot (\delta \mathrm{T}^{\text{DE}} - \delta \mathrm{T}^{\text{FE}}) \mathrm{d}V \\
&= \underbrace{\epsilon^T \int_{\Omega^{\text{C}}} (\theta^{\text{DE}} - \theta^{,\text{FE}}) \cdot \delta \mathrm{T}^{\text{DE}} \mathrm{d}V}_{:=\delta C^{T,\text{DE}}} + \underbrace{\epsilon^T \int_{\Omega^{\text{C}}} (\theta^{\text{FE}} - \theta^{\text{DE}}) \cdot \delta \mathrm{T}^{\text{FE}} \mathrm{d}V}_{:=\delta C^{T,\text{FE}}} = 0,
\end{aligned}
\tag{5.88}
$$

where ϵ^T is the thermal penalty parameter $[\frac{W}{mK}][\frac{1}{m^2}]$, which must be strictly positive in the overlapping domain to avoid the singular values. Substituting $\theta^{\text{FE}} = \sum_{j=1}^N \theta_j^{\text{FE}} \psi_j$, $\theta^{\text{DE}} = \sum_{j=1}^N \theta_j^{\text{DE}} \psi_j$, $\delta \mathbf{T}^{\text{FE}} = \sum_{i=1}^N \delta \mathbf{T}_i^{\text{FE}} \psi_i$, and $\delta T^{\text{DE}} = \sum_{i=1}^N (\sum_{\alpha=1}^{N_p} \Pi_{i\alpha} \delta T_\alpha^{\text{DE}}) \psi_i$, the discretized forms of δC^T become:

$$
\begin{aligned}
\delta C^{T,\text{FE}} \quad &= \int_{\Omega^{T,\text{C}}} \epsilon^T \underbrace{(\theta^{\text{FE}} - \theta^{\text{DE}})}_{:=-\mathbf{b}^{T,\text{C}}} \cdot \delta T^{FE} \mathrm{d}V \\
&= \sum_{i=1}^N \epsilon^T \underbrace{\sum_{j=1}^N \int_{\Omega^{T,\text{C}}} \psi_i \psi_j \mathrm{d}V (\theta^{\text{FE}} - \theta^{\text{DE}}) \cdot \delta T_i^{\text{FE}}}_{:=-\mathbf{f}_i^{T,\text{C}}}.
\end{aligned}
\tag{5.89}
$$

$$
\begin{aligned}
\delta C^{T,\text{DE}} \quad &= \int_{\Omega^{T,\text{C}}} \epsilon^T (\theta^{\text{DE}} - \theta^{\text{FE}}) \cdot \delta T^{\text{DE}} \mathrm{d}V \\
&= \sum_{\alpha=1}^{N_p} \underbrace{\sum_{i=1}^N \sum_{j=1}^N \epsilon^T \int_{\Omega^{\text{C}}} \psi_i \psi_j \mathrm{d}V (\theta^{\text{DE}} - \theta^{\text{FE}}) \Pi_{j\alpha} \cdot \delta T_\alpha^{\text{DE}}}_{:=-\mathbf{f}_\alpha^{T,\text{C}}}.
\end{aligned}
\tag{5.90}
$$

Substituting Eq. (5.89) and Eq. (5.90) into the virtual work equation $\delta H = \delta H^{\text{FE}} + \delta H^{\text{DE}} + \delta C^T$ yields

$$
\begin{aligned}
\delta H = & \sum_{e=1}^{N_e} \int_{\Omega_e^{\text{FE}}} (1-w) \left\{ \rho c_p \frac{\partial T}{\partial t} + k_{cond} \nabla^2 T + \frac{1}{1-w} \mathbf{b}^{T,C} \right\} \delta T^{\text{FE}} \mathrm{d}V \\
& + \sum_{\alpha=1}^{N_p} \left[w_\alpha \rho_\alpha c_{p,\alpha} \frac{\mathrm{d}T_\alpha}{\mathrm{d}t} + \sum_{\beta=1}^{n_\alpha} w_{\alpha\beta} k_\alpha (T_\beta - T_\alpha) \frac{a_{\alpha\beta}}{l_{\alpha\beta}} - \mathbf{f}_\alpha^{T,C} \right] \cdot \delta T_\alpha^{\text{DE}}.
\end{aligned}
\tag{5.91}
$$

5.3.2. COARSE-GRAINING FOR HOMOGENIZATION

The coupling terms in Section. 5.3.1 requires defining the homogenized physical variables from the discrete particles to the finite elements. Here we introduce coarse-graining (CG), a local smoothing technique that defines continuum fields (ρ, $\vec{v}$, σ, q), locally satisfying conservation laws [27]. For instance, the coarse-grained density may be defined as

$$
\rho(\vec{x}) = \rho_m \circ \mathcal{W} = \sum_{\alpha=1}^{N} m_\alpha \mathcal{W} (\vec{x} - \vec{x}_\alpha),
\tag{5.92}
$$

Where m_α is the mass of particle α, $\vec{x}_\alpha$ is the particle position, and $\mathcal{W}$ is a spatial smoothing kernel, which in $n-$ dimensional space

- is normalized: $\int_{\mathbb{R}}^n \mathcal{W}(\mathbf{x}) \mathrm{d}\mathbf{x} = 1$,

- is non-negative: $\mathcal{W}(\mathbf{x}) \geq 0$ for all $\mathbf{x} \in \mathbb{R}^n$

- has compact support: $\exists c \in \mathbb{R} : \mathcal{W}(\mathbf{x}) = 0$ for all $|\mathbf{x}| > c$

Two typical CG functions are the cut-off Gaussian and the Lucy polynomial [19]

$$
\begin{aligned}
\mathcal{W}^G(\mathbf{x}) &= \begin{cases} C^G \exp\left(-\frac{|\mathbf{x}|^2}{2(c/3)^2}\right) & \text{if } |\mathbf{x}| < c, \\ 0 & \text{else}, \end{cases} \\
\mathcal{W}^L(\mathbf{x}) &= \begin{cases} C^L \left(-3(|\mathbf{x}|/c)^4 + 8(|\mathbf{x}|/c)^3 - 6(|\mathbf{x}|/c)^2 + 1\right) & \text{if } |\mathbf{x}| < c, \\ 0 & \text{else}, \end{cases}
\end{aligned}
\tag{5.93}
$$

where C^G and C^L are the appropriate factors for normalization. Note, for spherical particles, $\mathcal{W}$ is isotropic in space in c is the only parameter that controls the support of the CG field.

Fig. 5.4 illustrates the particle density and stress fields extracted using CG.

CG is used to homogenize both the displacement field and the temperature field from discrete particle computations presented in Eq. (5.80) and Eq. (5.88). To this end, the particle velocity field and particle rate of the temperature field can be written in terms of their homogenization operator, namely
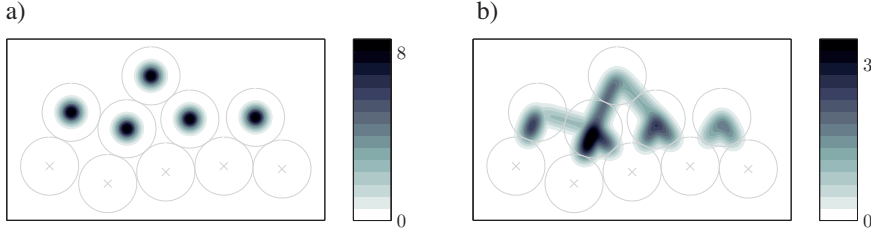
Figure 5.4: a) Coarse-grained density field b) Coarse-grained stress field [27].

$$
\mathbf{v}_i^{\mathrm{DE}} = \sum_{\alpha=1}^{N_p} \Pi_{i\alpha} \mathbf{v}_\alpha, \text{ where }
\begin{cases}
\Pi_{i\alpha} = \dfrac{m_\alpha \psi_i(\mathbf{x})}{\sum\limits_{\alpha=1}^{N_p} m_\alpha \psi_i(\mathbf{x})} & \text{for } c = 0 \\[2ex]
\Pi_{i\alpha} = \dfrac{\int_{\Omega_e} m_\alpha \mathcal{W}(\mathbf{x}-\mathbf{x}_\alpha)\psi_i(\mathbf{x})\mathrm{d}\mathbf{x}}{\sum\limits_{\alpha=1}^{N_p} \int_\Omega m_\alpha \mathcal{W}(\mathbf{x}-\mathbf{x}_\alpha)\psi_i(\mathbf{x})\mathrm{d}\mathbf{x}} & \text{for } c > 1.
\end{cases}
\tag{5.94}
$$

and,

$$
\dot{\theta}_i^{\mathrm{DE}} = \sum_{\alpha=1}^{N_p} \widetilde{\Pi}_{i\alpha} \dot{\theta}_\alpha, \text{ where }
\begin{cases}
\widetilde{\Pi}_{i\alpha} = \dfrac{m_\alpha c_{p,\alpha} \psi_i(\mathbf{x})}{\sum\limits_{\alpha=1}^{N_p} m_\alpha c_{p,\alpha} \psi_i(\mathbf{x})} & \text{for } c = 0 \\[2ex]
\widetilde{\Pi}_{i\alpha} = \dfrac{\int_{\Omega_e} m_\alpha c_{p,\alpha} \mathcal{W}(\mathbf{x}-\mathbf{x}_\alpha)\psi_i(\mathbf{x})\mathrm{d}\mathbf{x}}{\sum\limits_{\alpha=1}^{N_p} \int_\Omega m_\alpha c_{p,\alpha} \mathcal{W}(\mathbf{x}-\mathbf{x}_\alpha)\psi_i(\mathbf{x})\mathrm{d}\mathbf{x}} & \text{for } c > 1.
\end{cases}
\tag{5.95}
$$

where $\Pi_{i,\alpha}$ and $\widetilde{\Pi}_{i,\alpha}$ are the homogenisation operators for the velocity and rate of temperature fields. Note, when c_p the specific heat capacity is constant for all particles, $\Pi_{i,\alpha} = \widetilde{\Pi}_{i,\alpha}$. ψ_i are the finite element basis functions. We make use of this simplification in the following for the implementation of the coupled code.

5.3.3. THE COUPLING ALGORITHM

The thermo-mechanical volume coupling implementation requires four governing equations to be weighted in the dynamically adapted coupling zone. Therefore, both the finite element and discrete particle classes, in oomph-lib [20] and MercuryDPM [19], respectively, are extended with member functions to evaluate the local coupling weights similarly as developed previously by Cheng *et al.* [21] at the integration points, particle positions, and contact points. The weighting function is assumed to be in the FEM shape function space (and thus moves if the thermo-elastic body deforms); thus we first set its nodal values and then interpolate for a given location, using the FEM basis functions $w(\mathbf{X}) = \sum_{i=1}^{N} w_i \psi_i(\mathbf{X})$. The implementation is depicted in Fig. 5.5.

The algorithm presented in Fig. 5.5 contains the following steps:

- At each time step, the hierarchical grid detection method of MercuryDPM [19] is employed to determine whether an Element overlaps with the discrete particles.
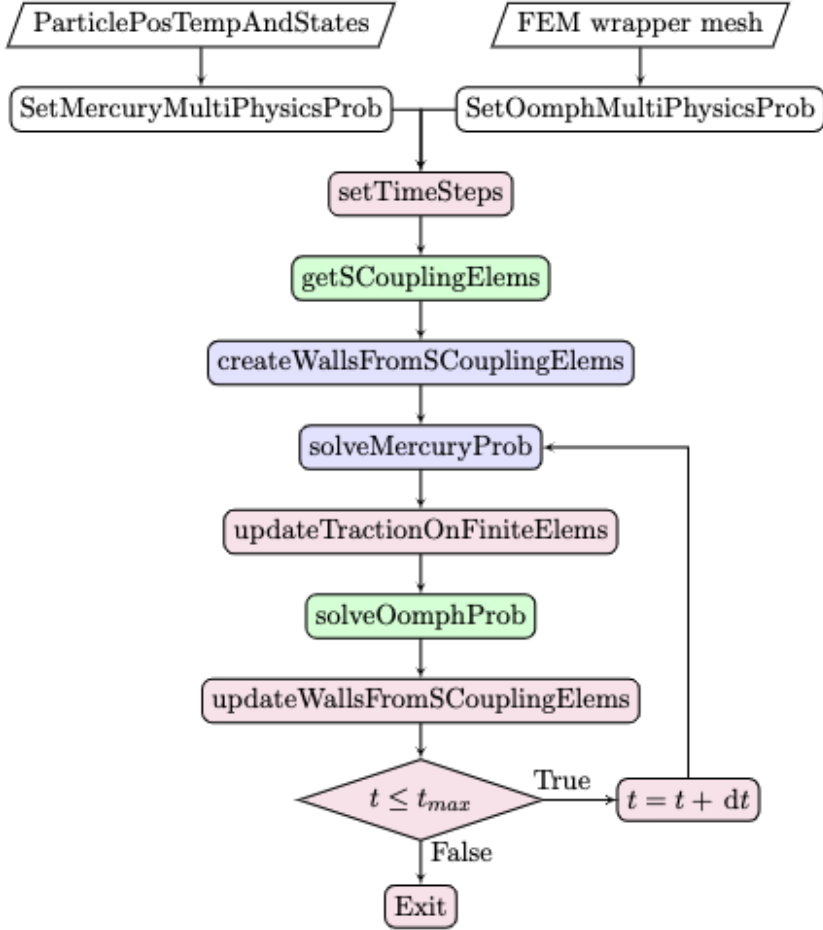
Figure 5.5: Implementation of FEM-DEM thermo mechanical volume coupling in the MercuryDPM and oomph-lib codes [21].

- During the homogenization process, which involves transferring the continuum velocity and temperature fields from discrete particles to elements (described by Eq. (5.94)), the local coordinates of particle positions in the coupled element are obtained. This transformation is achieved using the FEM basis functions.

- The boundary conditions, coupling forces, and fluxes are updated based on the revised velocity, positions, and temperature fields in the discrete and solid subdomains, handled respectively by MercuryDPM and oomph-lib.

- The simulation iterates through these steps until the condition $t \leq t_{max}$ is no longer true.

5.4. RESULTS AND DISCUSSION

In this section, we first analyse the unsteady heat transfer problem in discrete and solid media using MercuryDPM and oomph-lib, respectively. It verifies that the implemented coupling approach works properly for each physics. Then, the coupling implementation using both software is also verified for the unsteady heat problem along with the conservation of thermal energy within the system. To verify the accuracy of the thermo-mechanical description in the solid medium, mechanical tests are conducted and validated against analytical solutions. Finally, a multi-scale framework is presented to demonstrate the capabilities of the present implementation to address multi-physics scenarios such as the laser sintering process.

5.4.1. UNSTEADY HEAT TRANSFER

To verify the unsteady heat transfer problem in the discrete and solid media, and compare it against the analytical solution described in Appendix 5.7.1, we evaluate the domain illustrated in Fig. 5.6.
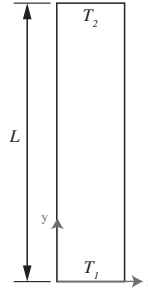
Figure 5.6: Domain of length L to be evaluated using Eq. (5.107). T_1 and T_2 are the temperatures at the bottom and top surfaces, respectively. We make the assumption that there is no internal heat generation $H = 0$, and no heat flux or heat transfer occurring across the boundaries of the volume V.

The material and boundary conditions are listed in Table 5.1.

Table 5.1: Material DEM properties, dimension and boundary conditions.

property	units	value
ρ^{DEM}	[kg/m^3]	1200
k_{cond}^{DEM}	[kg/m^3]	1.9×10^7
c_p^{DEM}	[J/Kg K]	2000
L	[m]	0.025
$T\|_{t=0} = T_0 \ \forall \ 0 < y < L$	[°C]	2.5
$T\|_{y=0} = T_1 \ \forall \ t > 0$	[°C]	2.5
$T\|_{y=L} = T_2 \ \forall \ t > 0$	[°C]	400

First, the discrete element simulation is performed using MercuryDPM. For this, a 3D elastoplastic beam [2] composed of 800 mono-size particles of radius $R = 25.0 \times 10^{-4}$ m

is built, where the particles are arranged in a $4 \times 4 \times 50$ grid such that the particles overlap by $0.001R$. It has a volume fraction of about 64%. The simulation neglects the effects of gravity and friction, while the contact properties are listed in Table 5.2.

Table 5.2: Contact properties.

Property, symbol	units	Value
Loading stiffness, k_1	[N/m]	$\beta E R$
Unloading stiffness, k_2	[N/m]	$10k_1$
Cohesion stiffness, k_c	[N/m]	k_1
Penetration depth, ϕ	[-]	0.01

The magnitude of stiffness k_1 is chosen based on the macro-micro relation $k_1 = \beta E R$ [28], where $\beta = 0.1$ and $E = 1.0$ GPA are used in our work. We neglect heat radiation and convection and only consider heat conduction through the particle-particle contacts. Fig. 5.7 shows the results of the diffusion process at different times t, along the $y-$ direction.
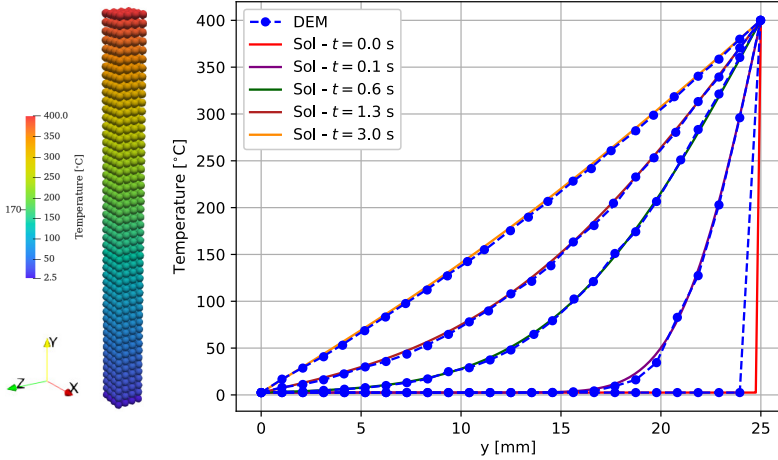

Figure 5.7: Left) Discrete domain. Right) Temperature distribution in the discrete domain at different times during the heat transfer. We assume that there is no internal heat generation $H = 0$, and no heat flux or heat transfer occurring across the boundaries of the volume V. Dotted lines represent the simulation and solid lines represent the analytical solution.

Fig. 5.7 shows the simulation results of the diffusion, starting from the initial temperature of T_0, prescribed to all nodes at $t = 0$ s, except for the particles located at the top surface. As time progresses, the heat diffuses through the particles until it reaches a steady-state condition at $t = 3.0$ s. The comparison between the DEM simulation and the analytical solution (derived in Appendix 5.7.1) shows good agreement, with less than 1% error in the calculation of the transient problem. The DEM simulation using MercuryDPM is

thus well suited to modelling the unsteady heat transfer problem.

Subsequently, a solid beam is simulated using oomph-lib, where dissipative effects and thermal expansion are not considered, (see Eq. 5.66, $W_D = 0$), similar to the DEM model. The solid beam employs a total of 4 elements in the $x-$ and $z-$ directions, and 30 elements in the $y-$ direction, utilizing an elastic cubic mesh with 8 nodes per element. The constitutive relation of the beam is represented by the generalized Hooke's law, and Poisson's effect is not considered. In order to calibrate density, heat capacity, and thermal conductivity in the FEM simulations, we assume DEM heat conduction description without heat source (see Eq. (5.85)):

$$\rho_\alpha c_{p,\alpha} \frac{dT_\alpha}{dt} + \sum_{\beta=1}^{n_\alpha} k_{cond,\alpha}(T_\beta - T_\alpha)\frac{a_{\alpha\beta}}{l_{\alpha\beta}} = 0, \tag{5.96}$$

with contact area $a_{ij} = \sqrt{R_{ij}\delta_{ij}}$, $l_{ij} = 2R - \delta$. For $1D$ chain constant $a_{ij} = a$, $L_{ij} = L$, $m = \rho V$, particle volume V_p

$$\rho V_p c_p \frac{dT_\alpha}{dt} + a k_{cond}\left(\frac{T_{i+1} - T_i}{L} - \frac{T_i - T_{i-1}}{L}\right) = 0. \tag{5.97}$$

Now, the FEM heat conduction equation in $1D$ without a heat source:

$$\rho^{FE} c_p^{FE}\frac{\partial T^{FE}}{\partial t} + \frac{\partial}{\partial x}\left(k_{cond}^{FE}\frac{\partial T^{FE}}{\partial x}\right) = 0. \tag{5.98}$$

Using Finite differences and considering mesh size L, is possible to approximate spatial and temporal derivatives in the heat conduction equation. This numerically solves the equation on a discrete mesh and calculates how temperature evolves over time and space.

$$\rho^{FE} c_p^{FE}\frac{\partial T_i^{FE}}{\partial t} + \frac{k_{cond}^{FE}}{L}\left(\frac{T_{i+1} - T_i}{L} - \frac{T_i - T_{i-1}}{L}\right). \tag{5.99}$$

Using volume fraction $v = V_p/L^3$, we get

$$\rho^{FE} = v\rho^{DE} = \frac{V_p}{L^3}\rho^{DE}. \tag{5.100}$$

Assuming same heat capacity per L^3 volume element,

$$\rho^{DE} V_p c_p T_i = \rho^{FE} c_p^{FE} T_i L^3 \tag{5.101}$$

$$c_p^{FE} = c_p^{DE}, \tag{5.102}$$

then, comparing Eq. (5.96) and Eq. (5.98) we have

$$k_{cond}^{FE} = k_{cond}\frac{a}{L^2} \tag{5.103}$$

Fig. 5.8 illustrates the diffusion in the solid beam at different times along the $y-$ direction.
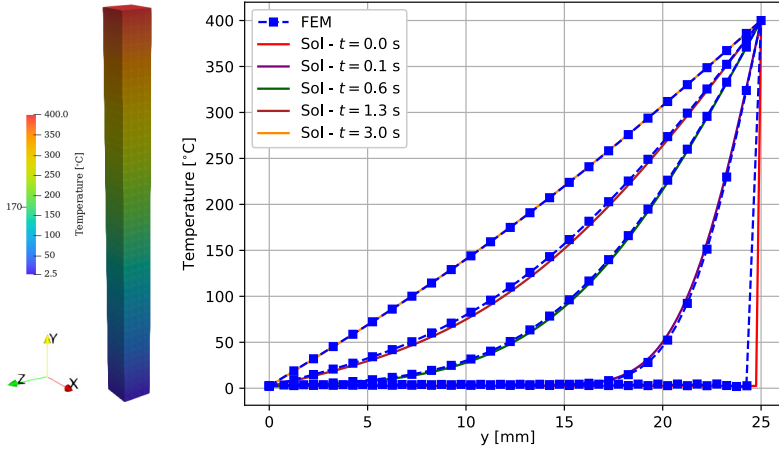
Figure 5.8: Left) Solid domain. Right) Temperature distribution in the solid domain at different times during the heat transfer. We assume that there is no internal heat generation $H = 0$, and no heat flux or heat transfer occurring across the boundaries of the volume V. Dotted lines represent the simulation and solid lines represent the analytical solution.

As seen in Fig. 5.8, the unsteady heat transfer problem using FEM is also consistent with the analytical solution presented in Appendix 5.7.1. As the heat is transferred through the solid elements, the temperature reaches a steady state at $t = 3$ s. It validates the FEM implementation using oomph-lib to model unsteady heat transfer by conduction.

Subsequently, the coupled simulation between DEM and FEM is performed to verify the difussion through the media. The length of the domain is divided by the solid and discrete media, where one discrete particle per element is set inside a finite solid element. Table 5.3 lists the penalties and coarse-grained width for the simulation.

Table 5.3: Coupling properties.

Property, symbol	units	Value
Thermal penalty, ϵ^T	[W/m^3 K]	2×10^{-1}
Mechanical penalty, ϵ	[Pa/m^2]	1×10^{-2}
Tolerance, tol	[-]	1×10^{-8}
Coarse-grained width, $CG\ w$	[m]	$0.5R$

Fig. 5.9 shows the temperature evolution in the coupled domain at different times along the $y-$ axis.

The agreement of heat transfer between both media, DEM and FEM, is satisfactory, with less than 1% error compared to the analytical solution as depicted in Fig. 5.9. It verifies the diffusion between both domains and the continuity of temperature fields.
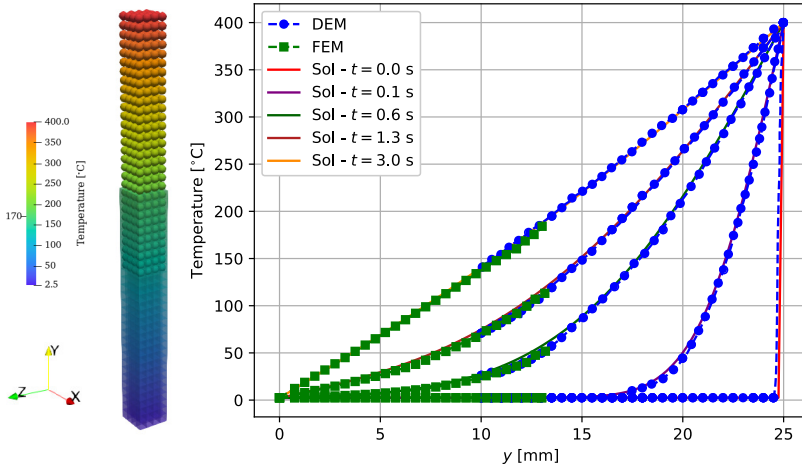
Figure 5.9: Left) Coupled domain. Right) Temperature distribution in the coupled domain at different times during the heat transfer. We assume that there is no internal heat generation $H = 0$, and no heat flux or heat transfer occurring across the boundaries of the volume V. Dotted lines represent the simulation and solid lines represent the analytical solution.

5.4.2. CONSERVATION OF THERMAL ENERGY

By maintaining the discrete and solid media at different temperatures and waiting until the thermal equilibrium is reached, the conservation of thermal energy (neglecting convection and radiation) is tested in the coupling implementation. For this test, the temperature is set to 120 °C for all discrete particles, while the solid elements are set to 100 °C, see Fig. 5.10. The DEM and FEM simulation properties are set similarly to the unsteady heat transfer problem discussed previously in Section 5.4.1.
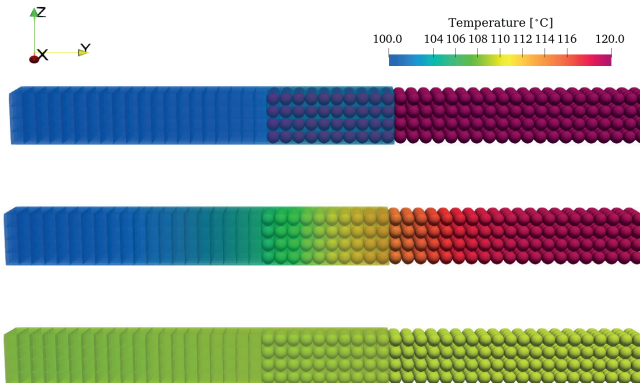

Figure 5.10: Discrete and solid media coupled and set to different temperatures. We assume no internal heat generation $H = 0$, and no heat flux or heat transfer occurring across the boundaries of the volume V. The colour bar represents the temperature.

As time progresses, the heat is transferred through the coupled medium, increasing the temperature of the solid elements, and decreasing the temperature of the discrete particles until reaching approximately an average value. The temperature evolution over time is visualized in Fig. 5.11
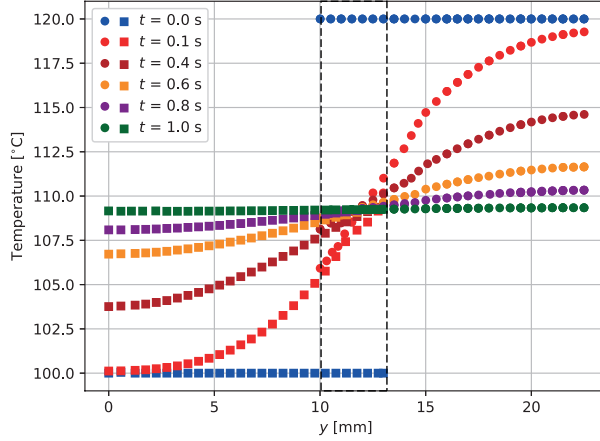

Figure 5.11: Conservation of thermal energy within the coupled domain. Temperature is measured along the $y-$ axis. Circles represent the discrete elements, squares represent the solid elements. The dashed area indicates the coupling zone.

As visualised in Fig 5.11, the coupled system reaches a final temperature of 109.3 °C, which represents an error of less than 1%. Ideally, the final temperature of the coupled domain should be 110 °C. This error can be attributed to the homogenization of material properties between DEM and FEM. In this case. Coarse-graining [22] can be employed to extract continuum quantities precisely, and future studies may be conducted to address a refined calibration of the models.

The results of heat transfer and thermal energy demonstrate that the coupling implementation describes the diffusion between the granular and solid media. It extends the coupling framework previously developed by Cheng *et al.* [21] for mechanical problems. The authors validated the mechanical coupling approach through various analytical solutions, and thus the present study continues to focus on the thermo-mechanical effects, specifically using oomph-lib, where the capabilities of the FEM framework are analysed to address thermo-viscoelasticity.

5.4.3. THERMAL DEFLECTION

To verify the thermal deflection in a solid medium, an isotropic cantilever beam problem is defined. Table 5.4 lists the parameters and boundary conditions used in the oomph-lib simulation.
The number of elements for the FEM analysis is set to 4 in $x-$ and $z-$ directions, and 50 elements in $y-$ direction. The constitutive relation of the beam is described by the

Table 5.4: Parameters for simulation

Parameter	Units	Value
Length - l_y	[m]	25.0
Height - l_z	[m]	0.5
Width - l_x	[m]	0.5
Flexural rigidity - M/EI	[N/m^2]	1.0×10^{-38}
Conductivity - β	[W/mK]	1.0
Thermal expansion - α	[1/°C]	$0.0 - 7.1 \times 10^{-3}$
Gravity - g	[m/s^2]	0.0
$T\vert_{t=0} = T_0$	[°C]	0.0
$T\vert_{z=l_y} = T_1 \ \forall \ t > 0$	[°C]	1.0
$T\vert_{z=0} = T_2 \ \forall \ t > 0$	[°C]	0.0

generalized Hooke's law, and the Poisson effect is neglected. This corresponds to a steady heat transfer problem, for which is assumed that the thermal equilibrium is reached once the simulation starts. Two temperatures, $T_1 = 1.0$ °C and $T_2 = 0.0$ °C, are set to the top ($z = l_z$) and bottom ($z = 0$) surfaces of the domain, respectively. The beam is fully constrained at $l_x = 0$. Fig. 5.12 shows the cantilever beam and the thermal deflection.

Temperature [°C]
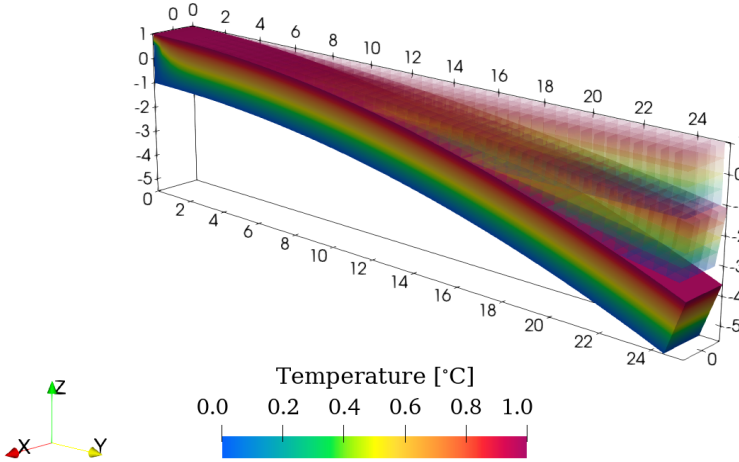
Figure 5.12: Thermal deflection of a cantilever beam. The beam of length l_y is fully constrained at $x = 0$. We assume no internal heat generation $H = 0$, and no heat flux or heat transfer occurring across the boundaries of the volume V.

Fig. 5.12 shows the cantilever beam deflecting. The displacement results for the nodes along the $-y$ axis, located at $z = l_z/2$, with different thermal expansion coefficients α, are presented in Fig. 5.13.

The cantilever beam deflects higher according to the increment of its thermal

Figure 5.13: Deflection results of the nodal points along the $y-$ axis, located at $z = l_z/2$ in the cantilever beam. the crossed lines represent the FEM simulation and the solid lines represent the analytical approximation. Different thermal expansion coefficients α are tested.
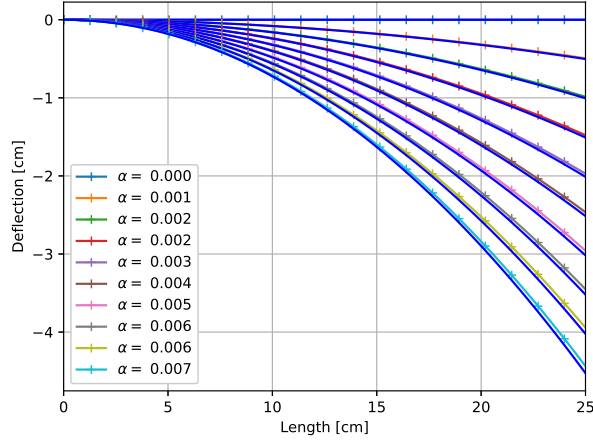
expansion, as visualized in Fig. 5.13, which describes the effect of temperature in the body. Comparing the simulation against the analytical solution developed in Appendix 5.7.2, the FEM simulations present good accuracy.

5.4.4. VIBRATION OF A CANTILEVER BEAM

In order to verify the accuracy of the FEM model to describe thermo-viscoelastic problems, the vibration of a cantilever beam is analysed. As a single analytical solution for the thermo-mechanical problem is not trivial, several tests are designed to validate the problem separately, verifying the contribution of each term in Eq. (5.66). Fig. 5.14 illustrates the cantilever beam.
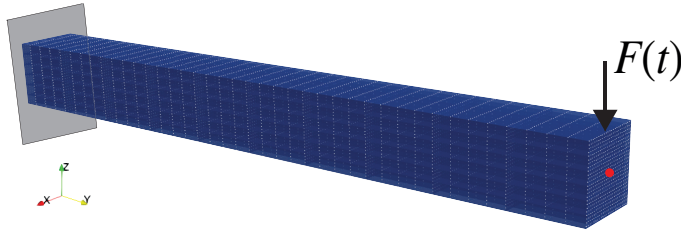
Figure 5.14: Cantilever beam of length L_y, height L_z, width L_x, and square cross section. F represents the axial force applied at the free end at $t = 0$ s. The red point represents the measuring points.

The cantilever beam is fully constrained at $L_y = 0$, and an axial force f is located at the free end as indicated in Fig. 5.14. This force disrupts the equilibrium at $t = 0$ s. The model properties are listed in Table 5.5.

Table 5.5: Model parameters for simulation.

Parameter	Units	Value
Length - L_y	[m]	1.25×10^{-2}
Height - L_z	[m]	1.0×10^{-3}
Width - L_x	[m]	1.0×10^{-3}
Inertia - I	[Kg/m^2]	$(1.0/12.0) * W^4$
Young's modulus - E	[Pa]	1.0×10^{13}
Density - ρ	[kg/m^3]	5.0×10^7
Simulation time - t_{max}	[s]	50
Gravity - g	[m/s^2]	0.0
Force - F	[N]	3.5×10^5
Dissipation - μ	[N s/m]	5.0×10^{-5}
Conductivity - β	[W/mK]	1.0×10^4
Thermal expansion - α	[1/°C]	1.0

The solid beam contains a total of 2 finite elements in the $x-$ and $z-$ directions, and 25 finite elements in the $y-$ direction, utilizing an elastic cubic mesh with 8 nodes per element. The constitutive relation of the beam is represented by the generalized Hooke's law, and Poisson's effect is not considered.

DYNAMIC ELASTIC RESPONSE

The elastic response of the cantilever beam is simulated, considering the elastic W_E and inertia W_I terms in Eq. (5.66). The illustration of the oomph-lib simulation is depicted in Fig. 5.15.
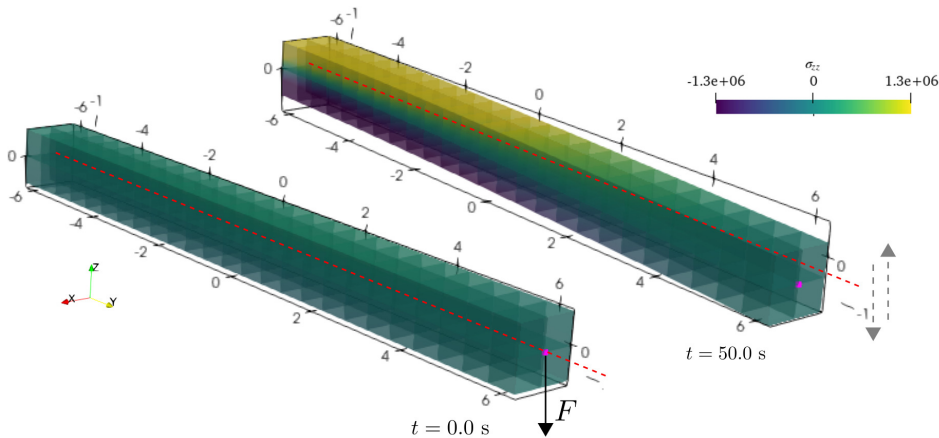

Figure 5.15: Dynamic elastic response of the cantilever beam. F represents the applied force at $t = 0$ s, the dot located at the free surface represents the measured point, and the colour bar the stress along the beam.

As the cantilever beam vibrates due to the perturbation F at $t = 0$ s, the nodal

displacement of the point located at the centre of the free surface is measured. The result of the nodal displacement is presented in Fig. 5.16
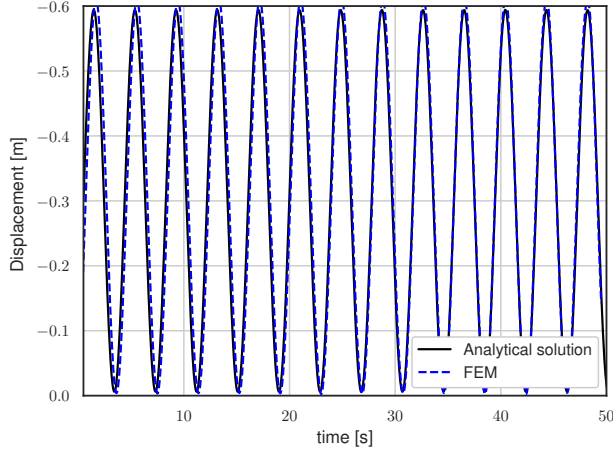

Figure 5.16: Displacement of the node located at the free surface of the cantilever beam. The dashed line represents the simulation, and the solid line represents the analytical solution.

The nodal displacement of the end of the cantilever beam is tracked during the simulation, which describes a harmonic oscillation typically observed in fully elastic systems. As visualised in Fig. 5.16 both the amplitude and period agree with the analytical solution developed in Appendix 5.7.3.

DYNAMIC THERMO-ELASTIC RESPONSE

The thermo-elastic response of the cantilever beam, depicted in Fig. 5.14 is simulated, considering the elastic W_E, inertia W_I, conductivity W_K, and thermal capacity W_{KT} terms in Eq. (5.66). It is assumed that the thermal equilibrium of the beam is reached instantaneously, once the simulation starts $t = 0$ s, We assume no internal heat generation $H = 0$, and any flux through the boundaries is neglected $q_n = 0$. The temperature on the surfaces of the beam is set to $T = 273.0$ K, at $t = 0$ s. Fig. 5.17 illustrates the oomph-lib simulation.

As the cantilever beam vibrates due to the perturbation F at $t = 0$ s, the nodal displacement of the point located at the centre of the free surface is measured for five thermal gradients ranging from $\Delta T = 0$ K to $\Delta T = 250.0$ K. The nodal displacement results are depicted in Fig. 5.18.

The results indicate that the amplitude of the oscillation of the nodal displacement at the measuring point located at the end of the cantilever beam is affected linearly as the temperature difference ΔT increases, see Fig. 5.18. This is because the thermal expansion of the material leads to changes in the mechanical properties of the beam, affecting its response to the applied load. The frequency of oscillation remains the same
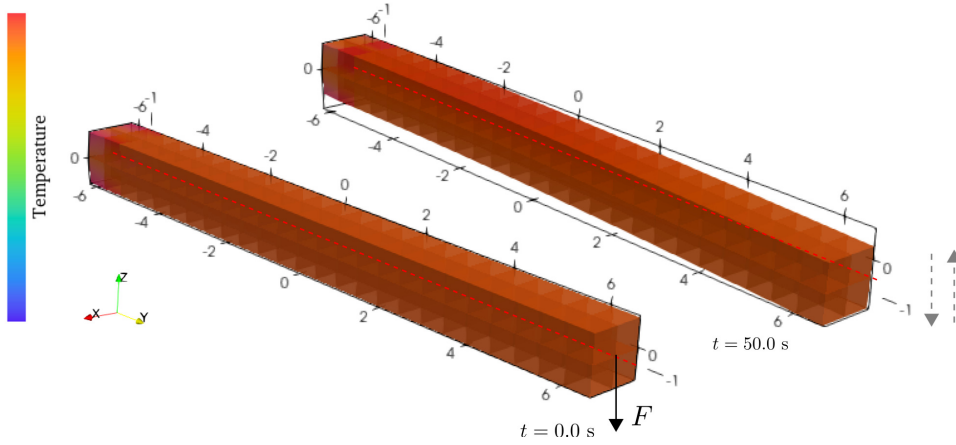
Figure 5.17: Dynamic thermo-elastic response of the cantilever beam. F represents the applied force at $t = 0$ s, the dot located at the free surface represents the measured point, and the colour bar the temperature along the beam.

Figure 5.18: Displacement of the node located at the free surface of the cantilever beam. The dashed lines represent the simulation according to different gradients of temperature. The blue dashed curve represents the FEM simulation at $\Delta T = 0\ K$.

for all curves, as it is primarily determined by the material properties and geometry of the beam.

DYNAMIC ELASTIC AND DISSIPATIVE RESPONSE

The elastic and dissipative response of the cantilever beam is simulated, considering the elastic W_E inertia W_I, and dissipation W_D terms in Eq. (5.66). The results of the nodal

displacement located at the free surface of the cantilever beam are depicted in Fig. 5.19

Figure 5.19: Displacement of the node located at the free surface of the cantilever beam. The dashed line represents the simulation, and the solid line represents the analytical solution.

As the cantilever beam vibrates due to the perturbation F at $t = 0$ s, the nodal displacement of the point located at the centre of the free surface is measured. The nodal behaviour describes a harmonic oscillation, decreasing over time, typically observed in elastic bodies under frictional forces, with dissipation μ. As visualised in Fig. 5.16 both the amplitude and period agree with the analytical solution developed in Appendix 5.7.4.

DYNAMIC THERMO-ELASTIC AND DISSIPATIVE RESPONSE

The thermo-elastic and dissipative response of the cantilever beam is simulated, considering the elastic W_E inertia W_I, dissipation W_D, conductivity W_K and thermal capacity W_{KT} terms in Eq. (5.66). It is assumed that the thermal equilibrium of the beam is reached instantaneously, once the simulation starts $t = 0$ s, we assume no internal heat generation $H = 0$, and any flux through the boundaries is neglected $q_n = 0$. The temperature on the surfaces of the beam is set to $T = 100.0$ °C. The results of the nodal displacement located at the free surface of the cantilever beam are depicted in Fig. 5.20

The simulation results demonstrate that the measuring point, located at the free surface of the cantilever beam, oscillates with higher amplitude as the temperature increases. The displacement of the cantilever, considering dissipation μ, is also affected by temperature, leading to an over-damping compared to the mechanical test where $\Delta T = 0$. in addition, an increase in temperature can cause an increase in the damping coefficient of the beam, which may lead to faster dissipation of energy as visualized in Fig. 5.20. This behaviour is consistent with the expectations of thermo-mechanical
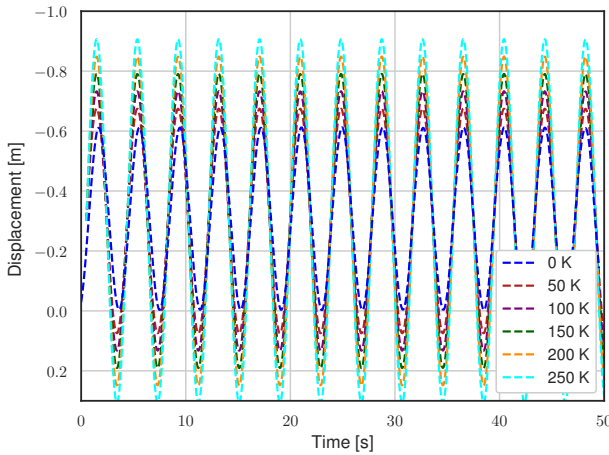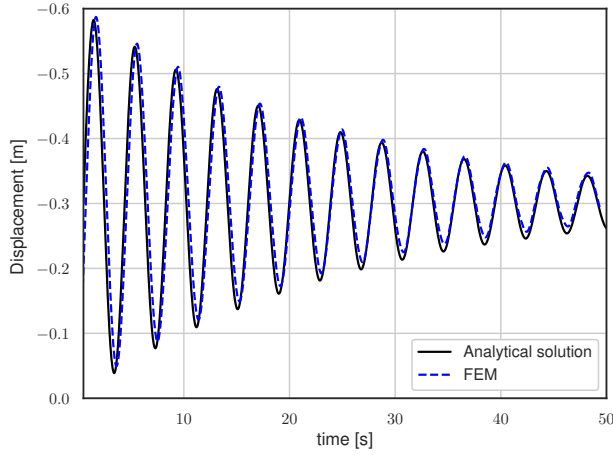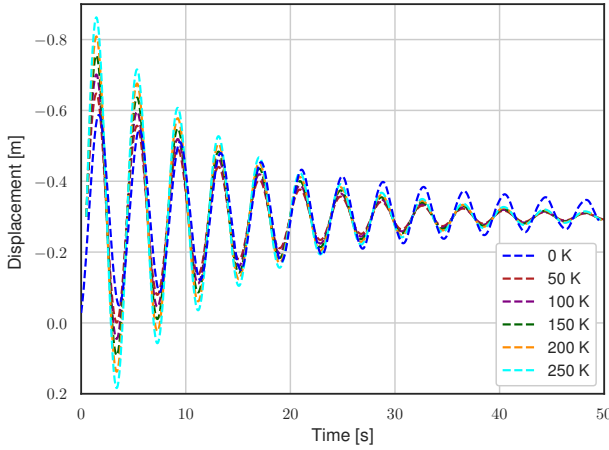
Figure 5.20: Displacement of the node located at the free surface of the cantilever beam. The dashed line represents the simulation according to different gradients of temperature. The blue dashed curve represents the FEM simulation at $\Delta T = 0\,K$.

systems, where temperature-dependent material properties can significantly influence the dynamic response and dissipation characteristics of structures.

5.4.5. MULTI-SCALE SINTERING SIMULATION

The present investigation showcases the capabilities of two open-source software packages, MercuryDPM and oomph-lib, for modelling multi-physics problems and assessing their accuracy when coupled for a multi-scale framework.

One of the specific multi-physics and multi-scale scenarios we explore is laser sintering. This process involves the simultaneous solution of thermal equilibrium and momentum balance equations during the interaction of a laser beam with particulate materials (powders). The length scale at which the laser impacts and sinters individual particles is on the order of micrometres, whereas the collection and behaviour of millions of particles on the working stage occur at the scale of centimetres. Such a wide-ranging scale makes the laser sintering process impractical to model using a single scale itself.

In this context, our coupling framework is designed to capture the micro-scale intricacies of laser sintering while representing the outer domain as a solid using oomph-lib. Figure 5.21 shows the proposed approach.

To simulate laser sintering, we utilize a two-domain system. In the central region, we insert 8800 particles to represent micro-scale resolution. This central domain is surrounded by an outer domain composed of finite elements. The total number of finite elements in the system is 12455, encompassing both the solid and macro-scale aspects of the process. At the interface between these discrete particle domains and the
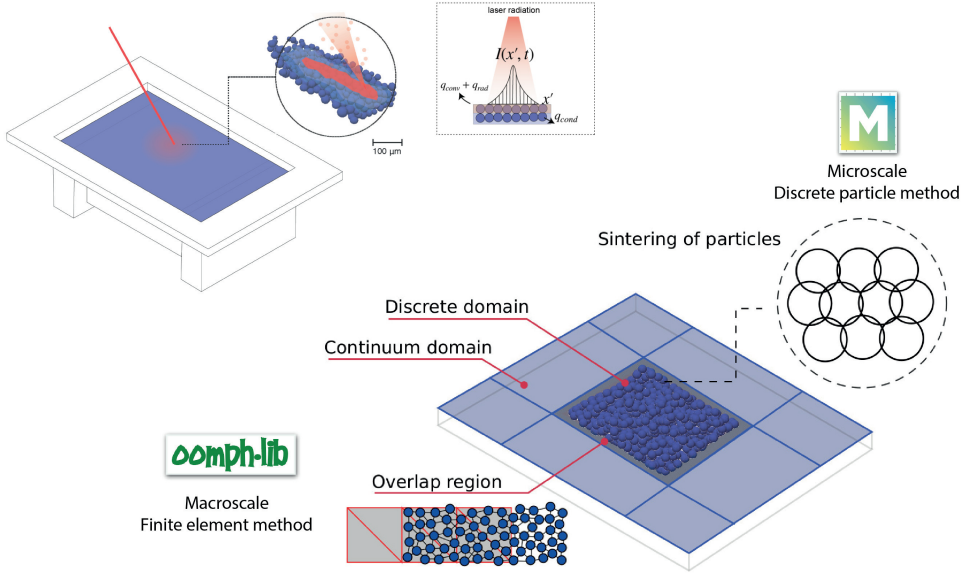
Figure 5.21: Multi-scale framework to simulate the laser sintering process using MercuryDPM and oomph-lib.

solid finite element domain, there are a total of 1500 volume coupling elements. Each coupling element contains a single discrete particle. The dimensions of the domain have been chosen to be representative, based on the average size of PA12 particles, which is approximately 125 μm. For a visual representation of this configuration, see Figure 5.22.
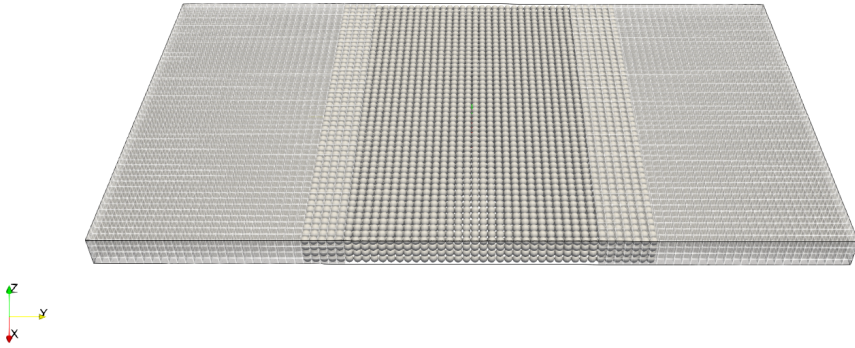
Figure 5.22: Coupled domain to simulate laser sintering. Discrete elements (particles) are modelled using MercuryDPM, finite elements are modelled using oomph-lib. The domains are coupled using volume elements, containing one discrete element per volume.

The material parameters are listed in Table. 5.6

A temperature and pressure-dependent visco-elastic-plastic model [2] is utilized to

Table 5.6: Material properties

Property - symbol	units	value
Radius - R^{DEM}	[μm]	125
Density - ρ^{DEM}	[kg/m^3]	1020
Heat capacity - c_p^{DEM}	[J/kg K]	1200
Thermal conductivity - k_{cond}^{DEM}	[W/mK]	0.240
Thermal convectivity - k_{conv}^{DEM}	[W/mK]	635.73
Emissivity - ϵ^{DEM}	[-]	0.164
Melting point - T_m	[$^\circ$C]	186

describe the interactions, implemented in MercuryDPM [19]. The properties associated with this model are listed in Table 5.7.

Table 5.7: Contact properties.

Property - symbol	units	value
Loading stiffness - k_1	[N/m]	βER
Unloading stiffness - k_2	[N/m]	$10k_1$
Cohesion stiffness - k_c	[N/m]	k_1
Range of melting - T_{var}	[$^\circ$C]	0.1 T_m
Adhesive distance - δ_a,	[m]	0.001
Thermal expansion - δa_T	[K^{-1}]	0.0001

The particles are just at contact, the effect of gravity is neglected, and friction among the particles is not considered. The loading stiffness k_1 is determined based on the macro-micro relationship $k_1 = \beta ER$ [28], where we set $\beta = 0.1$ and $E = 1.0$ GPa in our work. The initial temperature of the system is $T = 150\,^\circ$C. The thermal energy dissipation is only considered in the discrete media since convection and radiation are not implemented in the solid model. Future studies will describe all the modes of heat transfer in oomph-lib.

Regarding the sintering model, our temperature-dependent rheological model for visco-elastic particles is utilized [8]. The model requires the calibration of fluidity C_1 and surface tension γ. Our previous investigation, discussed in Chapter 4, estimated the range of these parameters according to the laser set-up. Table 5.8 lists the parameters.

Table 5.8: Sintering model parameters

Property - symbol	units	value
Fluidity - C_1	[Pa^{-1}s^{-1}]	3.41
Surface tension - γ	[mN/m]	48.56

In Chapter 4, we determined the extent of absorption achievable by particles when irradiated by a laser beam. This analysis involved ray tracing simulations, which provided insights into the level of absorption based on the overlap and energy input. Here, we utilize the same results obtained from the ray tracing simulations, and Table 5.9 summarizes the laser configuration.

Table 5.9: Laser and material properties.

Parameter - symbol	units	value
Laser radius - R_l	μm	15
Irradiated energy - E_{in}	μJ	384
Hatch distance - h_l	μm	250
Pulse duration - t_l	ms	1
Reflectance - R_l	[−]	0.05

In laser sintering and materials processing, the estimation of the scan speed can be computed as:

$$v_l = \frac{h_l}{t_l} \frac{E_{in}}{\pi R_l^2 (1 - R_l)},$$ (5.104)

The scan speed we have computed, approximately 3.85 m/s (as detailed in Table 5.9), is remarkably high compared to the conventional laser operation speed range of $0.01 - 1.0$ m/s. To provide context for this deviation, it's important to note that these values are based on our earlier investigation in Chapter 4, where we characterized the absorption behaviour of PA12 particles under irradiation with an energy level of $E_{in} = 384$ μJ over a pulse duration of $t_l = 1$ ms.

We use Hooke's law for the material constitution of the finite elements, assuming small deformations. We neglect the Poisson's effect and the coefficient of thermal expansion is set to $\alpha = 0.0001$ K^{-1}. Regarding the overlapping coupling zone, Table 5.10 summarises the parameters used in our simulations. These parameters are specifically chosen to ensure the thermo-elastic effect within the coupling zone.

Table 5.10: Coupling properties.

Parameter - symbol	units	Value
Thermal penalty - ϵ^T	[W/m^3 K]	2×10^{-1}
Mechanical penalty - ϵ	[Pa/m^2]	1×10^{-2}
Tolerance - tol	[-]	1×10^{-8}
Coarse-grained width - $CG\ w$	[m]	$0.5R$

Fig. 5.23 illustrates the simulation of the coupled system.
Following the irradiation of surface particles with an energy input of $E_{in} = 384$ μJ over a duration of $t = 0.001$ s, as depicted in Fig. 5.23, heat is transferred to adjacent particles. This heat transfer facilitates mobility and interpenetration among the particles, which is essential for the sintering process. The temperature changes over time during this simulation are illustrated in Fig. 5.24, for particles located at the top surface within the spot radius.
The temperature of the particles located at the surface reaches $T = 210$ °C, which is high enough to sinter PA12. The laser is switched off at $t = 0.001$ s, the moment at which the cooling period starts, decreasing the temperature of the system by thermal dissipation
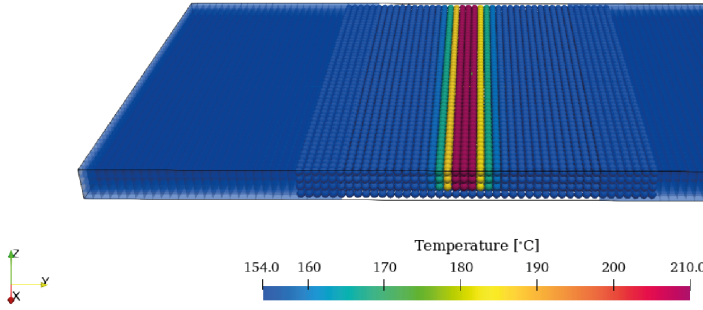
Figure 5.23: Coupled simulation of the selective laser sintering process at $t = 0.001$ s. The region where the laser heats the particles corresponds to the red area.
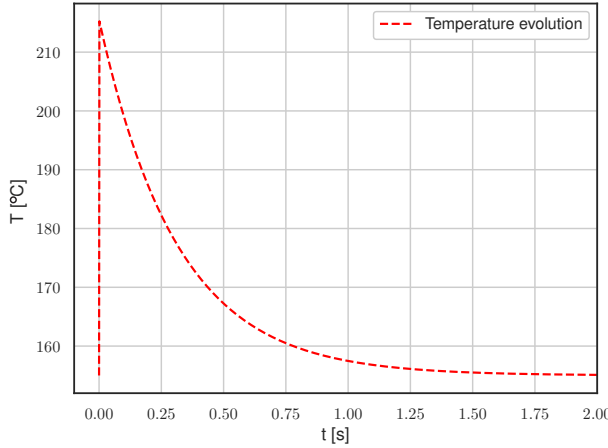
Figure 5.24: Temperature evolution of the region within the laser heats the particles.

until it reaches the initial temperature, $T = 153\,°$C. The axial reduction of the system is visualised in Fig. 5.25.

As shown in Fig. 5.25, particles situated in the region receiving higher energy (highlighted in red) absorb more energy, thus accelerating the sintering process compared to particles with lower temperatures, considering the material's melting point at $T_m = 185\,°$C. This energy absorption disrupts the initial arrangement of discrete elements, leading to a reduction in volume due to densification. To assess the mobility and, consequently, the sintering impact in the $y-$ direction, we calculate the thermal stress as follows:

$$\sigma_{thermal}(y) = \alpha E \Delta T(y)(L_y - y)/L_y, \qquad (5.105)$$
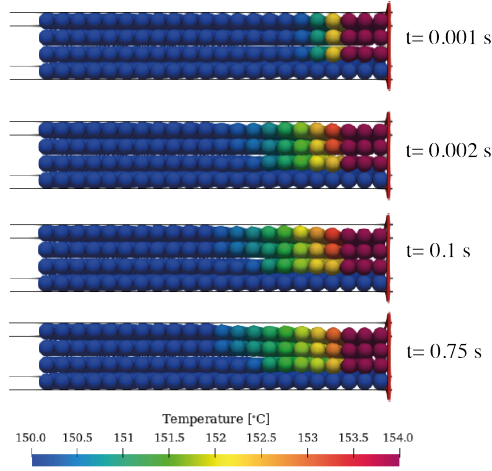
Figure 5.25: Axial reduction of the coupled system, visualized only on the half of the discrete domain. Note, the colour bar has been modified to observe the diffusion.

where α is the coefficient of thermal expansion of the material. E is the Young's modulus, ΔT is the change in temperature, L_y is the original length, and y is the displacement of both discrete and finite elements. The thermal stress on average, along the $y-$ direction, is visualised in Fig. 5.26.
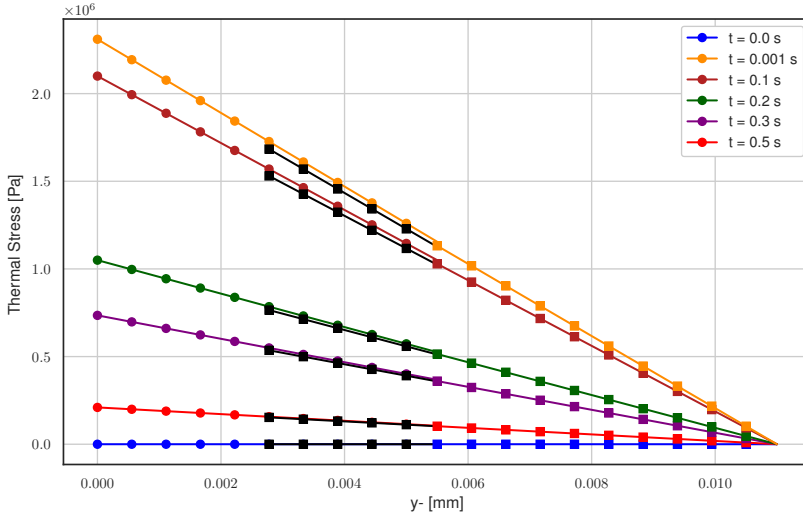
Figure 5.26: Thermal Stress of the coupled simulation during laser sintering. Dots represent the MercuryDPM results, while the squares are the oomph-lib results. The grey area represents the overlapping zone.

The results reveal how temperature fluctuations impact stress within the coupled domain. At $t = 0.001$ s, we observe elevated thermal stress, primarily attributed to the high temperatures resulting from the laser still being active. This stress gradually decreases along the $y-$ axis as the system's temperature reduces during the cooling phase when the laser is switched off. However, residual stress persists as a consequence of the sintering process among the discrete elements.

5.5. CONCLUSIONS AND OUTLOOK

This investigation presented a thermo-viscoelastic approach for analysing multi-physics processes. It begins by establishing the thermo-elastic formulation, which involves reviewing the momentum balance and thermal energy equations, and the implemented Galerkin method on the open-source software oomph-lib. The coupling approach is then formulated to handle the thermo-mechanical overlapping zone, integrated with MercuryDPM and enriched with coarse-graining.

Computational tests were conducted to verify the capabilities of MercuryDPM, oomph-lib, as well as the coupling approach in handling heat and thermo-viscoelastic problems. The results demonstrate good agreement with analytical solutions, indicating the efficacy of the software and the implemented coupling approach. It allowed us to analyse multi-physics scenario of the selective laser sintering process, modelled within a multi-scale perspective.

The laser sintering simulation considered the laser-particle interactions, the contact rheological model for sintering, and the elastic constitutive behaviour of the surrounding continuum. It is important to note that certain assumptions were made, such as the ideal distribution of particles, neglecting mass exchange, the effect of thermal dissipation in the solid media, and the crystallization process during cooling. However, this initial study paves the way for future simulations and improvements. For example, future studies can focus on refining and enhancing the current approach by addressing laser strategies, random particle packing and material properties.

5.6. ACKNOWLEDGMENTS

5.7. APPENDICES

5.7.1. APPENDIX: UNSTEADY HEAT TRANSFER

The unsteady heat conduction problem consists of determining the temperature fields $T(x, y, z, t)$ at any point within a domain such as

$$\alpha \left(\frac{\partial^2 T}{\partial x^2} + \frac{\partial^2 T}{\partial y^2} + \frac{\partial^2 T}{\partial z^2} \right) = \frac{\partial T}{\partial t}, \tag{5.106}$$

where $\alpha = k_{cond}/(\rho c_p)$ is the thermal diffusivity coefficient of the system, being k_{cond} the material conductivity, ρ the material density, and c_p the heat capacity. Neglecting the inner heat generation rate, an analytical solution is proposed by Weigand [29] to measure the temperature field along $y-$ axis of a 2D domain

$$T(y, t) = T_1 + \frac{y \Delta T}{L} + \Delta T \sum_{n=1}^{\infty} C_n \sin\left(\frac{n\pi y}{L}\right) e^{-(n\pi)^2 \frac{\alpha t}{L^2}}, \tag{5.107}$$

where the coefficients C_n are defined as

$$C_n = \frac{2}{L} \int_0^L (L\theta_0 - y) \sin(n\pi y) dy, \tag{5.108}$$

and θ_0 is a dimensionless quantity defined as $\theta_0 = \frac{T_0(y) - T_1}{T_2 - T_1}$, being T_1 and T_2 the constant temperatures at the bottom and top surfaces, respectively. n indicates the number of sinusoidal modes considered in the series expansion. L represents the domain length as illustrated by Fig. 5.27.
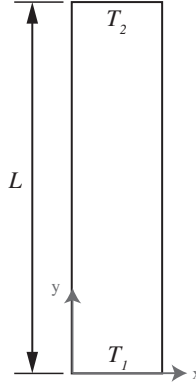
Figure 5.27: T_1 and T_2 are the temperatures at the bottom and top surfaces, respectively. We make the assumption that there is no internal heat generation $H = 0$, and no heat flux or heat transfer occurring across the boundaries of the volume V.

5.7.2. THERMAL DEFLECTION OF A CANTILEVER BEAM

In order to couple the heat equation and solid mechanics, we consider the uniform thermal deflection of an elastic body that is differentially heated, and restricted at one side (cantilever problem). The top surface is heated at temperature T_2, while the bottom surface is maintained at the reference temperature T_1. The problem is illustrated in Fig. 5.28.

In this context, we assume that the elastic body's material properties are temperature-dependent, with a coefficient of thermal expansion by α. As a result, the body will expand or contract according to α when the temperature changes, resulting in deformation and stress that can be modelled by solid mechanics equations. Note that when $T_2 > T_1$, the deflection is upward, and the angle of rotation is counterclockwise.

Figure 5.28: Illustration of the problem with temperature differential, δ deflection, and θ rotation.

The temperature variation over the beam's height is assumed to be linear. The beam's average temperature, occurring at the mid-height of the beam ($h/2$), is given by

$$\Delta T = \frac{T_1 + T_2}{2}. \tag{5.109}$$

If the beam is free to expand longitudinally, its length will increase by an amount of δ_T,

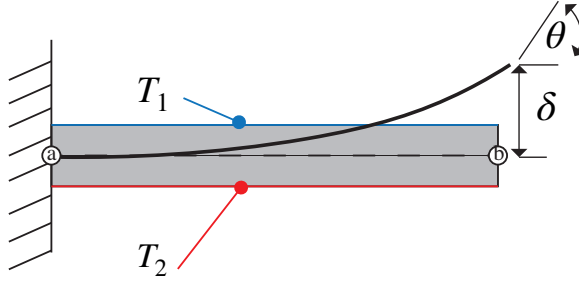$$\delta_T = \alpha_l \left(\frac{T_1 + T_2}{2} \right) L, \tag{5.110}$$

where α is the coefficient of thermal expansion of the material, and L is the length of the beam. To determine the deflections due to temperature differentials, consider the element of length dx cut out from the structure. The changes in the length of the element at the bottom and top are $\alpha(T_2 - T_0)dx$ and $\alpha(T_1 - T_0)dx$, respectively. If T_2 is greater than T_1, the sides of the element will rotate towards each other through an angle $d\theta$. This angle is related to the changes in dimensions by the following equation, obtained from geometry

$$hd\theta = \alpha(T_2 - T_0)dx - \alpha(T_1 - T_0)dx, \tag{5.111}$$

where h is the height of the beam. Therefore, we have

$$\frac{d\theta}{dx} = \frac{\alpha(T_2 - T_1)}{h}. \tag{5.112}$$

Since the curvature κ can be described as the derivative of the angle of rotation θ with respect to the position x (for small angles of rotations), which represents the deflection of the structure v, we can write

$$\kappa = \frac{1}{\rho} = \frac{d\theta}{dx} = \frac{d^2 v}{dx^2}. \tag{5.113}$$

Furthermore, if the material of the structure behaves elastically and follows Hooke's law, the curvature is related to the bending moment M and the flexural rigidity EI of the structure as follows,

$$\kappa = \frac{1}{\rho} = \frac{M}{EI}. \tag{5.114}$$

Combining these equations, we obtain the differential equation

$$\frac{d^2 v}{dx^2} = \frac{M}{EI} = \frac{\alpha(T_2 - T_1)}{h}. \tag{5.115}$$

If the beam is able to change in length and deflect freely, there will be no stresses associated with the temperature changes described in this section. However, if the beam is restrained against longitudinal expansion or lateral deflection, or if the temperature changes do not vary linearly from top to bottom of the beam, internal temperature stresses will develop.

To find the deflection, the following equations can be used

$$\frac{dV}{dx} = \frac{\alpha(T_2 - T_1)}{h} x + C_1. \tag{5.116}$$

If the boundary condition is $v'(0) = 0$, then $C_1 = 0$. Subsequently,

$$v = \frac{\alpha(T_2 - T_1)}{h} \left(\frac{x^2}{2}\right) + C_2. \tag{5.117}$$

If the boundary condition is $v(0) = 0$, then $C_2 = 0$. Thus, the deflection δ and angle of rotation θ at end b of this structure (due to the temperature differential) are as follows

$$\delta_B = v(L) = \frac{\alpha(T2 - T1)L^2}{2h}. \tag{5.118}$$

$$\theta_B = v'(L) = \frac{\alpha(T2 - T1)L}{h}. \tag{5.119}$$

Now, the reaction R and moment M of the structure can be found using the superposition method, which in cantilever beams gives

$$(\delta_b)_2 = \frac{R_b L^3}{3EI} \quad (\theta_b)_2 = \frac{R_b L^2}{2EI}. \tag{5.120}$$

$$(\delta_b)_2 = -\frac{M_b L^2}{2EI} \quad (\theta_b)_2 = -\frac{M_b L}{EI}. \tag{5.121}$$

The equations of compatibility can be written as follows

$$\delta_b = \delta_b + (\delta_b)_2 + (\delta_b)_3 = 0. \tag{5.122}$$

$$\theta_b = \theta_b + (\theta_b)_2 + (\theta_b)_3 = 0. \tag{5.123}$$

Substituting the appropriate expressions, we get

$$\frac{\alpha(T2 - T1)L^2}{2h} + \frac{R_b L^3}{3EI} - \frac{M_b L^2}{2EI} = 0, \tag{5.124}$$

$$\frac{\alpha(T2 - T1)L}{h} + \frac{R_b L^2}{2EI} - \frac{M_b L}{EI} = 0. \tag{5.125}$$

Therefore,

$$R_b = 0, \quad M_b = \frac{\alpha EI(T2 - T1)}{h}. \tag{5.126}$$

The fact that R_b is zero could have been anticipated initially from the symmetry of the fixed-end beam.

5.7.3. VIBRATION OF AN ELASTIC CANTILEVER BEAM

For the elastic bending of a cantilever beam with a uniform cross-section, as shown in Fig. 5.29, a transverse vibration force $F(x, t)$ was applied at the end.
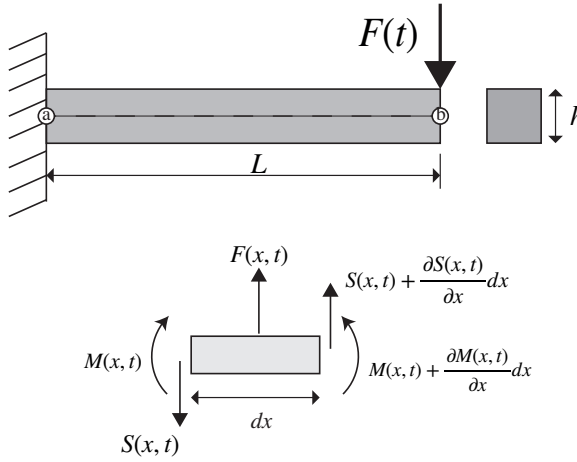
Figure 5.29: (Top) Cantilever beam of length L_y, height (L_z), width L_x, and square cross section. F represents the axial force applied at the free end at $t = 0$ s. Points a and b represents measuring points. (Bottom) infinitesimal points to describe the bending moment M, and shear force S of the beam.

Let the length be denoted by L, and the cross-sectional area be denoted by A. Assuming that the cross-sectional height h is relatively small compared to the beam's length, the inertia force in the beam element can be expressed as

$$F = (\rho A dx)\frac{\partial^2 u}{\partial t^2}(x, t), \tag{5.127}$$

where u represents the transverse displacement, ρ is the mass density of the beam. Therefore, the shear force equation for the beam element can be written as

$$(S(x, t) + dS(x, t)) - S(x, t) + F(x, t)dx = (\rho A dx)\frac{\partial^2 u}{\partial t^2}(x, t), \tag{5.128}$$

where $dS = \frac{\partial M}{\partial x}dx$. The moment equation for a beam can be expressed as

$$(M(x, t) + dM(x, t)) - M(x, t) + (S(x, t) + dS(x, t))dx + F(x, t)dx\frac{dx}{2} = 0, \tag{5.129}$$

where $dM = \frac{\partial M}{\partial x}dx$. The shear force and moment equations can be simplified as follows

$$\frac{\partial S}{\partial x}(x, t) + F(x, t) = (\rho A dx)\frac{\partial^2 u}{\partial t^2}(x, t), \tag{5.130}$$

$$-\frac{\partial M}{\partial x}(x, t) = S(x, t). \tag{5.131}$$

The force equation can be written in terms of displacement and transverse force

$$-\frac{\partial^2 M}{\partial x^2}(x, t) + F(x, t) = (\rho A dx)\frac{\partial^2 u}{\partial t^2}(x, t), \tag{5.132}$$

The relation between the bending moment and transverse displacement is expressed using the strength of materials

$$M(x, t) = EI(x)\frac{\partial^2 u}{\partial x^2}(x, t), \tag{5.133}$$

where E is the elastic modulus, and I is the moment of inertia of the beam. When the beam has a uniform cross-section, the equation of the vibrational beam can be transformed as

$$F(x, t) = EI\frac{\partial^4 u}{\partial x^4}(x, t) + (\rho A dx)\frac{\partial^2 u}{\partial t^2}(x, t). \tag{5.134}$$

For free bending vibration, the applied force is zero, therefore, the equation is reduced to

$$EI\frac{\partial^4 u}{\partial x^4}(x, t) + (\rho A dx)\frac{\partial^2 u}{\partial t^2}(x, t) = 0. \tag{5.135}$$

The solution of the above equation can be obtained through a separation of the dependent variable method expressed as

$$u(x, t) = U(x)V(t). \tag{5.136}$$

Thus, the free vibration of the beam can be deduced in the form of a separable variable method expressed as

$$\frac{EI}{(\rho A dx)}\frac{\partial^4 U(x)}{\partial x^4}V(t) + \frac{\partial^2 V(t)}{\partial t^2}U(x) = 0 \tag{5.137}$$

$$\frac{EI}{(\rho A dx)}V(t)\frac{\partial^4 U(x)}{\partial x^4} + U(x)\frac{\partial^2 V(t)}{\partial t^2} = 0 \tag{5.138}$$

$$-\frac{EI}{(\rho A dx)}\frac{\frac{\partial^4 U(x)}{\partial x^4}}{U(x)} = \frac{\frac{\partial^2 V(t)}{\partial t^2}}{V(t)}. \tag{5.139}$$

The last equation can be further simplified by introducing a separation constant ω^2, leading to

$$\frac{\frac{\partial^4 U(x)}{\partial x^4}}{U(x)} = +\omega^2 \quad \text{and} \quad \frac{\frac{\partial^2 V(t)}{\partial t^2}}{V(t)} = -\omega^2 \left(\frac{EI}{\rho A \mathrm{d}x}\right). \tag{5.140}$$

These equations can be solved separately, leading to the general solution of the form

$$u(x,t) = \sum_{n=1}^{\infty} \left[A_n \cos(n\pi x/L) + B_n \sin(n\pi x/L)\right] \sin(\omega_n t), \tag{5.141}$$

where L is the length of the beam, $\omega_n = n^2 \pi^2 \sqrt{EI/(\rho A \mathrm{d}x L^4)}$, and A_n and B_n are constants determined by the initial conditions.

Separating the time and spatial variables, respectively, we have

$$\frac{\partial^2 V(t)}{\partial t^2} + \omega^2 V(t) = 0, \tag{5.142}$$

$$(\frac{\partial^4 U(x)}{\partial x^4}) - \omega^2 \frac{(\rho A \mathrm{d}x) U(x)}{EI} = 0, \tag{5.143}$$

$$(\frac{\partial^4 U(x)}{\partial x^4}) - \beta^4 U(x) = 0, \tag{5.144}$$

The solution of the above equation can be written as

$$V(t) = B_1 \sin(\omega t) + B_2 \cos(\omega t). \tag{5.145}$$

The displacement solution is satisfied if

$$\beta^4 = \frac{\rho A}{EI} \omega^2. \tag{5.146}$$

The displacement equation for the vibration mode is assumed as

$$U(x) = A_0 \sin(\beta x) + A_1 \cos(\beta x) + A_2 \sinh(\beta x) + A_3 \cosh(\beta x). \tag{5.147}$$

where A_0, A_1, A_2, and A_3 are constants that can be obtained by applying the boundary conditions. The boundary conditions of the fixed-free beam are

$$U(0) = 0 \text{ (zero displacement) } U'(0) = 0 \text{ (zero slope)} \text{ at } x = 0, \tag{5.148}$$

and,

$$U''(L) = 0 \text{ (zero bending moment) } U'''(L) = 0 \text{ (zero shear force). at } x = L \tag{5.149}$$

Applying the first boundary condition, we get

$$A_1 = -A_3, \tag{5.150}$$

and applying the second boundary condition, we get

$$A_0 = -A_2, \tag{5.151}$$

Thus, the harmonic solution can be expressed as

$$U(x) = A_0\sin(\beta x) - \sinh(\beta x) + A_1\cos(\beta x) - \cosh(\beta x), \tag{5.152}$$

$$\frac{d^2U(x)}{dx^2} = -\beta^2[A_0\sin(\beta x) + \sinh(\beta x) + A_1\cos(\beta x) + \cosh(\beta x)], \tag{5.153}$$

$$\frac{d^3U(x)}{dx^3} = -\beta^3[A_0\cos(\beta x) + \cosh(\beta x) - A_1\sin(\beta x) - \sinh(\beta x)]. \tag{5.154}$$

Substituting $x = L$ and applying the second boundary condition, we get

$$\frac{d^2U(L)}{dx^2} = -\beta^2[A_0\sin(\beta L) + \sinh(\beta L) + A_1\cos(\beta L) + \cosh(\beta L)] = 0, \tag{5.155}$$

$$A_1 = -A_0\left[\frac{\sin(\beta L) + \sinh(\beta L)}{\cos(\beta L) + \cosh(\beta L)}\right], \tag{5.156}$$

$$\left[A_0\sin(\beta L) + \sinh(\beta L) + A_1\cos(\beta L) + \cosh(\beta L)\right] = 0. \tag{5.157}$$

Forming the equations into matrix format, we have

$$\begin{bmatrix} \sin(\beta L) + \sinh(\beta L) & \cos(\beta L) + \cosh(\beta L) \\ \cos(\beta L) + \cosh(\beta L) & -\sin(\beta L) + \sinh(\beta L) \end{bmatrix} \begin{bmatrix} A_0 \\ A_1 \end{bmatrix} = \begin{bmatrix} 0 \\ 0. \end{bmatrix} \tag{5.158}$$

By solving the system, we obtain the characteristic equation

$$\cos(\beta L)\cosh(\beta L) = -1. \tag{5.159}$$

Therefore, the roots of the above equation are

$$\begin{aligned} \beta L &= 1.87510 \quad \textbf{for } n = 1 \\ \beta L &= 4.69409 \quad \textbf{for } n = 2. \end{aligned} \tag{5.160}$$

The circular frequency of the beam can be expressed as

$$\omega^2 = \beta^4\frac{EI}{\rho A}, \tag{5.161}$$

$$\omega = (\beta L)^2\sqrt{\frac{EI}{\rho AL^4}}. \tag{5.162}$$

The natural frequency of the cantilever beam, which represents the mode of vibration, can be calculated as

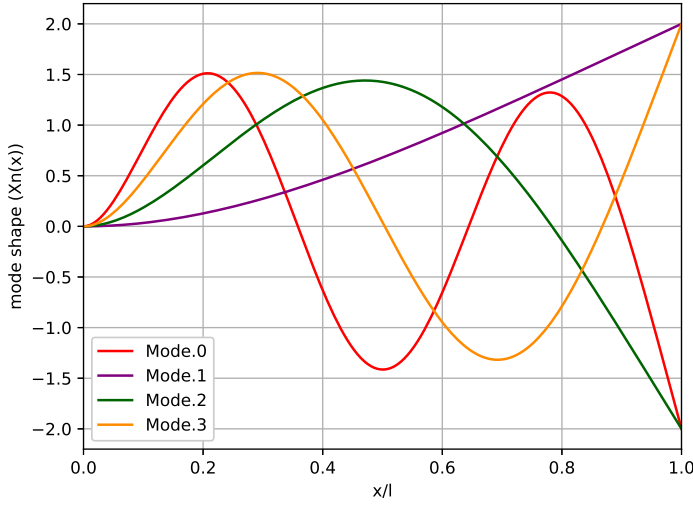$$f = \frac{\omega}{2\pi} = \frac{(\beta L)^2}{2\pi}\sqrt{\frac{EI}{(\rho A)L^4}}. \tag{5.163}$$

Figure 5.30: Modes of vibration of a cantilever beam.

Fig. 5.30 shows the different modes of vibration of the problem.

The modes of vibration of a beam depend on its shape, length, and material properties, and each mode corresponds to a specific natural frequency of the beam. These natural frequencies determine how the beam will vibrate when excited by a force or other disturbance.

5.7.4. VIBRATION OF AN ELASTIC AND DISSIPATIVE CANTILEVER BEAM

The model of a cantilever beam considering dissipation, disrupted by a transversal force at the free end, can be expressed by the following equation:

$$EI\frac{d^4u}{dx^4}(x,t) + \mu\frac{du}{dt}(x,t) + k\frac{d^2u}{dt^2} = F(x,t), \tag{5.164}$$

where $u(x,t)$ is the transverse displacement of the beam at position x and time t, EI is the flexural rigidity of the beam, μ is the damping coefficient, k is the spring constant due to the material and boundary conditions, and $F(x,t)$ is the load applied to the beam. The solution considering dissipation involves the use of the Euler-Bernoulli beam theory, which takes into account the damping effect of the material. The displacement equation for a cantilever beam with damping can be expressed as

$$u(x,t) = \sum_{n=1}^{\infty} A_n \sin\left(\frac{n\pi x}{L}\right) e^{-\mu\omega_n t}\sin(\omega_{dn}t + \phi_n), \tag{5.165}$$

where μ is the damping ratio, ω_n is the natural frequency of the beam, and $\omega_{dn} = \sqrt{1-\mu^2}\omega_n$ is the damped natural frequency. The constants A_n and ϕ_n are

determined by the initial conditions. The displacement solution with damping shows that the amplitude of the vibration of the beam will decrease over time due to the damping effect of the material. This means that the displacement of the beam will reach a steady-state value, which is smaller than the maximum displacement that would occur in the absence of damping.

5.7.5. VIBRATION OF AN ELASTIC AND/OR DISSIPATIVE CANTILEVER BEAM WITH TEMPERATURE

To include the effect of temperature for thermo-mechanical analysis of the cantilever beam, the thermal energy balance is considered.

$$\rho C_p \frac{\partial T}{\partial t} - \nabla \cdot (k \nabla T) = 0, \tag{5.166}$$

where ρ is the material density, C_p is the specific heat capacity at constant pressure, T is the temperature, k is the thermal conductivity. We can couple this equation with the mechanical equation of motion for the cantilever beam by adding a term that represents the effect of temperature on the material stiffness, such as

$$EI(T) \frac{d^4 u}{dx^4}(x, t) + \mu(T) \frac{du}{dt}(x, t) + k(T) \frac{d^2 u}{dt^2}(x, t) = F(x, t), \tag{5.167}$$

where $EI(T)$, $\mu(T)$, and $k(T)$ are the temperature-dependent bending stiffness, damping coefficient, and mass density. These quantities can be obtained from experimental data or from theoretical models that take into account the effect of temperature on the material properties. As the analytical solution is not trivial, we use oomph-lib to handle both the mechanical and thermal equations simultaneously, validating the mechanical and thermal fields in the previous tests.

REFERENCES

[1] S. Luding, *Cohesive, frictional powders: Contact models for tension,* Granular Matter **10**, 235 (2008).

[2] S. Luding, K. Manetsberger, and J. Müllers, *A discrete model for long time sintering,* Journal of the Mechanics and Physics of Solids **53**, 455 (2005).

[3] C. Martin, L. Schneider, L. Olmos, and D. Bouvard, *Discrete element modeling of metallic powder sintering,* Scripta materialia **55**, 425 (2006).

[4] P. Hejmady, L. C. Van Breemen, P. D. Anderson, and R. Cardinaels, *Laser sintering of polymer particle pairs studied by in situ visualization,* Soft Matter **15**, 1373 (2019).

[5] O. Pokluda, C. T. Bellehumeur, and J. Vlachopoulos, *Modification of Frenkel's model for sintering,* AIChE Journal **43**, 3253 (1997).

[6] G. Lutzweiler, J. Farago, E. Oliveira, L. Jacomine, O. Erverdi, N. E. Vrana, A. Testouri, P. Schaaf, and W. Drenckhan, *Validation of Milner's visco-elastic theory of sintering for the generation of porous polymers with finely tuned morphology,* Soft Matter **16**, 1810 (2020).

[7] Y. Y. Lin, C. Y. Hui, and A. Jagota, *The role of viscoelastic adhesive contact in the sintering of polymeric particles,* Journal of Colloid and Interface Science **237**, 267 (2001).

[8] J. Alvarez, H. Snijder, T. Vaneker, H. Cheng, A. Thornton, S. Luding, and T. Weinhart, *Visco-elastic sintering kinetics in virgin and aged polymer powders,* Powder technology **397**, 117000 (2022).

[9] P. Rando and M. Ramaioli, *Numerical simulations of sintering coupled with heat transfer and application to 3D printing,* Additive Manufacturing **50**, 102567 (2022).

[10] Q. Meng, X. Song, S. Han, F. Abbassi, Z. Zhou, B. Wu, X. Wang, and S. Araby, *Mechanical and functional properties of polyamide/graphene nanocomposite prepared by chemicals free-approach and selective laser sintering,* Composites Communications **36**, 101396 (2022).

[11] D. M. Sassaman, M. S. Ide, J. J. Beaman, and D. Kovar, *A model for bonding mechanisms in indirect laser powder bed fusion of nylon/alumina blends,* Additive Manufacturing **59**, 103163 (2022).

[12] C. Bierwisch, S. Mohseni-Mofidi, B. Dietemann, M. Gruenewald, J. Rudloff, and M. Lang, *Universal process diagrams for laser sintering of polymers,* Materials & Design **199**, 109432 (2021).

[13] S. Waqar, K. Guo, and J. Sun, *FEM analysis of thermal and residual stress profile in selective laser melting of 316L stainless steel,* Journal of Manufacturing Processes **66**, 81 (2021).

[14] C. Luo, J. Qiu, Y. Yan, J. Yang, C. Uher, and X. Tang, *Finite element analysis of temperature and stress fields during the selective laser melting process of thermoelectric SnTe,* Journal of Materials Processing Technology **261**, 74 (2018).

[15] A. Foroozmehr, M. Badrossamay, E. Foroozmehr, and S. Golabi, *Finite element simulation of selective laser melting process considering optical penetration depth of laser in powder bed,* Materials & Design **89**, 255 (2016).

[16] F. Liu, Q. Zhang, W. Zhou, J. Zhao, and J. Chen, *Micro scale 3D FEM simulation on thermal evolution within the porous structure in selective laser sintering,* Journal of Materials Processing Technology **212**, 2058 (2012).

[17] A. K. S. Chauhan, M. Shukla, and A. Kumar, *3D thermal simulation of powder bed fusion additive manufacturing of stainless steel,* International Journal on Interactive Design and Manufacturing (IJIDeM) , 1 (2023).

[18] M. Ganci, W. Zhu, G. Buffa, L. Fratini, S. Bo, and C. Yan, *A macroscale FEM-based approach for selective laser sintering of thermoplastics,* The International Journal of Advanced Manufacturing Technology **91**, 3169 (2017).

5

[19] T. Weinhart, L. Orefice, M. Post, M. P. van Schrojenstein Lantman, I. F. Denissen, D. R. Tunuguntla, J. M. Tsang, H. Cheng, M. Y. Shaheen, H. Shi, P. Rapino, E. Grannonio, N. Losacco, J. Barbosa, L. Jing, J. E. Alvarez Naranjo, S. Roy, W. K. den Otter, and A. R. Thornton, *Fast, flexible particle simulations — An introduction to MercuryDPM,* Computer Physics Communications **249**, 107129 (2020).

[20] M. Heil and A. L. Hazel, *oomph-lib- An object-oriented multi-physics finite-element library,* in *Fluid-structure interaction: Modelling, simulation, optimisation* (Springer, 2006) pp. 19–49.

[21] H. Cheng, A. R. Thornton, S. Luding, A. L. Hazel, and T. Weinhart, *Concurrent multi-scale modeling of granular materials: Role of coarse-graining in FEM-DEM coupling,* Computer Methods in Applied Mechanics and Engineering **403**, 115651 (2023).

[22] T. Weinhart, A. R. Thornton, S. Luding, and O. Bokhove, *From discrete particles to continuum fields near a boundary,* Granular Matter **14**, 289 (2012).

[23] R. B. Hetnarski, M. R. Eslami, and G. Gladwell, *Thermal stresses: advanced theory and applications*, Vol. 41 (Springer, 2009).

[24] B. A. Boley and J. H. Weiner, *Theory of thermal stresses* (Courier Corporation, 2012).

[25] R. B. Hetnarski and J. Ignaczak, *Generalized thermoelasticity,* Journal of Thermal Stresses **22**, 451 (1999).

[26] Q. X. Le, J. L. Torero, and V. T. Dao, *Understanding the effects of stress on the coefficient of thermal expansion,* International Journal of Engineering Science **141**, 83 (2019).

[27] T. Weinhart, C. Labra, S. Luding, and J. Y. Ooi, *Influence of coarse-graining parameters on the analysis of DEM simulations of silo flow,* Powder technology **293**, 138 (2016).

[28] S. Nosewicz, J. Rojek, M. Chmielewski, K. Pietrzak, and D. Lumelskyj, *Application of the Hertz formulation in the discrete element model of pressure-assisted sintering,* Granular Matter **19**, 1 (2017).

[29] B. Weigand, *Analytical methods for heat transfer and fluid flow problems*, Vol. 263 (Springer, 2004).

5

6

CONCLUSIONS AND OUTLOOK

This thesis provides an investigation of the sintering process of visco-elastic powders using a multi-scale approach and multi-physics methodology. The research has yielded valuable insights into the impact of process and material parameters, particularly in the context of applications like laser sintering and dilatometric analysis. The sintering model accurately computes the sintering rate of visco-elastic particles, such as polymers, and has been developed, calibrated, validated, and applied through various investigations. It enables future studies to refine and customize the process for diverse targets and applications, serving as a virtual prototype.

The thesis's interrelated investigations cover the entire spectrum of the sintering process sequentially, from micro-scale particle-particle interactions modelled using DEM to macro-scale continuum deformations modelled by FEM, as follows.

The initial study, described in Chapter 2, introduced a DEM model that uses a sintering regime map to forecast the sintering kinetics of visco-elastic particles. This model takes into account the material's contact rheology around melting during particle-particle interactions and demonstrated remarkable consistency with experimental observations on different polymers such as PA12, PS, and PEEK. Additionally, the model is capable of predicting the sintering kinetics for degraded materials, such as those that have undergone powder recycling or annealing processes.

In Chapter 3, the sintering model was improved by including the heat balance equation within the linear momentum conservation, and then provide a more comprehensive understanding of the multi-physics involved in the sintering process. This included accounting for different modes of heat transfer, such as conduction between particles, convection with and radiation to the environment. Additionally, a non-homogeneous laser energy input was considered, and a new ray tracing model was developed to compute particle temperature at each time step and particle-particle inter-penetrations. The findings of the study demonstrated that energy density and the time-dependent nature of visco-elastic coalescence have a significant impact on the

sintering process. Furthermore, experimental data on two materials, PA12 and PS, were used to calibrate the model.

In Chapter 4, the impact of process parameters on the sintering process was explored by investigating the densification of pellets made of PA12 powder. The investigation utilized the current temperature and pressure-dependent DEM model, which accurately predicted the shrinkage of the experiments. The study analysed different factors such as holding time, process time, sintering temperature, and pressure. The findings revealed that process time and pressure assisted sintering significantly, particularly when the pellet is close to the material's melting point.

In Chapter 5, a novel thermo-mechanical model was developed to simulate the intricate interplay between heat dissipation and mechanical deformation using finite elements and discrete elements. The significance of volume coupling was showcased as it enabled the transition between both media. Through this approach, the sintering process was simulated, seamlessly integrating both microscopic and macroscopic perspectives while upholding the principles of thermal energy conservation and momentum conservation.

In conclusion, the multi-scale sintering model of visco-elastic powders presented in this thesis provides a tool for optimizing sintering processes for various industrial applications via virtual prototyping.

The following are some key messages and conclusions from this thesis:

1. This thesis introduces a novel DEM framework that can accurately predict the sintering behaviour of visco-elastic powders at both short and long time-scales.

2. The sintering model considers the material contact rheology during particle-particle interactions and enables the calibration of model parameters for recycled particles.

3. Bayesian inference was used to calibrate sintering material parameters, which were then validated using experimental data. This grain learning approach provides a robust and data-driven method for parameter calibration.

4. The study found that sintering takes two to three times longer for aged polymer powders, highlighting the importance of carefully selecting and storing materials for sintering processes.

5. A new DEM model was developed that includes energy absorption and laser sintering based on ray tracing. This model provides insights into the impact of inhomogeneous, localized laser energy parameters on the sintering process and can help optimize sintering outcomes.

6. A new DEM model to study densification of visco-elastic pellets, which was validated using dilatometric experimental data.

7. Longer process times and external pressure are the process parameters that assist further densification of PA12 pellets.

8. A Multi-scale and multi-physics DEM-FEM model to simulate thermo-mechanical processes.

9. Coarse-graining enriched homogenization technique, which enhances the coupling framework's accuracy and efficiency.

OUTLOOK

1. Chapter 2: In future studies, the proposed approach could be utilized to analyse the strength evolution by sintering. It would help to avoid surface defects from the poor cohesion of sintered layers. This approach may also be extended to investigate the influence of different particle shapes and surface treatments on sintering behaviour.

2. Chapter 3: To effectively apply this model to realistic powder mixtures, further work can explore the influence of different mechanical properties, and material parameters such as poly-disperse size distribution, particle size, and volume fraction, on sintering kinetics. Additionally, the proposed approach can be extended to investigate laser sintering of metallic and ceramic powders, as well as as well as the effect of printing on multiple layers.

3. Chapter 4: It presents several avenues for future studies to improve the sintering model's predictive capability. One potential area of focus could be incorporating the crystallization process during the cooling stage into the DEM model, which would provide further insight into the densification. Additionally, the effect of dilatation due to the presence of air or bubbles, which can cause additional pressure effects, could be incorporated into the model by exploring a function that describes fluidity based on experimental data. The results of DEM simulations would be useful to develop predictive models for powder densification and sintering, which could aid in the optimization of process parameters and the design of new materials.

4. Chapter 5: Future work can focus on extending the continuum model presented in this chapter to include the effects of anisotropic material properties and micro-structure, which may have a significant impact on the sintering process. The model could be extended to investigate the sintering of other materials, such as metals and ceramics, which exhibit different deformation behaviours. Additionally, laser strategies can be analysed in future studies.

6

ACKNOWLEDGEMENTS

"If have seen further, it is by standing on the shoulders of giants."
- Isaac Newton

The journey as a PhD student has been extensive, enjoyable, stressful, and challenging. But most importantly, I have gained knowledge and inspiration by standing on the shoulders of amazing people and looking further. Thank you, **Prof. Stefan**, **Dr. Thomas** and **Dr. Hongyang** for the supervision during this journey. Our weekly meetings motivated me to strive daily to prove myself as an engineer, scientist, individual, and colleague at the University of Twente.

I'm grateful to **Prof. Anthony** for allowing me to explore my capabilities as a developer for MercuryDPM. The software, while occasionally testing my patience, also demonstrated the beauty of well-crafted software. I also express my appreciation to **Prof. Andrew** for his guidance during my intern-ship at the University of Manchester, where he helped me deepen my understanding of my passion for continuum thermo-elasticity. These experiences were immensely valuable.

Throughout this journey, I've formed strong bonds with colleagues and, of course, friends. **Sylvia**, thank you for your unwavering support. I would like to thank my paranymphs **Timo** and **Sahar**, who work hard every day. I cherish the moments spent with invaluable friends, whether over coffee, social events, discussions, laughs, or parties. **Tim**, **Laura**, **Daniel**, **Stefano**, **Mitchel**, and **Max**, your friendship has enriched my life. I'm also grateful to everyone in the multi-scale mechanics group and the thermal and fluid department.

I must acknowledge that my PhD journey was inspired by **Dr. Hongyang**, while my Master's journey was shaped by **Dr. Andres**. I feel fortunate to have had the company of two individuals who not only encouraged me to aim higher but also possessed incredible minds and personalities. They were truly my mentors.

My close friends have played an essential role in helping me unwind through board games, social activities, gym sessions, and dancing. **Nataly**, I discovered my love for gintonic thanks to you, while waiting for **Juan Camilo** and enjoying **Luisa**'s contagious smile. **Juan Sebastian**, we can now sit at the same table, observing **Bruno**'s dance at the pole, listening to **Luiza**'s funky tunes, and noting **Pedro**'s almost dancing like if he were at the Barranquilla's Carnival. Of course, thank you to my Greek friends **Orfeas** and **Ilias**, my Dutch friends **Gabriela**, **Demilya**, **Rick** and my Romanian friends **Anya** and **Elena**.

Thank you, **Maria Jose**, for your invaluable help with the document cover and your unwavering friendship. To **Mariana** and her sage advice. And, of course, a heartfelt

thank you to **Yelitza** for your unconditional support and friendship. To **Luis** and **Fabian**. You all for being such special friends.

Thank you to my family. My mother, **Luz Stella**, dedicated herself tirelessly to guide me. I want to express my gratitude to my aunt, **Gloria Patricia**, and **Jacinto** for their unwavering support during my student years. To my brother **Juan Bernardo**, **Luz Stella** and **Sebastian**, my nephew.

I would like to extend my thanks to **Rosa** for her courage and determination. And to **Leidy**, you are the one who embraces me and makes me feel like a true Dominican.

In 2016, I left Colombia and for the first time in seven years, I felt at home, in the Netherlands. This was due to finding a Dutch home and an italian family full of love. I would like to thank **Alessio** for sharing his days and **Francesca**, **Marcel**, **Riccardo**, **Mallory**, **Santiago**, and **Gianna** for making me feel warmly welcomed.

I want to express my gratitude to my Brazilian friends. They will always hold a special place in my heart. **Marcelo filho**, **Marcelo**, **Gianne**, and **Larissa**.

Finally, I want to say thank you to my biggest inspiration, the person who always welcomed me with a smile when I arrived home, the individual who carried encyclopaedias and books everywhere, and to whom this thesis is dedicated. Thank you, giant grandpa **Bernabe**.

<div align="right">Juan Alvarez</div>

6

University of Twente
2023

CURRICULUM VITAE

Juan Esteban Alvarez Naranjo

08-11-1991   Born in Zarzal - Valle del Cauca, Colombia.

EDUCATION

2008–2013   B. E. in Mechanical Engineering
Technological University of Pereira, Colombia

2016–2018   M. Sc. in Mechanical Engineering
The University of Campinas, Brazil

2019–2023   PhD candidate at the Multi-Scale Mechanics Group
The University of Twente, The Netherlands

Thesis: Multi-scale Sintering Model of Visco-elastic Powders
Promotor: prof.dr.rer.-nat. S. Luding
Co-promotor: dr. T. Weinhart

PhD internship at Department of Mathematics-2022
The University of Manchester, The United Kingdom
Supervisor: prof.dr A. Hazel

PROFESSIONAL EXPERIENCES

- Software engineer - AutoForm
The Netherlands/Switzerland - **2023 -**

- Lecturer: Programming in Engineering C++ - The University of Twente
Role: teacher.
The Netherlands - **2020 - 2022**

- Research assistant - AFOSR
Brazil - **03/2018 - 08/2018**

- Design engineer - BUSSCAR de Colombia S.A
Colombia - **06/2015 - 01/2016**

- Research assistant - COLCIENCIAS
  Colombia - **01/2014 - 12-2014**

- Mechanical Engineering assistant - UTP
  Colombia - **06/2013 - 12/2013**

- Design engineering internship - INDUMA S.A
  Colombia - **01/2013 -06/2013**

SUPERVISION EXPERIENCES

- Master supervision in Mechanical engineering - Henk Snijder. The role of powder ageing in the polymer sintering process, **2022**, The University of Twente - The Netherlands.

- Master supervision in Mechanical engineering - Bert Nijkamp. Modelling of laser beam absorption in powder-based sintering processes, **2022**, The University of Twente - The Netherlands.

PROJECT EXPERIENCES

- Project: Virtual Prototyping of Particulate Processes (ViPr) - Design and Optimisation via Multiscale Modelling and Rapid Prototyping. NWO-TTW grant No.16604. **2019 - 2023** - The Netherlands.

- Project: Multi-Scale Dynamic Failure Modeling of Heterogeneous Materials. Project supported by the Air Force Office of Scientific Research under award number FA9550-18-1-0113. **2018** - Brazil.

- Project: Determinación de la condición de operación de máquinas industriales por medio del análisis de vibraciones. Casos de estudio: Motores de combustión interna y máquinas hidráulicas. COLCIENCIAS. **2013 - 2014** - Colombia.

HONORS AND AWARDS

- Excellent presentation award **2022** - International Workshop on Computational Mechanics of Granular Materials for PhD students. Modelling the neck-growth kinetics of visco-elastic powders, China.

- Best poster presentation **2021** - Graduate School on Engineering Mechanics (EM). Thermo-mechanical modelling of polymer sintering, The Netherlands.

- Graduated with honours at the Technological University of Pereira **2013**, Colombia.

- Undergraduate college dissertation completion award, Technological University of Pereira **2013**, Colombia.

INVITED SPEAKER

Minisymposium Presentation at the 9th International Conference on Discrete Element Methods (DEM9) **2023**. Contact rheology model for visco-elastic powders during laser sintering. Advancements in Additive Manufacturing processes through the use of the Discrete Element Method (DEM). Erlangen, Germany.

LIST OF PUBLICATIONS

JOURNAL PUBLICATIONS

- **Alvarez, J. E.**, Snijder, H., Vaneker, T., Cheng, H., Thornton, A. R., Luding, S., & Weinhart, T. (**2022**). Visco-elastic sintering kinetics in virgin and aged polymer powders. *Powder technology*, 397, 117000.

- **Alvarez, J. E.**, Ramos, C. C., Galvis, A. F., & Sollero, P. (**2021**). A fully dynamic bridging approach for modeling the intergranular failure mechanisms in 2D polycrystalline materials. *Mechanics of Materials*, 159, 103920.

- Weinhart, T., Orefice, L., Post, M., van Schrojenstein Lantman, M. P., Denissen, I. F., Tunuguntla, D. R., Tsang, .M.F., Cheng, H.,Shaheen, M, Y., Shi, H., Rapino, P., Grannonio, E., Losacco, N., Barbosa, J., Jing, Lu., **Alvarez, J. E.**, Roy, S.,den Otter, W., & Thornton, A. R. (**2020**). Fast, flexible particle simulations—an introduction to MercuryDPM. *Computer physics communications*, 249, 107129.

- **Alvarez, J. E.**, Galvis, A. F., & Sollero, P. (**2018**). Multiscale dynamic transition of 2D metallic materials using the boundary element method. *Computational Materials Science*, 155, 383-392.

- **Alvarez, J. E.**, Nijkamp, B., Cheng, H., Luding, S., & Weinhart, T. (**Submitted, 2023**). Contact rheology model for visco-elastic powders during laser sintering.

- **Alvarez, J. E.**, Cheng, H., Luding, S., & Weinhart, T. (**submitted, 2023**). Densification of visco-elastic powders during free and pressure-assisted sintering.

- **Alvarez, J. E.**, Cheng, H., Luding, S., Hazel, A., & Weinhart, T. (**to be submitted, 2023**). A thermo-mechanically coupled multi-scale model of granular media.

CONFERENCES

- **Alvarez, J. E.**, Cheng, H., Luding, S., Hazel, A., & Weinhart, T. (2023). Multi-scale modelling of thermo-mechanically coupled processes in granular materials. In 10th International Conference on Computational Methods for Coupled Problems in Science and Engineering (COUPLED), Crete, Greece.

- **Alvarez, J. E.**, Cheng, H., Luding, S., & Weinhart, T.(2022). Modelling of selective laser sintering of visco-elastic powders. In 10th International Conference for Conveying and Handling of Particulate Solids (CHOPS), Salerno, Italy.

- **Alvarez, J. E.**, Cheng, H., Luding, S., & Weinhart, T.(2022). Modelling the neck growth kinetics of visco-elastic powders. In International Workshop on Computational Mechanics of Granular Materials, Dalian, China.

- **Alvarez, J. E.**, Cheng, H., Luding, S., & Weinhart, T.(2021). Neck growth kinetics during polymer sintering for powder-based processes. In Powders & Grains, Buenos Aires, Argentine.

- **Alvarez, J. E.**,Cheng, H., Luding, S., & Weinhart, T. (2019). Multi-scale simulations of particulate processes. In 8th International Conference on Discrete Element Methods (DEM8), Enschede, The Netherlands.

- **Alvarez J. E.**, Galvis, A. F., Sollero, P. (2018) Micro dynamic failure of 2D crystal aggregate structures using BEM and a hierarchical multiscale cohesive zone model. In International Conference on Boundary Element Techniques (BETEQ), Malaga, Spain.

- **Alvarez, J. E.**, Galvis, A. F., Sollero, P. (2017). Macro-micro scale dynamic analysis of 2D polycrystalline materials using the boundary element method. In 38th Ibero-Latin American Congress on Computational Methods in Engineering (CILAMCE), Florianopolis, Brazil.

- **Alvarez, J. E.**, Quintero, H. F., Lopez, J. F. L. (2014) Cavitation detection in a centrifugal pump using envelope analysis. In 2nd International Congress of Advanced Technologies, Design and Manufacturing (AMDM), Bogota, Colombia.